Utah State University

DigitalCommons@USU

12-2020

Effects of the Radiation Belt on the Plasmasphere Distribution

Stefan Thonnard
Utah State University

Follow this and additional works at: https://digitalcommons.usu.edu/etd

Part of the Plasma and Beam Physics Commons

Recommended Citation

EFFECTS OF THE RADIATION BELT ON THE PLASMASPHERE DISTRIBUTION

by

Stefan Thonnard

A dissertation submitted in partial fulfillment
of the requirements for the degree

of

DOCTOR OF PHILOSOPHY

in

Physics

Approved:

_____   _____
Robert Schunk, Ph.D.   Eric Held, Ph.D.
Major Professor   Committee Member

_____   _____
Bela Fejer, Ph.D.   Charles Swenson, Ph.D.
Committee Member   Committee Member

_____   _____
Mike Taylor, Ph.D.   D. Richard Cutler, Ph.D.
Committee Member   Interim Vice Provost
                                                        of Graduate Studies

UTAH STATE UNIVERSITY
Logan, Utah

2020

ABSTRACT

Effects of the Radiation Belt on the Plasmasphere Distribution

by

Stefan Thonnard, Doctor of Philosophy

Utah State University, 2020

Major Professor: Dr. Robert Schunk
Department: Physics

This study examines the distribution of plasmasphere ions in the presence of warmer radiation belt particles. Recent satellite observations of the radiation belts indicate the existence of a population of warm ions with energy 100 keV to 1 MeV trapped along magnetic field lines. Although likely having terrestrial origin, these lower energy trapped particles consisting of H^+, He^+ and O^+ ions do not have the same morphology as the colder ions created in the ionosphere and transported along field lines into the plasmasphere. To explore the interaction of these two coexisting populations, this study initially developed a simple one-dimension model of the F-region ionosphere and examined the effects of inserting an independent species of charge particles. The effort was extended by creating a representative density distribution of radiation particles using the Air Force AE9AP9 radiation belt model and incorporating them as an independent species into the two-dimensional solution for the transport of convecting plasma along a magnetic field line in the Ionosphere-Plasmasphere Model (IPM). The two models were used to explore different solar and geomagnetic conditions, and determined that the outer radiation belt has the greatest effect on the background plasmasphere in the equatorial

region at 18,500 km altitude. During solar maximum conditions the radiation belt particle density is negligible compared to the background plasmasphere. However, this investigation shows that during solar minimum the outer radiation belt could impart up to a 10% change in the plasmasphere distribution, predominately H^+. Furthermore, the warm O^+ ions from the radiation belt account for most of the effect on the colder plasmasphere H^+ distribution. Additionally, the study suggests that during moderate but relatively frequent solar storms when the outer plasmasphere is depleted, the rapid population of O^+ into the outer radiation belt may increase the time to refill the cold plasma in that region by 30%.

(162 pages)

PUBLIC ABSTRACT

Effects of the Radiation Belt on the Plasmasphere Distribution

Stefan Thonnard

This study examines the interaction of plasma, ions and electrons created by Solar illumination in the Earth's upper atmosphere, that travels along magnetic field lines filling the Plasmasphere, and the naturally occurring trapped particles known as the outer radiation belt. Although these two science disciplines have been largely worked independent of each other due the vast differences in the energy of the particles, recent satellite observations indicate a large population of particles with lower energy and greater mass also exist in the outer radiation belt. This study shows that during conditions of low solar output in an 11-year cycle, these newly identified particles may have an effect on the background plasma flowing up from the upper atmosphere along the magnetic field lines. Additionally, the study indicates that relatively frequent small solar storms that rapidly increase the radiation belt density may repel the upward flow of plasma, increasing the time for the background to return to the pre-storm conditions by 30%.

ACKNOWLEDGMENTS

CONTENTS

LIST OF TABLES

LIST OF FIGURES

CHAPTER I

INTRODUCTION

Sun and Solar Wind

In comparison to other stars, the Sun is of average mass and radius with a stable energy output dissipated into a spectrum of electromagnetic radiation and particles. The Sun's atmosphere is composed of three layers and it plays an important role in the Sun-Earth interaction. The photosphere, the atmosphere closest to the surface, is a thin layer where the temperatures decrease from 6000 K to 4500 K and visible radiation is produced. Beyond the photosphere, the layer where the temperature increases rapidly to 25,000 K within 4,000 km is known as the chromosphere. However, the vast majority of the Sun's atmosphere resides in an outermost layer known as the corona. In the corona the temperature of the ionized plasma is approximately 10^6 K and extends outward beyond 10 solar radii (Schunk & Nagy, Ionospheres, 2009). In addition to visible light, the Sun's atmosphere emits electromagnetic radiation in the X-ray, ultraviolet (UV), and extreme ultraviolet (EUV) spectrum. The energy distribution and variations in the electromagnetic radiation of the Sun are important drivers of planetary ionospheres.

The Sun has a 27-day axial rotation and possesses a strong magnetic field. The magnetic field is predominately dipole in shape with an offset between the dipole and rotational axis. The magnetic field of the Sun varies across a 22-year cycle coinciding with a reversal in polarity of the magnetic poles. Within the corona, plasma is trapped along the closed dipole field lines. Depending on the strength of the magnetic field, the high temperatures of the corona result in the radial flow of plasma outward known as the

solar wind. As the plasma accelerates outward it become supersonic, meaning that the

bulk velocity becomes greater than the characteristic wave speed in the medium, Figure

1. In addition, some field lines in the corona are not closed and result in streams of hot

plasma escaping radially. These streams of energetic particles provide the observed high-

speed component of the solar wind. Also, intense heating due to thermal conduction

fronts along a closed field loop can raise the plasma temperature to 20 to 30 million

degrees Kelvin. At times, one end of the loop breaks free ejecting highly energetic

plasma into space. Such events are known as coronal mass ejections (CME) and can
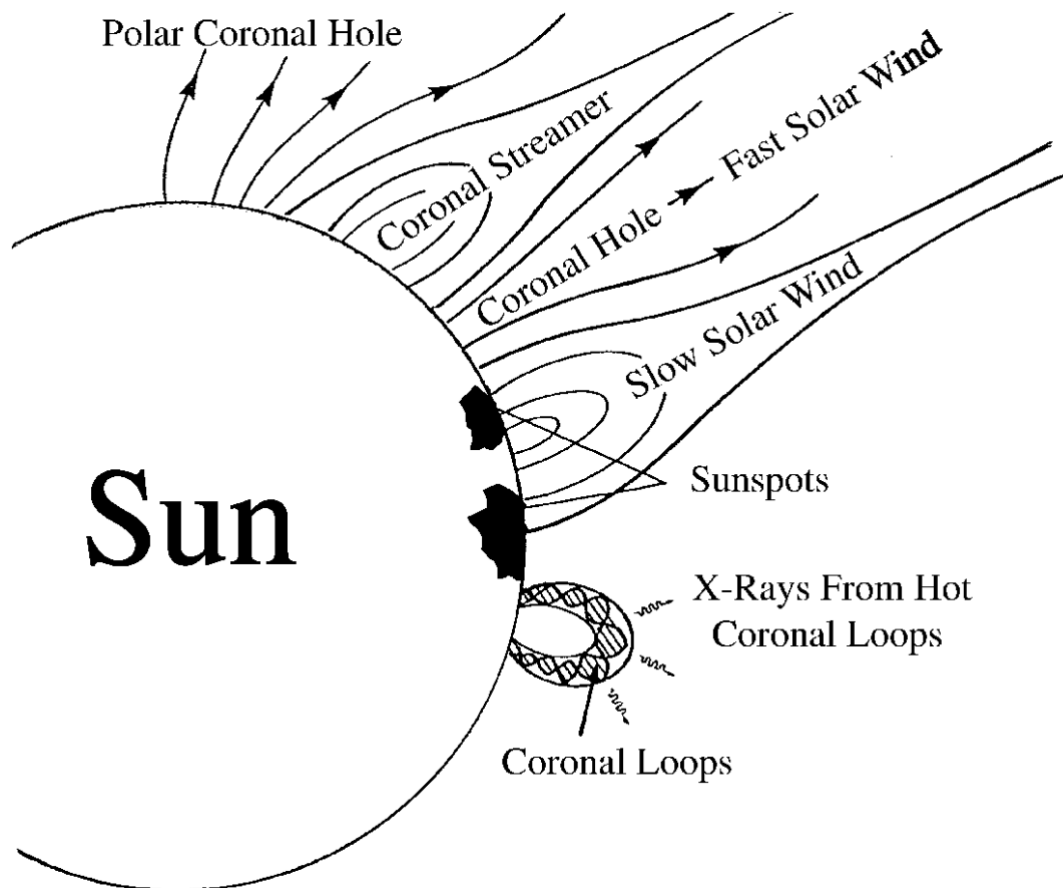
Figure 1. The Solar Corona and Solar Wind Generation (Schunk &
Nagy, Ionospheres, 2009).

contain as much as 10^{13} kg of plasma that expands as it travels with speeds as high as 1000 km s^{-1} (Schunk & Nagy, Ionospheres, 2009). This outward flow of plasma "freezes" and drags the solar dipole field lines with it into space. Due to the Sun's rotation, the trapped field lines bend radially forming a spiral known as the interplanetary magnetic field (IMF), extending deep into space, Figure 2.

Interplanetary Magnetic Field

Solar Wind

Sun
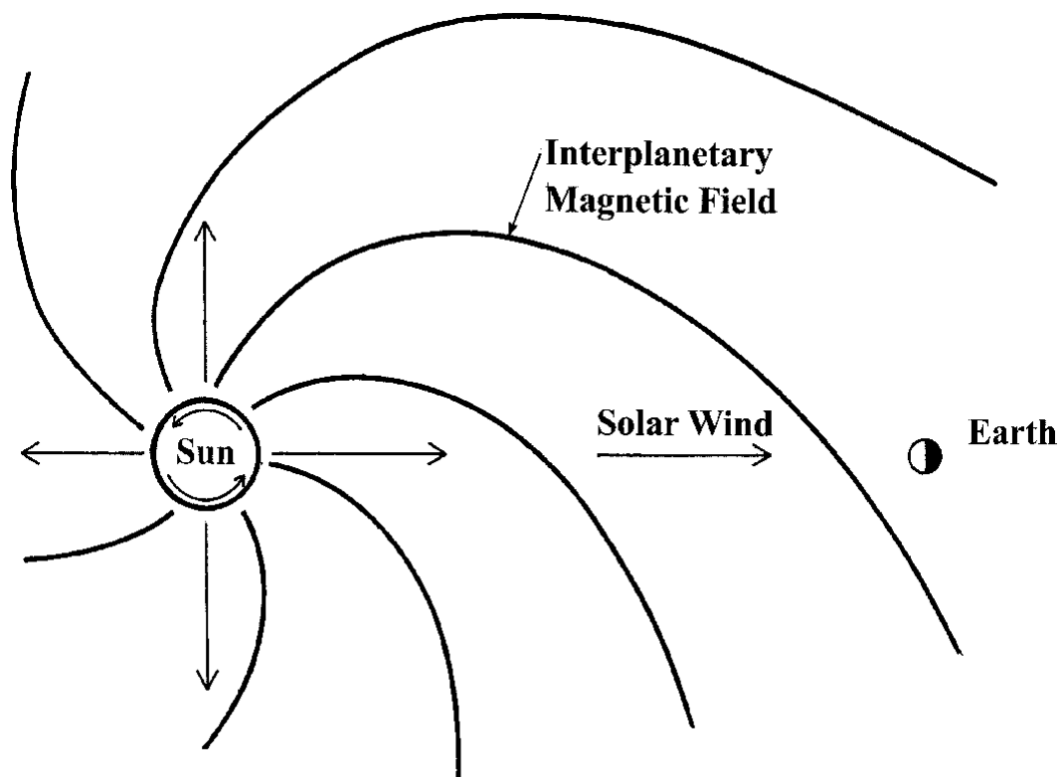
Earth

Figure 2. Sun's spiral magnetic field generated by the radial flow of the solar wind and the sun's rotation (Schunk & Nagy, Ionospheres, 2009).

Magnetosphere and Radiation Belts

At 150 million kilometers from the Sun, the Earth is protected from the onslaught of particles in the solar wind by its intrinsic magnetic field. Shielding from the Earth's

magnetic field creates a region isolated from the solar wind known as the magnetosphere, Figure 3. Unable to penetrate the closed magnetic field lines of the Earth's magnetosphere, the imposing solar wind forms a shock wave with a mean-free-path greater than the characteristic scale length for the change in density. This collisionless shock wave decelerates the supersonic flow of the approaching solar wind to a value below the plasma wave speed (Walt, 1994). Energy dissipated during this deceleration heats the plasma and the resulting subsonic stream can flow around the Earth's magnetic field. The region of subsonic solar wind around the Earth is known as the magnetosheath and is approximately 3 R_e (1 R_e = 6371 km) in thickness with particle energy significantly lower than the original solar wind.
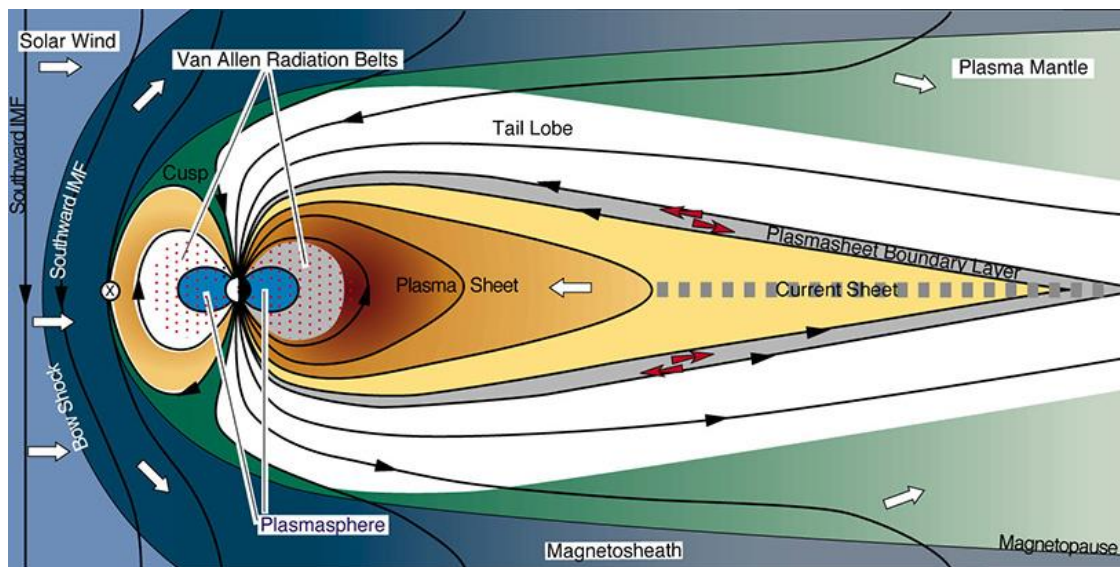
Figure 3. Diagram of the solar wind impinging on the magnetosphere (Parsec vzw, 2019)

Researchers often use the location of the boundary between the magnetosheath and the magnetosphere as a reference point when describing Sun-Earth interactions. This approximately 100 km thin boundary region known as the magnetopause is nominally

located at 9 R_e from the Earth's center and separates the solar plasma and magnetic field from the Earth's plasma and magnetic field. The actual location of the magnetopause along the Earth-Sun line is dynamic and dominated by the balance between the varying solar wind pressure in the shock region and the magnetic pressure of the Earth's compressed magnetic field. Balancing the pressure from the solar wind, the predominately dipole shape of the Earth's magnetic field beyond 7 R_e becomes distorted. On the sunlight side of the Earth, the nominal 10 R_e magnetosphere boundary is compressed to approximately 9 R_e. On the night side of the Earth, the reconnection of field lines results in an elongated magnetosphere tail extending several hundred Earth radii. This tail provides an important role in the transport of solar wind particles into the magnetosphere (Schunk & Nagy, Ionospheres, 2009).

Although the bulk of the solar wind is deflected, several mechanisms exist for a small fraction of these energetic particles, as well as terrestrial ions, to enter the inner magnetosphere. Once inside the magnetosphere, the original path of the charged particles is altered by the Earth's magnetic field causing some particles to be lost through collisions with the atmosphere and others to enter orbits bouncing between hemispheres along closed field lines. The trapping mechanisms for energetic particles results in stable belts of radiation around the earth. These regions of intense radiation are often referred to as the Van Allen belts, named after the early space pioneer who made the discovery. Due to the harmful effects of the radiation belts to humans and equipment in space and the national significance to obtain a presence in that environment, early explorers fervently sought to characterize these regions of trapped particles and understand their dynamics. There are two primary bands of radiation around the Earth; a stable inner belt consisting

predominantly of energetic protons and a dynamic outer belt of energetic electrons. Variations in the solar wind results in changes in the location, energy and composition of the radiation belts. With observations only possible from space and complex particle acceleration and transport mechanisms, some still not fully understood, the radiation belts continue to be a topic of discovery.

Ionosphere and Plasmasphere

The upper atmosphere consists predominately of N_2, O_2, O, H_e, and H and the densities decrease exponentially with altitude. Above 60 km, photoionization of the neutral atmosphere by solar ultraviolet, extreme ultraviolet and soft x-ray radiation creates a plasma resulting in a variety of chemical reactions and transport effects. Various day and night photochemical processes and transport mechanisms distribute the energy absorbed from the Sun about this region of the upper atmosphere. The spherical region from 60 km to beyond 1000 km is known as the ionosphere and this is the main location of plasma near the Earth, with a typical energy on the order of 0.1 to 2 eV. The ionosphere is represented in distinct regions based on the dominant processes for the production and loss of ions and electrons. These regions are denoted as the layers D, E, F1 and F2, with F2 having an order of magnitude greater plasma density than the other regions, Figure 4. Below 250 km the dominant ion O^+ is in chemical equilibrium and the density increases with altitude. Above 250 km the ion-atom interchange and transport processes begin to dominate and the O^+ density decreases. The peak of the F2 region is the altitude where chemical equilibrium and diffusive equilibrium are equivalent, resulting in a maximum density. A characteristic altitude for the F2 peak is between 250 km and 350 km, with an O^+ density of order 10^6 cm^{-3}. The region above the F2 peak

where O^+ remains the dominant ion is known as the topside ionosphere and it may extend

from 600 to 1500 km. Above about 500 km, diffusion and transport processes dominate

and the Earth's magnetic field influences the motion of the topside plasma.
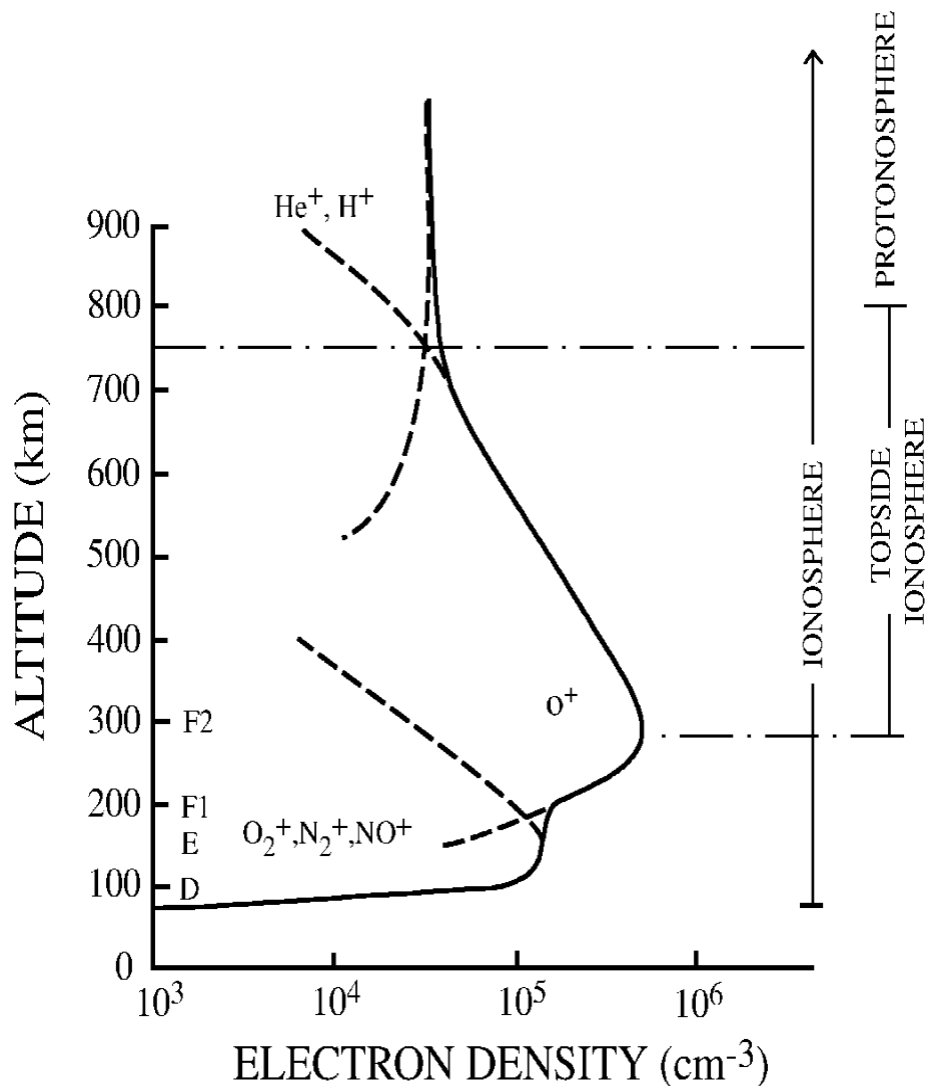
Figure 4. Electron density profile [solid line] for the mid-latitude
ionosphere in the D, E, and F layers and the topside ionosphere (Banks,
Schunk, & Raitt, 1976).

At high latitudes the geomagnetic field lines are open, connecting deep into the

tail of the magnetosphere. These open field lines result in dynamic ionospheric conditions

due to escaping topside plasma, precipitating energetic electrons from the cusp and

penetrating magnetospheric electric fields. At mid and low latitudes, the ring current establishes an opposing field canceling the magnetospheric electric field. This cancelation at mid-latitudes allows the topside plasma to co-rotate with the Earth and to travel between hemispheres along closed geomagnetic field lines in the inner magnetosphere. This region with closed magnetic field lines containing the cold plasma from the topside ionosphere is known as the plasmasphere.

The plasmasphere is toroidal in shape with an outer boundary equator crossing from 4 to 8 Re, depending on geomagnetic activity, Figure 3. In this region, the density of the cold plasma is on the order of 10^2 cm^{-3}, with the ion composition predominately H$^+$, but the region also contains He$^+$ and O$^+$. For geo-magnetically quiet conditions, diffusive equilibrium dominates and the ionosphere and plasmasphere are in equilibrium. Under these conditions, there is a gentle flow between the two regions from day to night. With increasing latitude, the volume of the plasmasphere mapped along field lines from a unit area in the ionosphere increases, resulting in a lower H$^+$ density at high altitudes. After a geomagnetic storm, the enhanced magnetospheric electric fields empty the plasma in the outer plasmasphere, causing an upward plasma flow from both hemispheres. At low latitudes, where the magnetic flux tube volumes are small, the flux tubes fill quickly. However, at high latitudes the depleted flux tubes may take days to refill and subsequent storms maintain a partially depleted state (Schunk & Nagy, Ionospheres, 2009).

Motivation for Proposed Research

Advances in the radiation belt models together with more recent observations indicate a greater population of low energy charged particles. The significance of a greater population of low-energy particles enables an opportunity for instances where the

trapped particle populations are comparable to the density in the surrounding plasmasphere. Under similar conditions, it is plausible that the two populations of charges particles could influence each other. The interaction of the similar and opposite charges between the cold plasma flowing along field lines and the hot particles trapped on the same field lines may create a boundary layer. Although the boundary layer between these two plasma populations may be small, it could still be important because of the impact the radiation belt has on space systems and national security, Appendix A. *Therefore, the purpose of this research is to evaluate the effect of the warm particles in the radiation belt on the distribution and transport of cold plasma in the plasmasphere, explore the characteristics of such an interaction and identify potential observables.*

CHAPTER II

IONOSPHERE-PLASMASPHERE AND RADIATION BELT MODELS

The intent of this study is to examine the effect of the warm particles in the

radiation belts on the distribution and transport of cold plasma in the plasmasphere. The

environment representing these two coexisting regions is obtained using two global

models, IPM and AE9AP9. A brief introduction to these models is described next.

Ionosphere-Plasmasphere Model (IPM)

The Ionosphere-Plasmasphere Model (IPM), originally designed as a low and

mid-latitude physics-based model of the ionosphere-plasmasphere system, was

constructed via a numerical solution of the ion and electron transport equations (Schunk,

Eccles, Sojka, Thompson, & Zhu, 2003). Afterwards, IPM was extended to high latitudes

providing an integrated global solution. The IPM calculates 3-dimensional, time-

dependent, density distributions along magnetic field lines for four major ions (NO^+, O_2^+,

N_2^+, O^+) at E-region altitudes and three major ions (O^+, H^+, He^+) in the F-region,

plasmasphere and polar wind. The model takes account of the following physical

processes: (1) Field-aligned diffusion due to density and temperature gradients, gravity,

and the ambipolar electric field; (2) cross-field electrodynamics drifts due to co-

rotational, dynamo (wind driven), and magnetosphere electric fields; (3) ion production

due to UV and EUV solar radiation, resonantly scattered solar radiation, starlight, and

auroral electron precipitation; (4) numerous energy-dependent chemical reactions; and

(5) neutral wind, composition and temperature changes. However, the plasma bubble

formation in the F-region ionosphere is not considered. The IPM solves electron and ion

energy equations at high latitudes, but an empirical model is used for the plasma

temperatures in the plasmasphere (Titheridge, 1998), because the standard collision-

dominated energy equations are not rigorously valid in this region.

The IPM is based on the International Geomagnetic Reference Field (IGRF),

IGRF
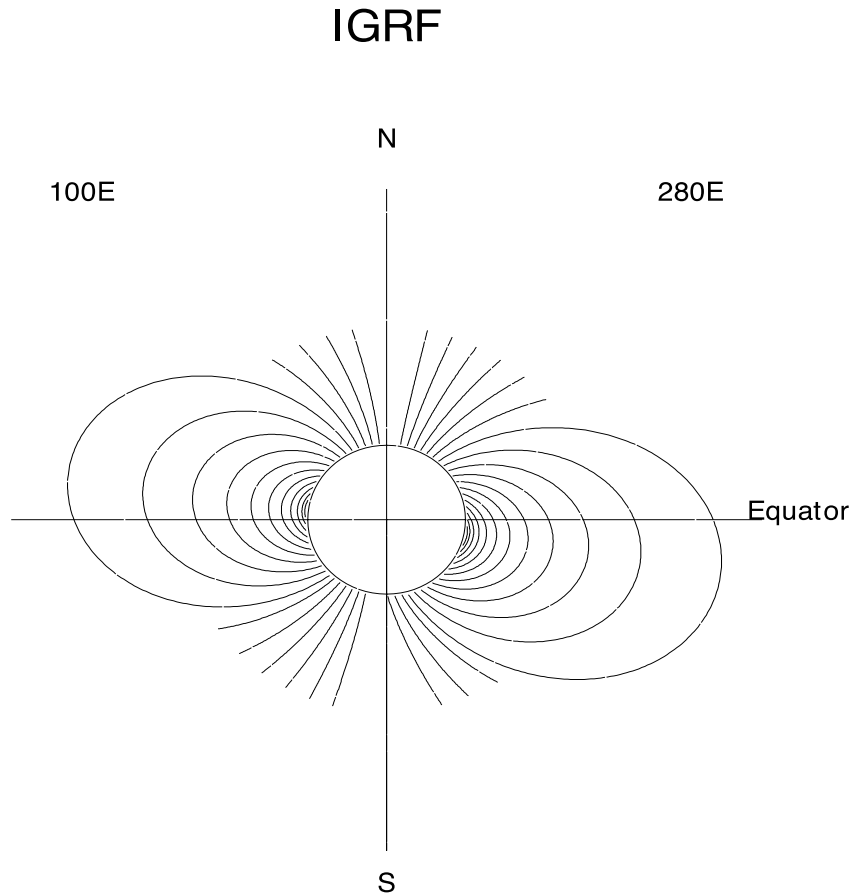
Figure 5. Magnetic field structure for the IPM model, showing open
field lines at high latitudes and closed field lines at mid and low
latitudes (Schunk, et al., 2004).

which accounts for effects due to the offset in the Earth's graphic and magnetic equators,

Figure 5. The model allows the plasmapause to vary, expanding and contracting in

response to changes in the magnetospheric electric fields. During low geomagnetic

activity the plasmapause is typically located at L = 6, however the plasmapause may be compressed to L = 4.5 during periods of high geomagnetic activity (European Space Agency, 2013). Beyond the plasmapause the magnetic field lines are open. IPM allows magnetic field lines to open and close as dictated by the storm-time electric fields and the location of the plasmapause. IPM uses an Euler-Lagrange numerical scheme, where the transport equations are solved along a magnetic field line for convecting plasma flux tubes up to L = 5.7 (30,000 km). This approach allows the plasma in the outer plasmasphere to drift away from the Earth during storms due to the magnetospheric electric fields. The global nature of the model is obtained by following thousands of plasma flux tubes.

The spatial and temporal resolutions of the model are adjustable, and the model outputs plasma densities, drift velocities, and temperatures. The global and time-dependent inputs to IPM are the neutral densities, temperatures, and winds, and the dynamo and magnetospheric electric fields which were obtained using the default physics-based and empirical models. The default models provided with IPM are: the MSIS-90 model for the atmospheric densities (Hedin, 1991); the HWM for the neutral winds (Hedin, et al., 1991); the Weimer model (Weimer, 2001) for the magnetosphere electric fields; the Hardy model (Hardy, Gussenhoven, & Holeman, 1985) for the electron precipitation; and the Scherliess and Fejer model (Scherliess & Fejer, Radar and Satellite Global Equatorial Vertical Drift Model, 1999) for the equatorial electric fields.

Sample Plasma Density from IPM Simulations

Season, local time, along with solar and geomagnetic activity drive variation in the ionosphere and plasmasphere density. These variations can be represented by

describing four cases in the northern hemisphere (NH), 1) summer; high solar and geomagnetic activity, 2) winter; high solar and geomagnetic activity, 3) summer; low solar and geomagnetic activity, 4) winter; low solar and geomagnetic activity. The background ionosphere-plasmasphere density was simulated for these four cases using IPM each producing four species, H^+, O^+, He^+ and total ion density, for four local times. Details pertaining to the specific parameters chosen for the simulations will be discussed in Chapter 3, however it suffices to state that these four cases span the diurnal, latitudinal, seasonal, and solar cycle plasma density variations observed in the ionosphere and plasmasphere.

In Figure 6, the four panels depict the total ion and species density for the dominate ions in the ionosphere and plasmasphere; H^+, O^+ and He^+. This comparison is provided as a visual aide in correlating the species having the greatest influence on the total density. In each panel, the density along the magnetic field lines with equator crossing altitudes from 600 km to 20,050 km is represented by a color ranging from dark blue to red. For all panels in a figure the same scale is used to correlate density to color. In panel a) above L=3, the total density is dominated by H^+ corresponding to the same region and color in panel b). At lower altitudes, the total density, panel a) is dominated by O^+ corresponding to the same region and color at the bottom of panel c). In panel d) the maximum He^+ is around 10^3 cm^{-3} at low altitudes and decreases to about 30 cm^{-3} in the region of study, L = 3.5 and 4, only a modest contribution to the total density.

In Figure 7, the distribution of O^+ density for case 1, NH summer solar maximum conditions, was selected to depict diurnal response in the lower plasmasphere and ionosphere. Each of the four panels in Figure 7 contains a plot corresponding to the local

time, 6 am, noon, 6 pm and midnight at 270 degrees longitude. The four panels in Figure

7 track the development of the ionosphere due to solar illumination starting at sunrise

through noon and into sunset. After sunset, production ceases and the ionosphere decays

throughout the night due to chemical recombination until sunrise where the process

repeats. At its peak, around 300 km, the O^+ ion population has a density around ~10^6 cm^{-3}

and daytime densities increasing by an order of magnitude as high as 5000 km altitude.

No O^+ ions are transported above 12,500 km. Figure 8 presents the O^+ density for the

four study cases at 270° longitude and noon local time. The four panels are arranged to

highlight density changes due to seasonal and solar activity. Selecting the simulation day

at the equinox, day 90 or 270, the two hemispheres would receive nearly equal

distribution of solar illumination. As a result, the production of O^+ in the northern

hemisphere would be near equivalent to the production in the southern hemisphere and

the ion distribution would be nearly symmetric about the geographic equator. A

comparison between NH summer, day 180, and NH winter, day 360, panels in Figure 8

indicates the seasonal effects result in an order of magnitude increase in the altitude

extent of O^+ up to 5000 km in the summer hemisphere. The top row, panels a and b in

Figure 8, were generated for solar maximum conditions. Comparing solar maximum

panels on the top row to the solar minimum on the bottom row, the lower solar activity

reduces the peak density by a factor of two but also decreases upward transport by 20%

to 40% in altitude extent.

Figures 9 and 10 are similar in format as Figures 7 and 8 but represent the NH

summer solar maximum H^+ density, the dominant ion in the upper plasmasphere. Panels a

through d in Figure 9 indicate that local time variations of H^+ density are observed across

mid and low-latitudes below 5000 km altitude. In this region the average density is around 10^4 cm^{-3} and varies from high to low by an order of magnitude. H^+ is transported to higher altitudes along magnetic field lines by diffusion. Additionally, magnetospheric electric fields result in $\mathbf{E}$ x $\mathbf{B}$ drift transporting H^+ to outer field lines. Within the region of study, L = 3.5 to 4, the equator crossing density decreases from 900 to 500 cm^{-3} with no observed diurnal variation. Figure 10 represents the H^+ density at noon local time for the four study cases. The four panels are arranged to highlight density changes due to seasonal and solar activity. A comparison between NH summer and winter in Figure 10 indicates the seasonal effects at mid and low latitudes could be an order of magnitude below 5000 km but as little as 10% in the upper plasmasphere.

A single flux tube was selected to explore the outer plasmaspheric density in greater detail and identify the conditions bounding variations. The density and morphology of the plasmasphere does not vary significantly from L = 3.5 to L = 4 and for reasons that will be explained in Chapter 3, the flux tube corresponding to L = 3.9 and having an equator crossing altitude of 18,500 km was selected for comparison. The three panels in Figure 11 depict the IPM density for H^+, He^+ and O^+ at 18,500 km altitude above the equator (L = 3.9). Each plot in Figure 11 displays the hourly ion density for two days during solar minimum and maximum conditions. For seasonal comparisons days, 180 and 360 were selected corresponding to northern hemisphere summer and winter.

The O^+ density represented in Figure 11 panel c), indicates the greatest diurnal variation changing by a factor of 10 throughout the day in summer. While the He^+ density, panel b, indicates the greatest variation in solar cycle with a factor of 6 increase

over solar minimum. However, H^+ with a density an order of magnitude greater than He^+ and more than three orders of magnitude greater than O^+ dominates any fluctuations in the plasmasphere in this region. With nearly no variability throughout the day, H^+ density in this region increases by a factor of three from solar minimum to solar maximum and a factor of two during northern hemisphere winter (day 360) over summer (day 180).

Combining the three ions into a total density, the four conditions of study are easily compared for the flux tube along L = 3.9. As shown in Figure 12, the total density has a maximum value of 1500 cm^{-3} above the equator during solar maximum when the northern hemisphere is in winter, day 360. In contrast, the minimum total density over the equator is approximately 250 cm^{-3} and occurs during solar minimum conditions when the northern hemisphere is in summer. Bounding the range of the plasmaspheric density allows a comparison to the energetic particle density from the radiation belt and an early assessment of the expected interaction of the two populations. Additionally, identifying the conditions bounding the plasmaspheric density and the region of interest reduces the combination of simulation necessary for this study.

H⁺, O⁺ & He⁺ Contribution to Total Ion Density (Noon Local Time)

a) Total Density

b) H+ ion density

c) O⁺ ion density

d) He⁺ ion density
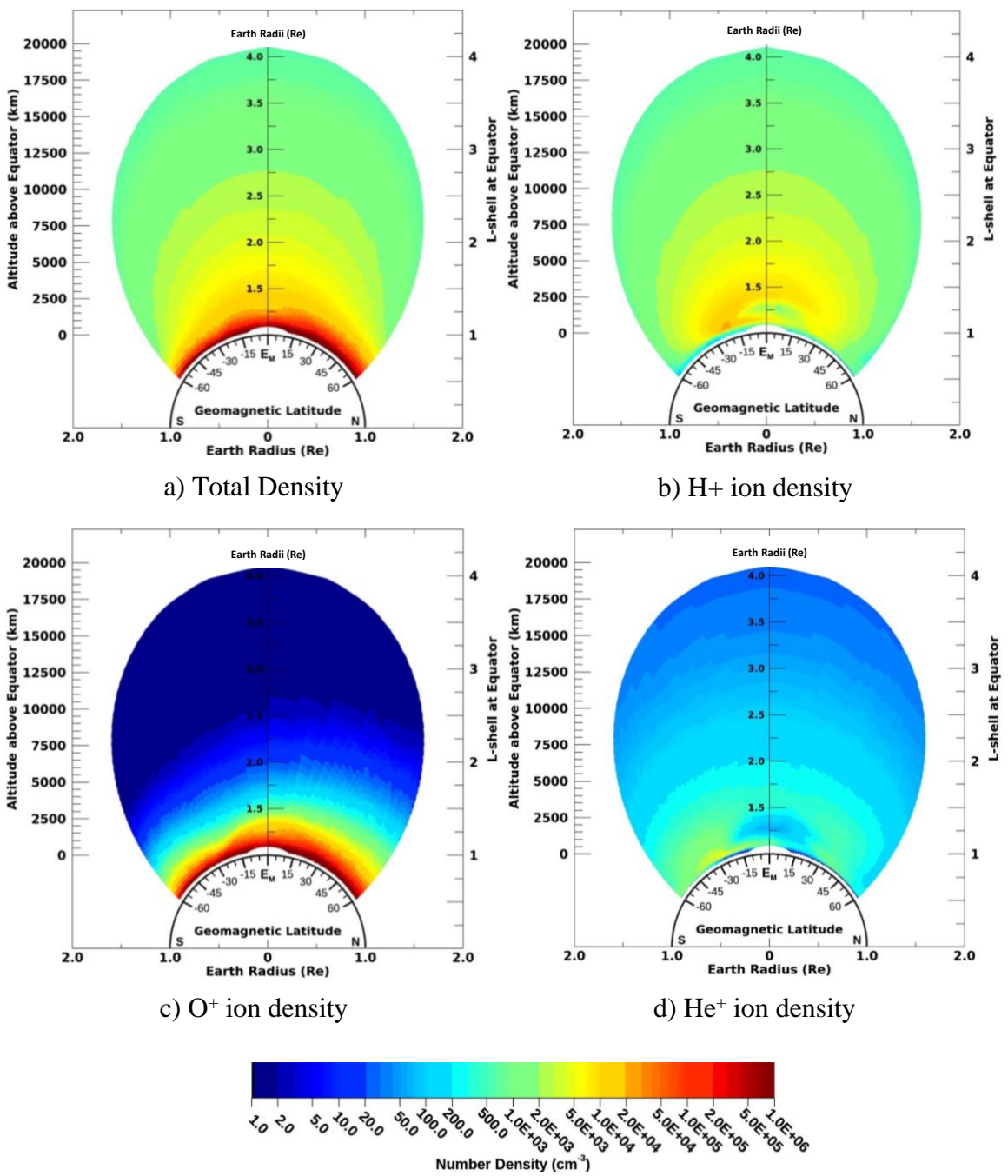
Figure 6. IPM total density for H⁺, O⁺, and He⁺ at 270° longitude and local noon during solar maximum conditions. Above L = 3 the total density is dominated by H⁺ as seen in (b) with a nominal density about 10^3 cm⁻³. Below 2500 km, the total density is mostly O⁺ as seen in (c). At 300 km, a typical peak density is 10^6 cm⁻³ and decreases by three orders of magnitude in the plasmasphere.

O⁺ Density Variations due to Local Time
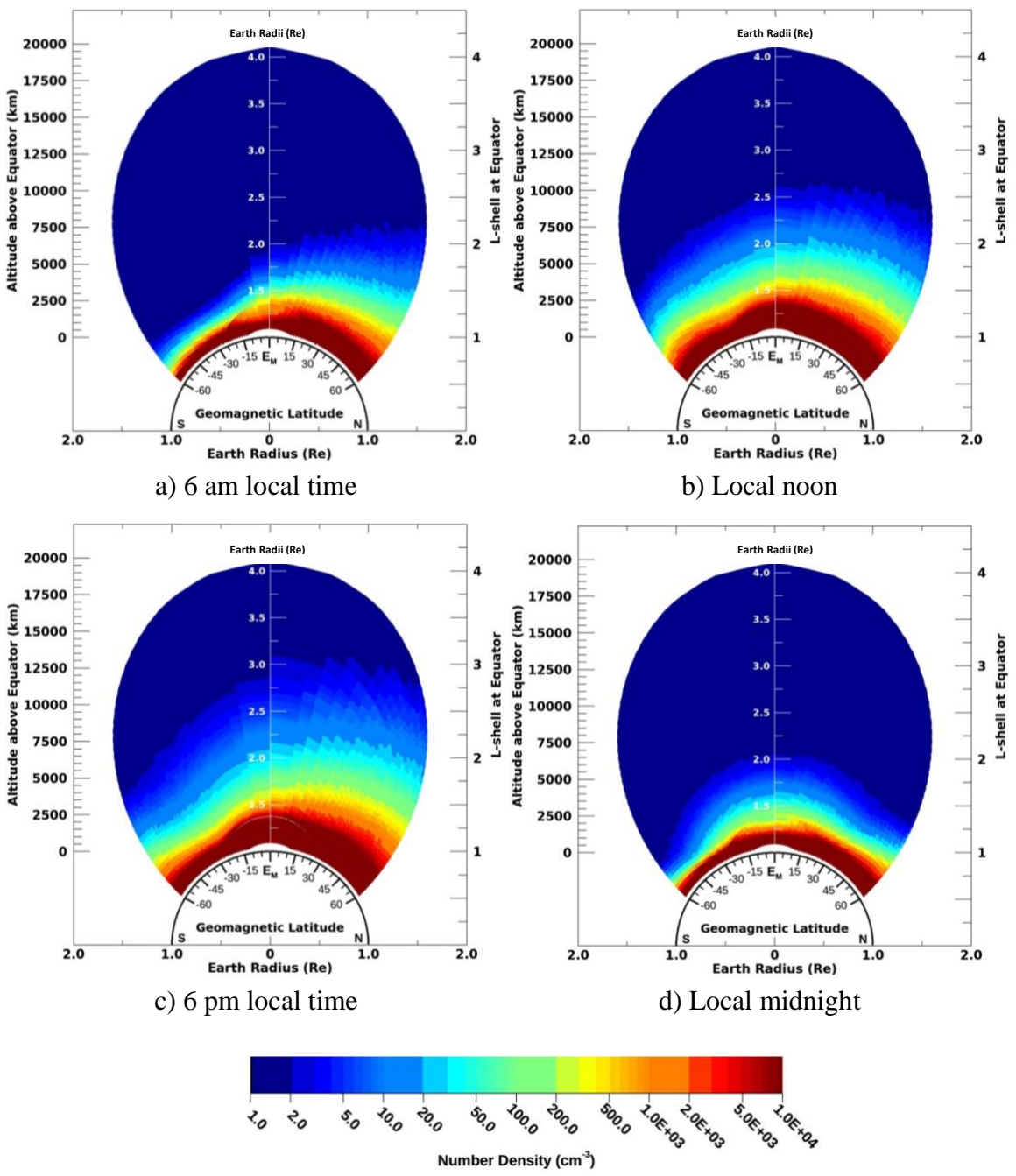
Figure 7. IPM O⁺ density every 6-hours for northern hemisphere summer, day 180, solar maximum conditions and at 270° longitude. O⁺ density is greater in the northern hemisphere due to the increased solar illumination. At sunrise (a) photoionization creates O⁺ in the ionosphere. By noon (b) the ionosphere is fully developed with O⁺ diffusing along field lines to higher altitudes. The density increases until sunset (c), when production ends and the ionosphere decays through chemistry (d).

Season and Solar Activity Impact on O$^+$ Density (Noon Local Time)

a) Solar maximum, day 180 (summer)

b) Solar maximum, day 360 (winter)

c) Solar minimum, day 180 (summer)

d) Solar minimum, day 360 (winter)
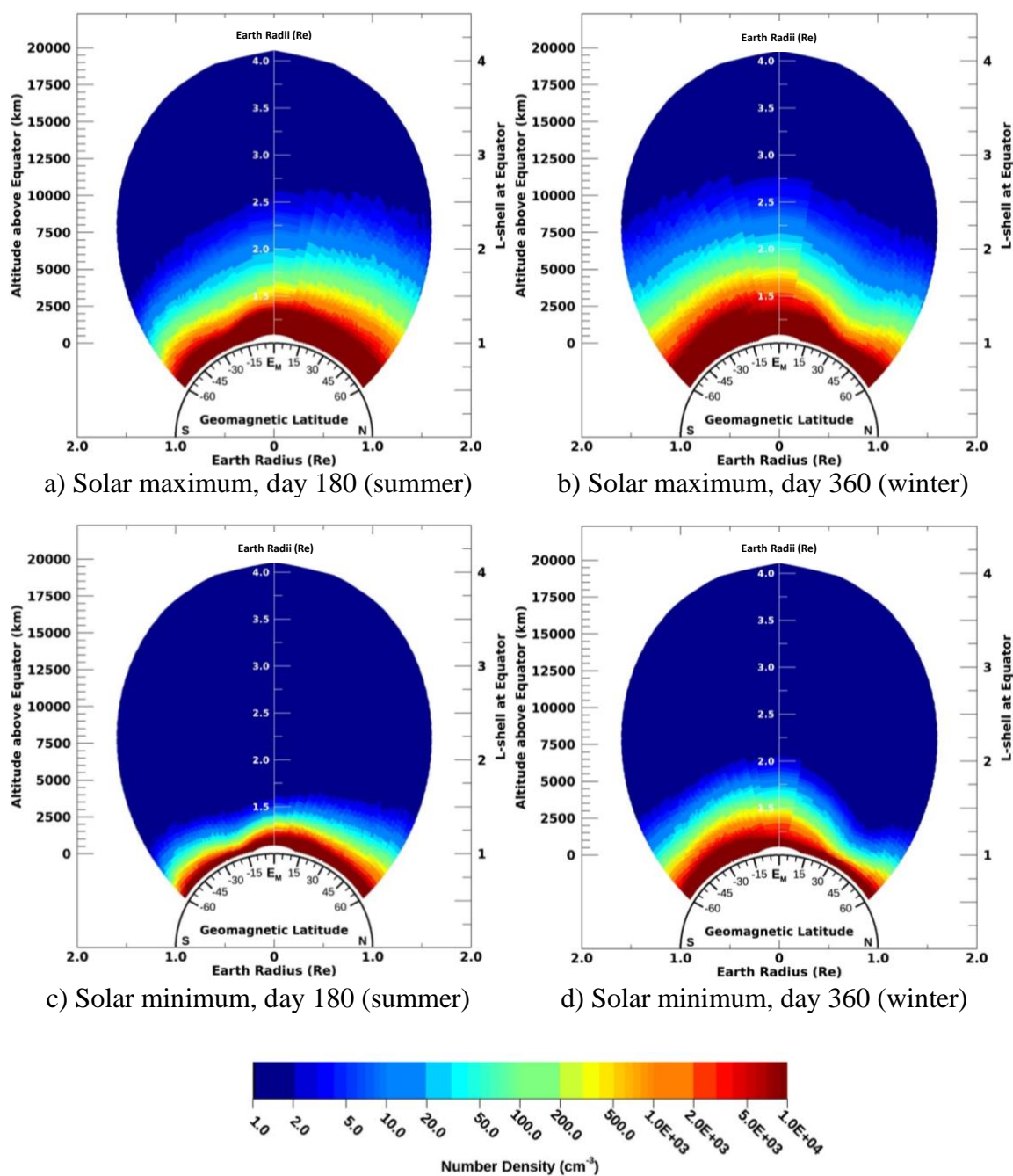
Figure 8. IPM O$^+$ density for the four study cases at 270° longitude and noon local time. Comparing summer (a) and winter (b), a strong seasonal dependence of O$^+$ production is observed with the greatest density ~10^6 cm^{-3} in the sunlit hemisphere. Less dramatic are the differences in the ionosphere for low solar activity (c) and (d). Comparing solar maximum, (a and b) to solar minimum (c and d), the peak density is a factor of two lower with decreases in upward transport by 20% to 40%.

H⁺ Density Variations due to Local Time

a) 6 am local time

b) Local noon

c) 6 pm local time

d) Local midnight
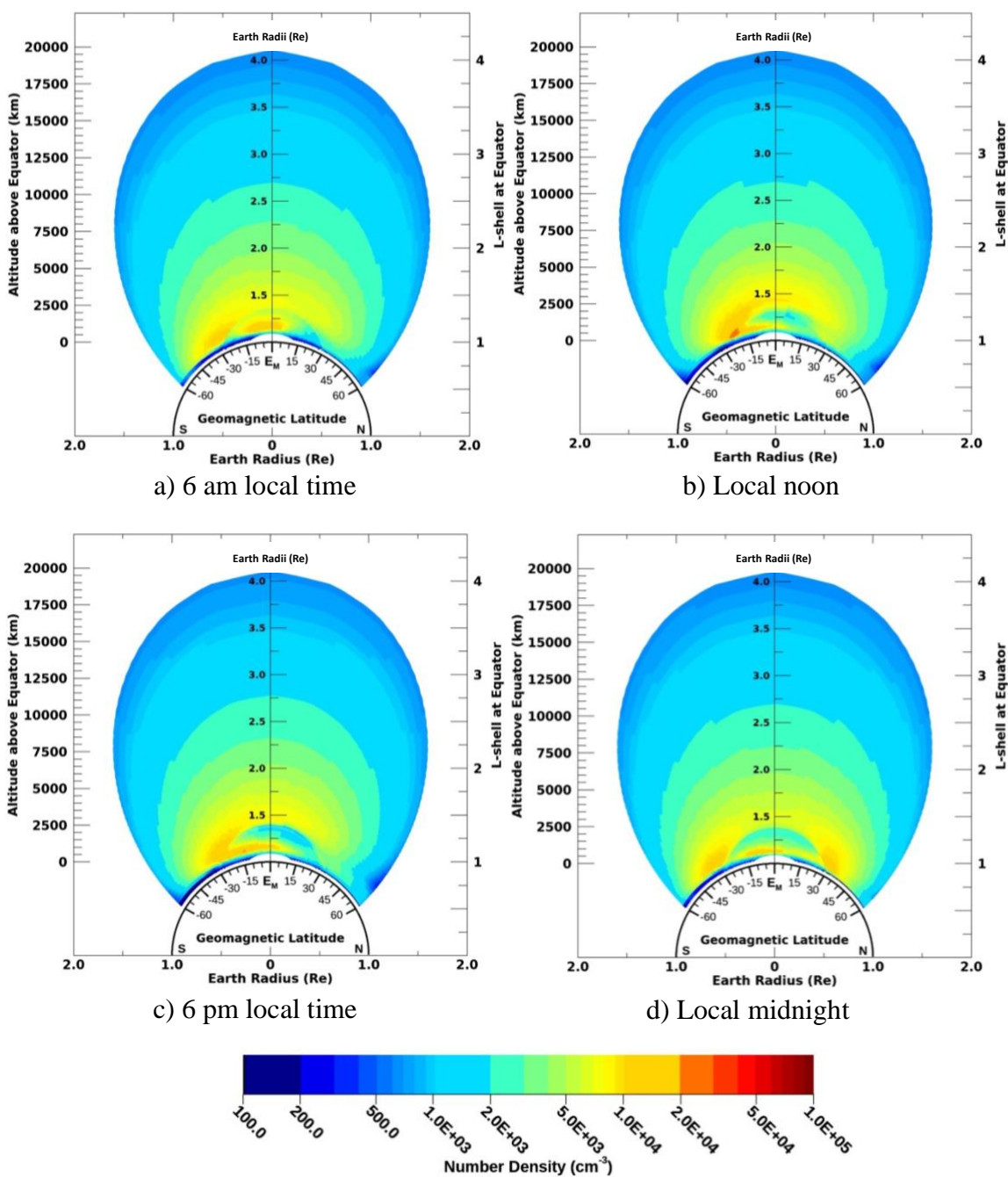
Figure 9. IPM H⁺ density at 6-hours intervals for northern hemisphere summer, day 180, solar maximum conditions and at 270° longitude. The greatest H⁺ density is 2.0 x10⁴ cm⁻³ at mid latitudes and below 5000 km equator crossing altitude with fluctuation about an order of magnitude. Transport from lower altitudes along and across magnetic field lines fills the plasmasphere. In the region of study, L = 3.9, density at the equator is ~ 700 cm⁻³ with no observed diurnal variation.

Season and Solar Activity Impact on H⁺ Density (Noon Local Time)

a) Solar maximum, day 180 (summer)

b) Solar maximum, day 360 (winter)

c) Solar minimum, day 180 (summer)

d) Solar minimum, day 360 (winter)
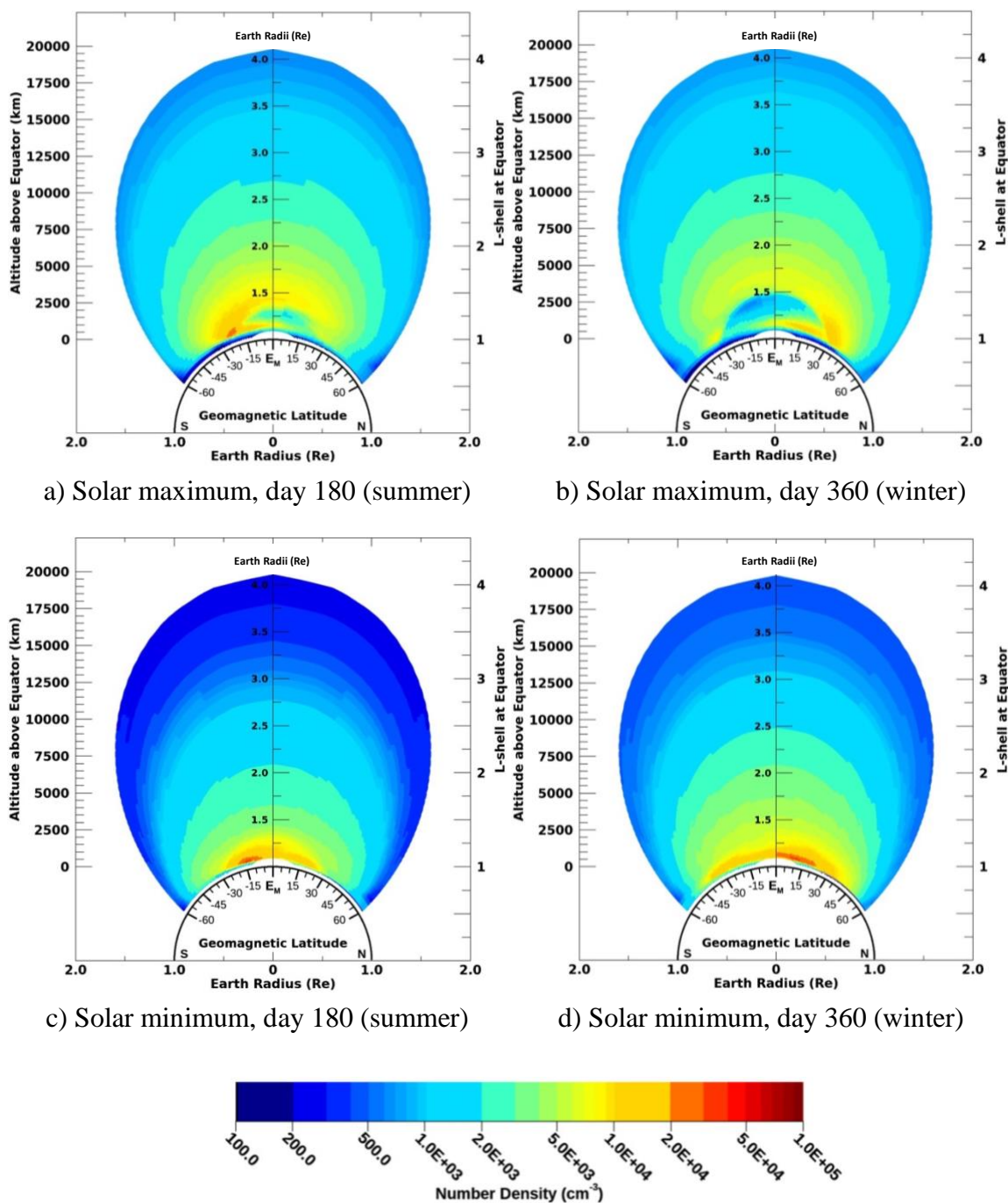
Figure 10. IPM H⁺ density for the four study cases at 270° longitude and local noon. Comparing summer and winter, the panels show that seasonal effects below 5000 km at mid and low latitudes may be a factor of 10, yet less than a factor of 2 in the upper plasmasphere. Comparing solar maximum, (a and b), to solar minimum, (c and d), along L = 3.9 at the equator, the H⁺ density changes by a factor of 3.

Hourly, Season and Solar Activity Variation in Ion Density at 18,500 km
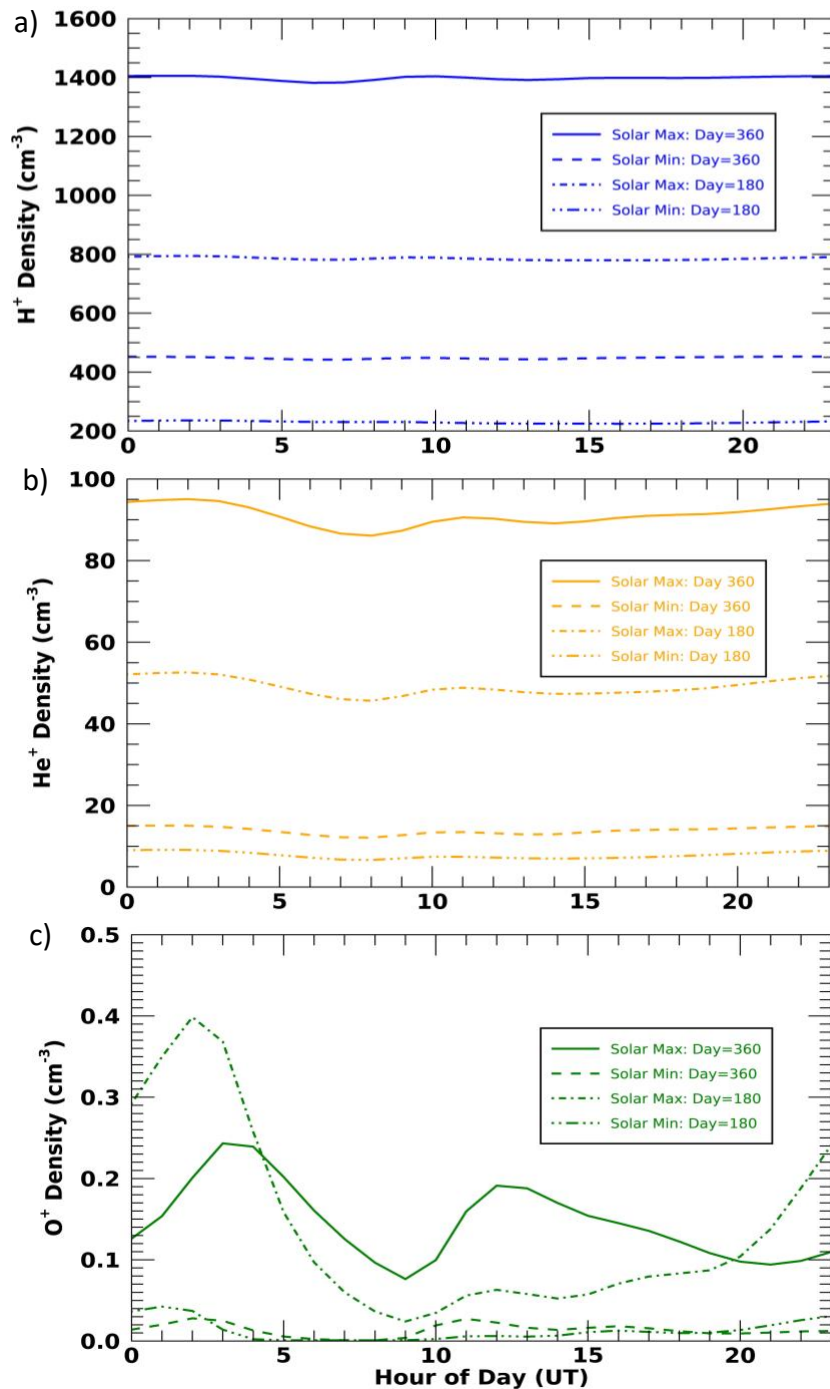
Figure 11. Hourly variations of H^+, He^+ and O^+ density at 18,500 km above the equator for the four study cases. The O^+ density, panel c, varies by a factor of 8 throughout the day. The He^+ density, panel b, increases by a factor of 6 from solar minimum to solar maximum. The H^+ density, panel a, with the greatest abundance and least variation, dominates the behavior of this region.

Season and Solar Activity Impact on Total Density (Noon Local Time)
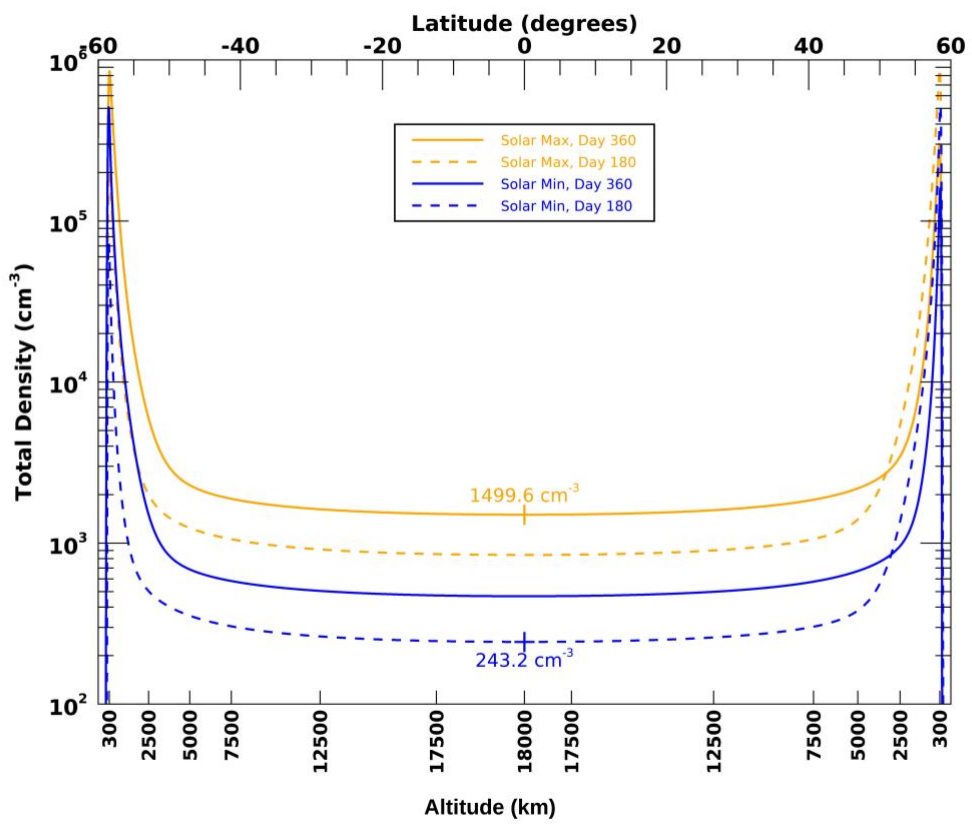
Figure 12. Total plasmaspheric ions, H^+, He^+ and O^+, plotted along the flux tube L = 3.9 for solar maximum day 360 and 180 and solar minimum day 360 and 180. These four cases bound the range of background density for the study.

Radiation Belt Model

Since the discovery of the inner and outer radiation belts by Van Allen (Van Allen,

Ludwig, Ray, & McIlwain, 1958), ongoing observations and theoretical studies have

depicted the unique characteristics of these two regions, Figure 13. The outer belt is the

most dynamic of the two, extending between $3.5 < L < 7$, where L, known as the
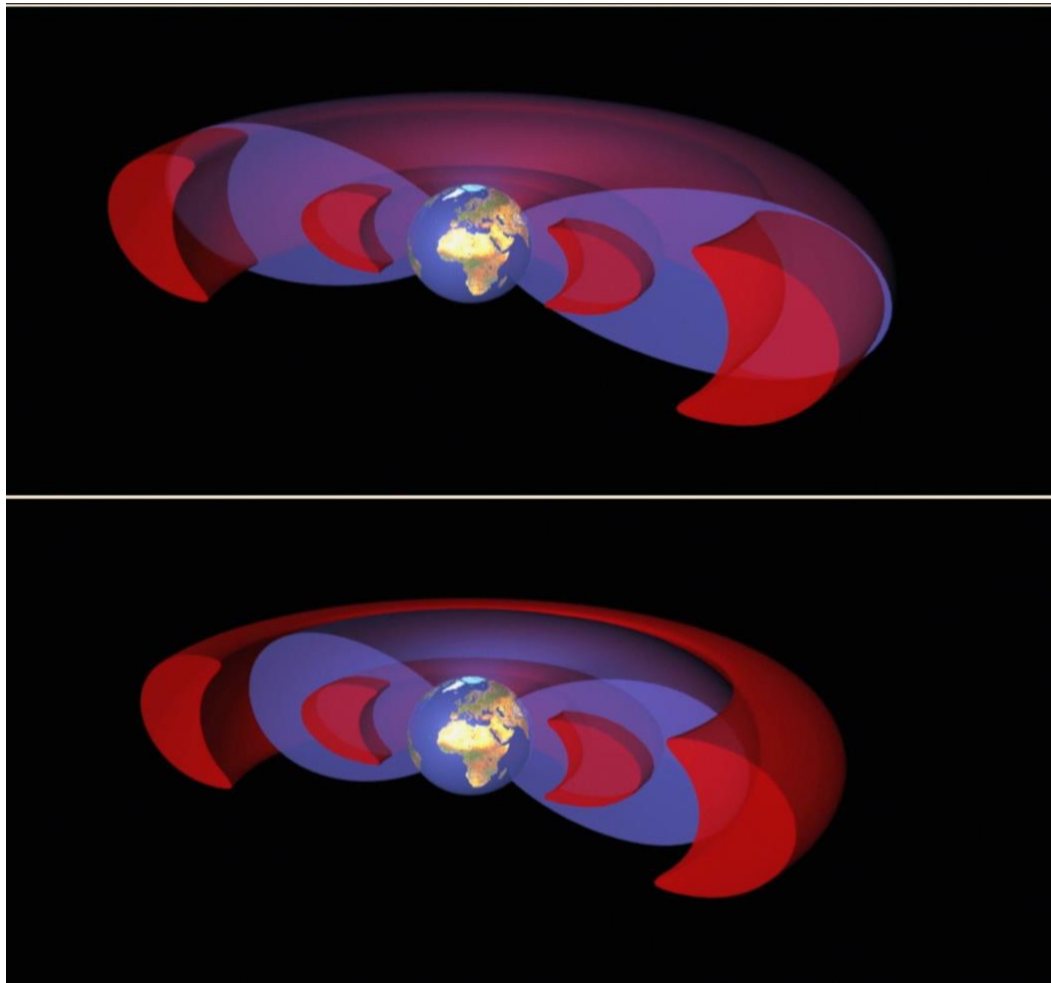
Figure 13. Diagram depicting the location of the plasmasphere with
respect to the radiation belts. The regions in red represent the locations
of the inner and outer radiation belts. The plasmasphere is depicted in
blue during low (top panel) and high (lower panel) geomagnetic
activity. Not shown is the temporary belt of relativistic electrons and
trapped warm ions in the "slot" region between the inner and outer
belts (European Space Agency, 2013).

McIlwain index (McIlwain C. E., 1961), provides a simple representation for magnetic field lines. Additional details about the McIlwain index is given in Appendix B, which also includes a description of charged particle motion in a magnetic field, the basic physics of particle trapping, particle motion in non- uniform magnetic fields, geomagnetic particle trapping, and the formation of the ring current. Appendix C provides more information about radiation belt characteristics, including the outer belt, resonant wave-particle interactions, radial diffusion, the Slot region, the inner belt, radiation belt variability, and the penetrating solar wind.

Due to the significant spatial and temporal variations of the outer belt during strong geomagnetic activity, the outer belt has undergone the most extensive research (Zou, et al., 2011). The largest flux for the outer belt is at L = 4, consisting predominately of relativistic electrons (>1 MeV) and to a less extent ions (10 keV to 10 MeV) (Singh, Singh, & Siingh, 2011).

In contrast, the inner radiation belt, spanning L = 1.2 to 2.3, is considered relatively stable with some highly energetic protons trapped for several hundred years (Farley & Walt, 1971). Theoretical modeling consistent with observations indicate that this region is predominately comprised of trapped energetic protons (15 to 170 MeV) from cosmic ray albedo neutron decay and lower energy solar protons (<100 MeV) from radial inward diffusion (Selesnick, Looper, & Mewaldt, 2007). Analysis of inner belt fluxes across the solar cycle indicate an anti-correlation of protons below L = 1.3 with F10.7, a proxy for solar activity. The main cause of decreased proton flux during high solar activity is due to the increase in particle collisions with the neutral atmosphere (Kuznetsov, Nikolaeva, & Panasyuk, 2010; Miyoshi, Morioka, & Misawa, 2000).

A recent analysis of data during geomagnetic storms indicates that the radiation environment in the inner magnetosphere may be more variable than previously thought. Data from three NOAA POES satellites were analyzed for large geomagnetic storms and found a loss of high energy protons on the outer regions of the inner belt (Zou, et al., 2011). Between the inner and outer radiation belts, 2.5< L<3.5, known as the "slot"
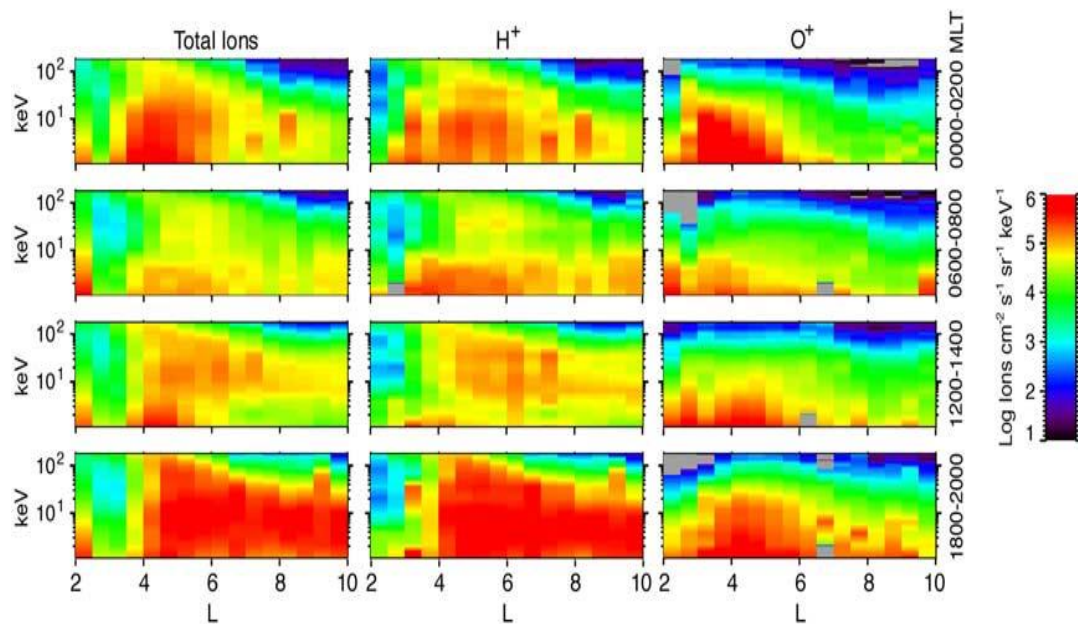
Figure 14. Spectrograms of energy verses L-shell for the total ion flux, H^+ and O^+ at four local times observed by instruments aboard the NASA Polar Satellite. From L = 3 to 4, two orders of magnitude change are observed between midnight and noon magnetic local time (Roeder, Chen, Fennell, & Friedel, 2005).

region due to the absence of energetic electrons, data from the NASA Van Allen probes detected a third temporary belt of relativistic electrons during periods of intense geomagnetic activity (Baker D. N., et al., 2004). Analysis of particle measurements from sensors aboard the NASA Polar satellite indicated the existence of large populations of energetic ions. In the region of interest, L = 3 to 4, these larger populations of particles

consist of H^+ and O^+ ions with considerably lower energy, 1-200 keV, than associated with the radiation belts, Figure 14. Additionally, these trapped ions exhibit significant variations in magnetic local time (Roeder, Chen, Fennell, & Friedel, 2005).

AE9AP9 Model

Based on flux maps derived from measurements onboard the first satellites in 1958, NASA sponsored the development of empirical radiation belt models. By the mid-sixties, several empirical models were available to guide engineers in the hazards of the space environment for designing systems and planning human flights. Incremental evolution of multiple models led to the release of AE-8 for the average electron flux in 1980 and AP-8 for protons, spawning several variants tailored to specific needs of the community. In the years that followed, NASA sponsored numerous measurements and models spanning the entire inner magnetosphere. However, each model had various spatial, temporal or energy range limitations. Although the NASA models were more advanced and supported the scientific community, they were not engineering friendly. Despite the limitations in AE-8 and AP-8, for several decades these models remained the space engineering design standard for specifying the radiation environment (Ginet, et al., 2013).

With the increasing complexity of space systems, the engineering techniques to optimize performance and cost required an improved representation of the radiation environment. A single comprehensive model including uncertainty estimates, probability distributions, and a larger spectral range was needed to support the community. Through government sponsorship, a 5-year community effort was undertaken to develop a new set of models addressing the previous limitations but also providing a framework to

incorporate future measurements. In keeping with the previous naming convention, the new models were designated AE9 for the trapped energetic electrons, AP9 for the trapped energetic protons, and SPM for the "warm" space plasma. These new models were validated, documented, combined together along with tools for the user and released to the community in September 2012 as AE9AP9.

The AE9AP9 model incorporates 33 satellite data sets starting as early as July 1976. Measurements range in energy from 0.05 to 10.0 MeV for electrons, 0.1 to 400 MeV for protons and 1.0 to 63.0 keV for the plasma. These data sets underwent an extensive data cleaning and a comprehensive cross-calibration using a spectral inversion technique. A new statistical methodology was applied for producing realistic flux probability distributions along a specific orbit. Internally, the AE9AP9 models employ coordinates invariant over the drift-bounce motion of the particles. The primary coordinates are $<E, K, \Phi>$, where E is the particle energy and K is the modified second adiabatic invariant for the bounce motion given by

$$K = \int_{S_m}^{S_{m'}} [B_m - B(s)] ds, \tag{2.1}$$

where B is the magnitude of the magnetic field line along a particle trajectory s from mirror points s_m to $s_{m'}$ at magnetic field B_m. The parameter Φ is the third invariant capturing the particle's drift motion,

$$\phi = \oint d\boldsymbol{L} \cdot \boldsymbol{A}, \tag{2.2}$$

where $\boldsymbol{A}$ is the magnetic vector potential and $\boldsymbol{L}$ is the entire drift shell of the particle. At the loss cone, Φ does not accurately represent the flux variations so an additional coordinate h_{min}, defined as the minimum altitude a particle reaches during its drift-bounce orbit, is used below 1000 km. Finally, a neural network interpolation algorithm is used to

reduce the computation demands for integration over the 3-D volume (Ginet, et al., 2013).

Recognized as an improvement over AE8 and AP8 for numerous reasons, the inclusion of the "warm" space plasma model drove the selection of AE9AP9 for this study. Although a few models representing low-energy plasma radiation observations already existed, the development of an integrated model suite and the establishment of a framework for incorporating new data meant AE9AP9 provided the greatest opportunity for future research as new measurements became available. At the beginning of this study, AE9AP9 version 1.30.001 became available and this version was maintained throughout this study to simplify software interfaces as described in Appendix D. However, the O^+ and He^+ models in SPM were limited to a single data set, Polar CAMMICE/MICS, and the lack of an extensive collection to characterize the trapped "warm" plasma resulted in several model limitations pertinent to this study. These limitations included the absence of solar cycle dependence along with large uncertainties for in the inner radiation belt protons (< 20 MeV) and no magnetic local time dependence in the SPM model. In spite of these limitations the results from AE9AP9 will be sufficient to represent the radiation environment and bound the effects on the plasmasphere.

Sample Radiation Flux from AE9AP9 Simulations

AE9AP9 was run for different time periods to examine the energy dependence, spatial distribution, and temporal variability of the proton and ion fluxes in the radiation environment. Initially, AE9AP9 simulations were conducted using all four study conditions, solar minimum and maximum during northern hemisphere winter and

summer. As previously identified in the limitations of the model, the output was invariant

for the four conditions reducing the study to only one canonical background radiation

environment for 2001, day 180 and UT 1200. However, the results were sufficient to

compare the expected inner belt morphology to the less recognized distribution of the

lower energy radiation environment.
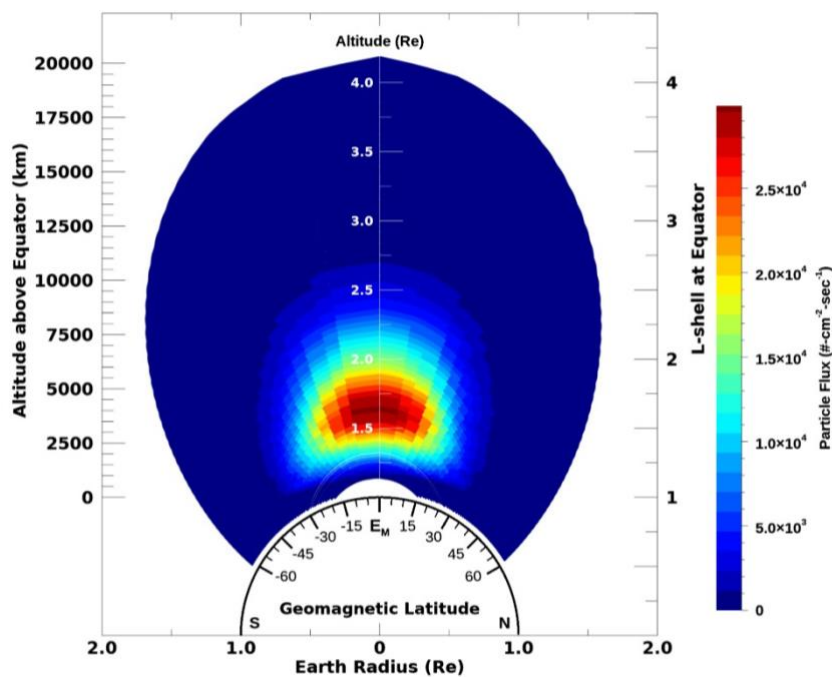
Figure 15. AE9AP9 generated proton flux for energy 10 to 2000 MeV depicting the recognized inner belt with intense radiation from L = 1.3 to 2.0

The inner radiation environment was studied using AE9AP9 simulations by

examining the particle distribution in three groups; high-energy protons, low-energy

protons and energetic ions known as the "warm" plasma. For the first group, Figure 15

depicts the AE9AP9 output for the population of protons with energy from 10 to 2000

MeV. This region of intense radiation spans L = 1.3 to 2.0 and reflects the classic

representation of the inner belt with a maximum omni directional flux of 2.5 x 10^5 cm^{-2}–

sec^{-1}. However, the objective behind incorporating AE9AP9 was to examine the

contribution from the lower-energy radiation population. Figure 16a depicts the AE9AP9

reported distribution of protons with energy from 0.1 to 10 MeV. This population of

protons spanning L = 2.5 to 4.25 is outside the inner radiation belt and in the region

a) Energy between 0.1 - 10 MeV   b) Energy between 1 - 100 keV
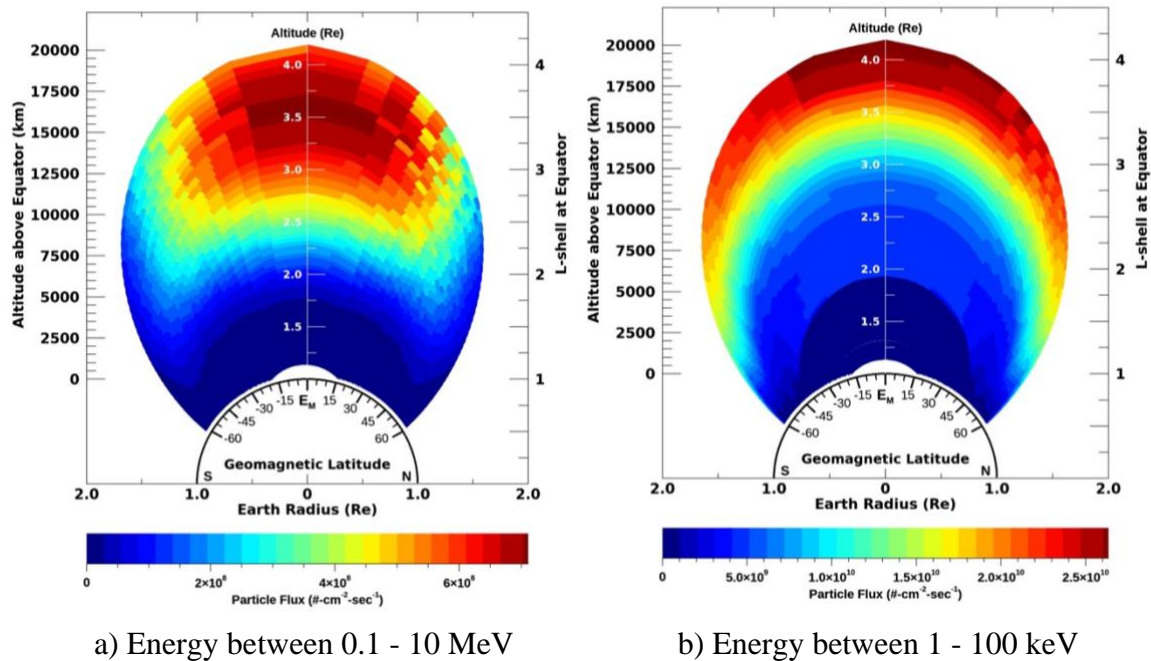
Figure 16. Panel (a) depicts AE9AP9 results for protons with energy
from 0.1 to 10 MeV while (b) represents total ion flux for energy
between 1 and 100 keV. These distributions of lower energy protons
and energetic ions have 3 orders-of-magnitude greater flux than the
high-energy protons in the inner radiation belt.

recognized as the "slot" for its absence of energetic electrons. With a maximum flux of

1.2 x 10^8 cm^{-2}–sec^{-1} at L = 3.3, these protons are 3 orders of magnitude greater in

population than found in the inner belt, albeit with considerably less energy. In addition,

AE9AP9 contains the "warm" plasma model, SPM, representing He$^+$, H$^+$, and O$^+$ ions

trapped in the magnetic field with energy from 1 to 100 keV. Figure 16b indicates the

combined flux distribution from AE9AP9 for the ions in this lower energy range. The

population of these ions become significant at L = 3.5 and increases with L until at L =

4.14, the top boundary of this study, the flux is 1 x 10^8 cm^{-2}–sec^{-1}, comparable to the

lower energy protons. The total flux of 1 to 100 keV ions is comprised of contributions

from He$^+$, H$^+$, and O$^+$ ions each having a similar distribution to the total and a maximum

individual flux of 7.5 x 10^6, 6.2 x 10^7 and 3.2 x 10^7 cm^{-2}–sec^{-1} respectively.
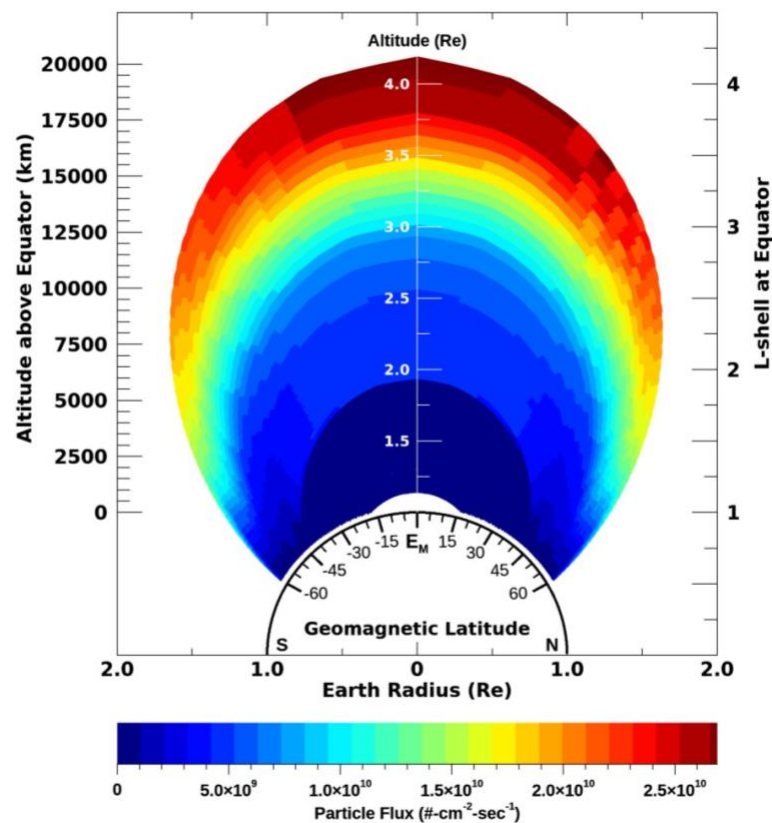
Figure 17. AE9AP9 aggregated flux for protons and ions from 1 keV to 2000 MeV. The maximum total flux, located at L = 3.8, is 1.9 x 10^8 cm^{-2}–sec^{-1} and dominated by protons below 10 MeV and ions below 100 keV.

The total flux, an aggregate of all proton and plasma populations provided by

AE9AP9 for the inner magnetosphere, is presented in Figure 17. With a peak flux of 1.9

x 10^8 cm^{-2}–sec^{-1} at L = 3.8, the total flux distribution is dominated by the population of protons below 10 MeV and ions below 100 keV and does not resemble the conventional inner radiation belt morphology previously described in Figure 15. Because these lower energy particles do not have the destructive effect on space systems as the high energy protons of the inner belt, they are not typically included in discussion about the radiation environment. However, for reason that will become apparent in the next chapter, these lower energy particles are the focus of this study. Chapter 3 presents the approach for comparing a plasma density to a flux of energetic particles in the radiation belts, a prerequisite for coupling the two models.

CHAPTER III

COUPLED MODEL APPROACH

Studying the interaction of the plasmasphere with the radiation belts required bridging two disciplines in space research. Within each discipline the models that evolved were optimized to support the unique needs of their respective communities. Due to various characteristics of the space environment and intended application, IPM and AE9AP8 use different units, coordinate systems and input parameters to best represent the observations and produce results in a form easily consumable by the users. Additionally, these models had to support the computational environments native to the two communities with different operating systems, software languages, libraries, interfaces and operating schemes. This chapter provides an overview of the approach employed to link the two models, the selection of input parameters for the four cases in the study and the conversion of flux to density. The extensive software development effort supporting this study consisting of modifications to IPM, the subroutines created to incorporate AE9AP9, IDL display routines along with a description of the input and output file formats, testing, and operating sequence is provided in Appendix D.

Coupling IPM and AE9AP9

From preliminary investigations with an independent population of charged particles in a 1-D ionosphere model, see Appendix E, the dominant effect anticipated for this plasmasphere-radiation belt study is a change in propagation and distribution of the cold plasma due to the presence of the energetic particles. Analogous to the 1-D example, the approach for this study is to express the radiation belt as a static distribution of

charged particles in the same magnetic flux tube as the cold plasma from the

plasmasphere. By adding a static population of charged ions into the IPM background

density, the numerical solution for the transport of plasma along a magnetic field line

should reflect the influence of the radiation particles on the plasmasphere. Evaluating the

significance of the radiation belt influence on the plasmasphere will be accomplished by

comparing IPM simulations with and without the radiation particles during the transport

of the cold plasma. To this end, the coupling of the two models is simplified by

expressing the radiation flux as an independent species density while solving the

transport equations for the distribution of cold plasma in the same flux tube.
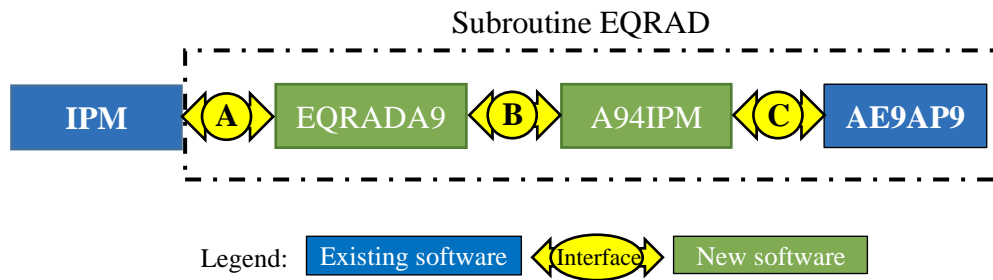
Figure 18. Block diagram of the software modules and interfaces in
EQRAD providing IPM a density derived from the AE9AP9 radiation
flux.

As depicted in Figure 18, the radiation particles provided by AE9AP9 were

incorporated in the global Ionosphere-Plasmasphere Model (IPM) using a new subroutine

called EQRAD. EQRAD was created to calculate the total density of charged particles

from the AE9AP9 provided flux for every IPM flux tube sample location. The subroutine

uses the Fortran API supplied with AE9AP9 release 1.30.001 to retrieve the energy

dependent particle flux from the model for a radiation species at a specific location (Air

Force Research Laboratory, 2016). A parameter in the setup file enables the user to select a radiation species or combination of species generated by AE9AP9 for inclusion in the total density calculation. Although the approach for coupling the two models was intended to provide seamless integration of AE9AP9 into IPM, for this study, IPM and the EQRAD subroutine were run separately. Identified in Figure 18 as interface "A", throughout this study the connection between these two modules was accomplished with the exchange of two files A1 and A2. File A1, generated by IPM, contains the details specific to every sample point along a flux tube and A2 ingested by IPM, provides the total radiation density derived from AE9AP9 for every sample point in A1. The use of the exchange files allowed better insight into the evolution of the plasmasphere in response to the distribution of injected energetic particles. The details regarding the exchange file formats, setup parameters and development of the EQRAD subroutine is provided in Appendix D

Selecting Parameters for the 4 Study Cases

In Chapter 2, representative samples of the naturally occurring ionosphere-plasmasphere density and trapped energetic particle fluxes were generated using the Ionosphere-Plasmasphere Model (IPM) and radiation belt model AE9/AP9/SPM (AE9AP9). In order to explore the extent of possible interaction between the two plasma populations, it was necessary to select conditions where the IPM and AE9AP9 model would produce output spanning typical variations for the environment. This range of plasma variations can be represented by four cases. For IPM, these four cases can be identified by dates corresponding to northern hemisphere summer and winter using solar and geomagnetic parameters corresponding to periods of minimum and maximum

activity. Since energetic particle flux from AE9AP9 is produced for a specific date and

IPM densities vary by supplied solar and geomagnetic parameters, 20-years of 10.7 cm

solar radio flux data, was reviewed to select time periods representing the study

conditions (NOAA, 2019).

From the 10.7 cm radio observations two dates were selected in 2001

corresponding to solar maximum summer and winter and two dates in 2008 for solar

Case Study	1	2	3	4
Year	2001	2001	2008	2008
Solar Conditions	Maximum	Maximum	Minimum	Minimum
Solar 10.7 cm flux	200	200	70	70
Average F10.7	200	200	70	70
Day of Year	180	360	180	360
Northern Hemisphere	Summer	Winter	Summer	Winter
Ap	4.0			
Longitude	270 degrees			
Altitude	600 km – 20,000 km, (L=1.1 – 4.1)			
Local Time	0000, 0600, 1200, 1800 hours			

Table 1. IPM and AE9AP9 parameters selected to represent the four
study cases.

minimum summer and winter. To simplify interpretation of the results, the solar flux

values were rounded to 200 for solar maximum and 70 for solar minimum. Likewise, the

same value was used for the daily and average solar flux. Avoiding complications due to

the compression of magnetic field lines during high geomagnetic activity, the value for

the planetary geomagnetic index, Ap, was fixed at 4.0 for all cases. The dates and

corresponding parameters used in the four cases of this study are summarized in Table 1

and depicted in Figure 19 on top of 20-years of measured solar 10.7 cm flux data

indicating the naturally occurring variability in the environment.
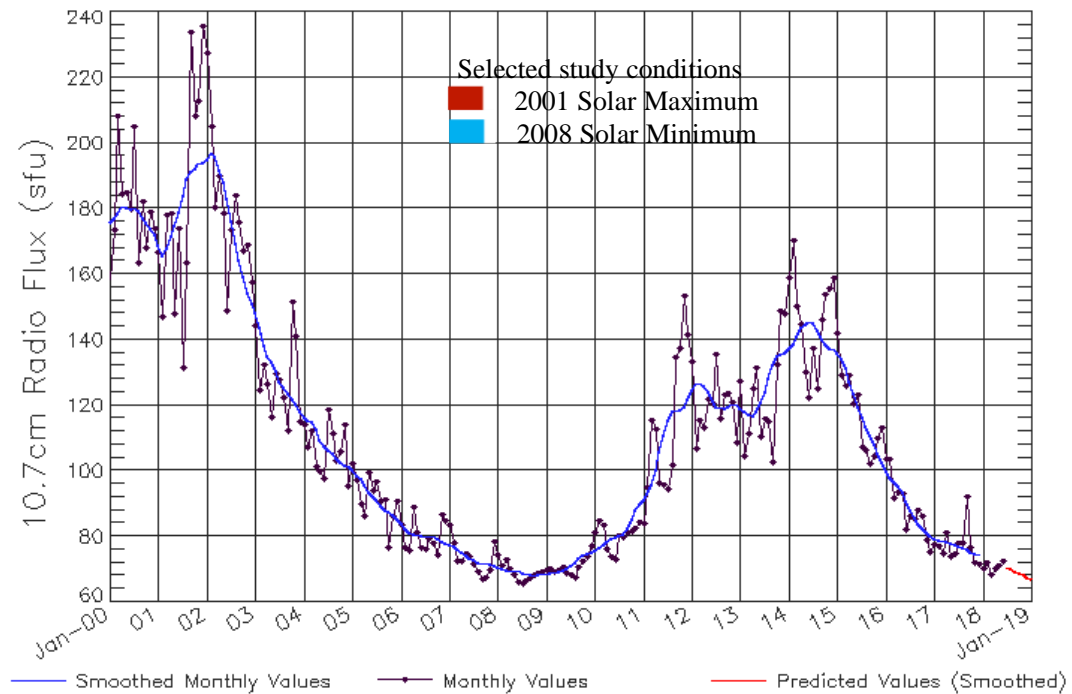
Figure 19. Solar 10.7 cm radio flux data from the Space Weather
Prediction Center depicting the dates and values selected for this study
(NOAA, 2019).

Restricting Ap to 4.0 may appear to be a concern since AE9AP9 is an empirical

model and may have incorporated data during an active period when the actual Ap was

closer to 22. However as noted in Chapter 2, the sparse data sets supporting the low

energy protons and warm plasma were insufficient to reflect the expected variability from

the solar and geomagnetic activity. Although a limitation of the current AE9AP9 model,

it will not impact this study.

Technique for Representing Flux as a Density

As noted earlier, the coupled model simulations will be accomplished by inserting

radiation belt particles into IPM as an independent charged species. This requires the

representation of the AE9AP9 provided fluxes ($\#$-cm^{-2}-sec^{-1}-MeV^{-1}) as a number density

of charged particles (#-cm^{-3}). In its simplest form, knowing the type and energy of the particle, density ρ can be obtained by,

$$\rho = \frac{j}{v(E,m)}, \tag{3.1}$$

where j is the flux of the particle expressed as (#-cm^{-2}-sec^{-1}) and velocity v is given by,

$$v = c\sqrt{1 - \left(\frac{1}{\left(\frac{E}{mc^2}+1\right)}\right)^2}, \tag{3.2}$$

the mass m of the particle and energy E. It is worth noting as significant to this study and the conversion of a single species flux to density, the energy and density have an inverse relationship. The greater the particle energy, the greater its velocity, and the less time it takes to transition a unit of volume. The time it takes for a particle to transition the length of a unit of volume is its contribution to density and represents the inverse of particle velocity. As illustrated in Figure 20, a flux of fast particles results in a lower density than the same flux of slower particles. The particle density contribution (sec/cm) is the energy dependent scale factor for converting flux (#-cm^{-2}-sec^{-1}) into number density (#-cm^{-3}).

Equally important is the relationship between the mass of a particle and its contribution to density as expressed in (3.1). The radiation belts contain particles with distribution varying in energy and species as a function of time and location. AE9AP9 provides the capability to specify the flux of each species in time and location, integrated over an energy range. The range of energies represented in AE9AP9 differs by species and is reported to contain energetic electrons from 1 keV to 10 MeV, protons from 0.1 MeV to 2000 MeV and warm ions, H$^+$, O$^+$ and He$^+$ from 1 keV to 0.1 MeV (Ginet, et al., 2013). The density for a unit of flux was calculated for the species in AE9AP9 across the reported range in energy. Figure 21 indicates the relative contribution to density for each

species. Due to the energy of some particles, the relativistic formulation was included in

the calculations resulting in the non-linear scale factors at higher energy. Not unexpected

but interesting, energetic O^+ ions provide the greatest contribution to density per unit of

flux.

An additional complication in the representation of radiation number density from

the AE9AP9 model output is that flux is expressed integrated over an energy interval. As

such, an accurate representation of velocity for the integrated flux necessitates knowing

the energy distribution of the particles over the same interval, unfortunately not available
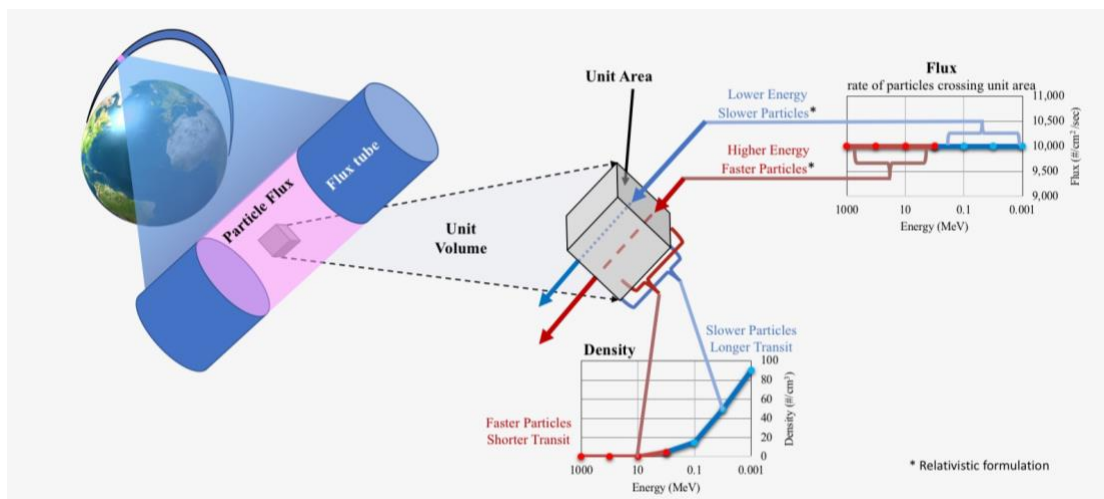
Figure 20. Illustration of the velocity relationship for the flux to density
conversion where a population of particles with the same mass have a
distribution in energy. Particles with greater energy will have a greater
velocity but a lower contribution to the number density.

from AE9AP9. This error in calculated velocity can be minimized by using small energy

bands, limited to the resolution of the energy grid internal to AE9AP9. The energy grid

internal to AE9AP9 was obtained and applied in EQRAD to select the intervals for the

integrated flux. Since the internal grid was developed for AE9AP9 based on the energy

distribution of particles in the data, these intervals were used in EQRAD to minimizes the error in velocity (O'Brien, 2017). The AE9AP9 internal energy grid for all species is provided in Appendix D and used to calculate the values in Figure 21.

Within EQRAD, the number density for a species at any location is determined by summing the results obtained from the repeated conversion of AE9AP9 flux across all energy intervals. During model initialization, the user can select to generate a density from a single species or a combination of species (e.g. protons, H^+, He^+, O^+ or electrons). The total density for a location is determined by first computing the number density
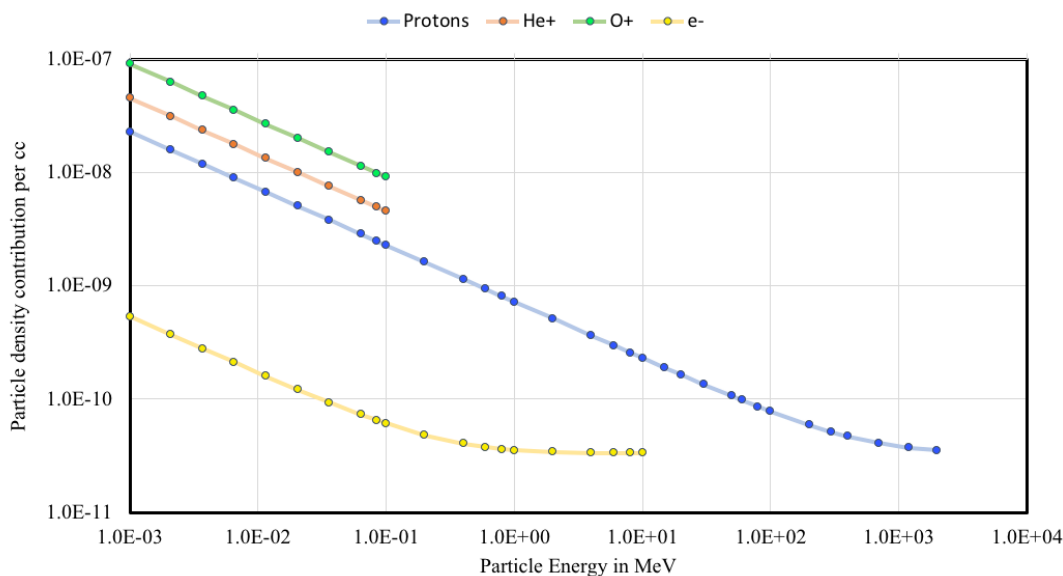
Figure 21. Density derived from a unit of flux ($1/cm^2$/sec) for each AE9AP9 species as a function of energy. The AE9AP9 internal grid is used for the energy intervals. The calculation includes the relativistic formulation.

derived for each species then aggregating them. The density along a flux tube is obtained by running IPM to generate the sample locations then running EQRAD, calling AE9AP9 and converting the flux to density for every location provided by IPM. The flexibility to

select one or a number of species for inclusion in the total density enabled the

examination of the spatial distribution and quantity for an individual contribution.

Density Derived from AE9AP9 Simulations

In Chapter 2, AE9AP9 was used to generate distributions of proton and ion flux

below L = 4.14 for three energy bands, 2000-10 MeV, 10 to 0.1 MeV, and 100 to 1 keV.

The fluxes provided from those simulations were converted to density using the approach

previously described. Figure 22a depicts the number density derived for the inner

radiation belt flux of protons with energy from 10 to 2000 MeV, previously described in

Figure 15. These super energetic protons with a peak flux greater than 10^5 cm^{-2}- sec^{-1}

translate into a pitifully insignificant density of 4 x 10^{-4} particles per cm^3. Next, the less

a) Protons with energy 10-2000 MeV   b) Protons with energy 0.1-10 MeV
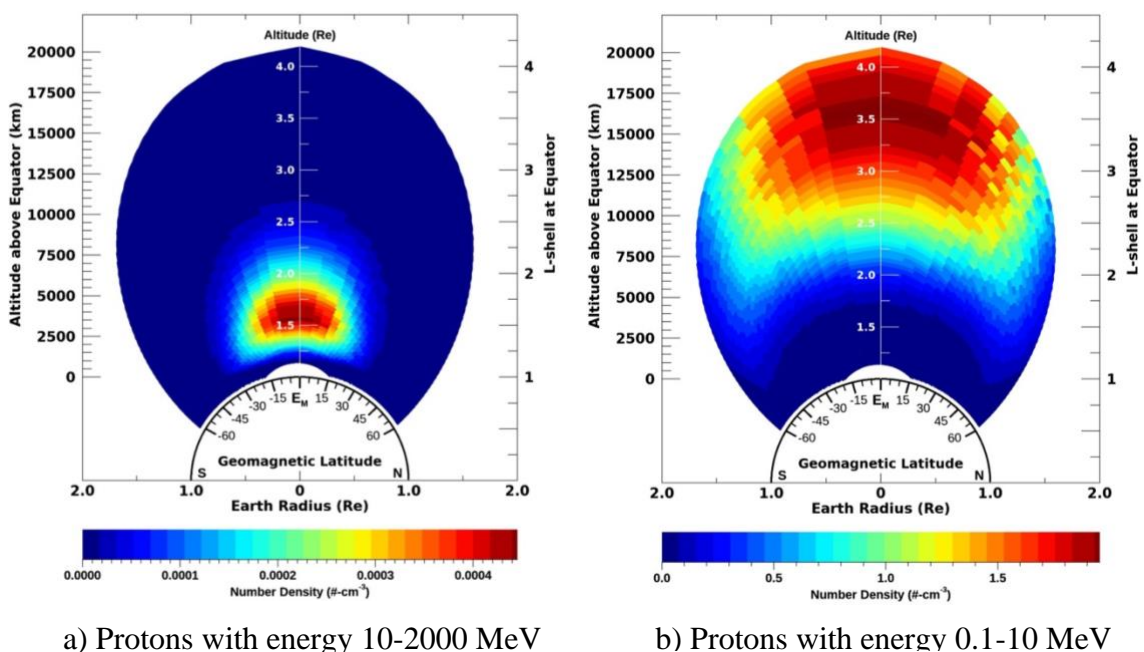
Figure 22. Number density derived from AE9AP9 generated flux.
Panel (a) depicts protons with energy from 10-2000 MeV
corresponding to a density of ~ 10^{-4} cm^{-3}. Panel (b) depicts protons
with energy from 0.1 to 10 MeV having a peak density at 1.9 cm^{-3}.
Note, the two images use different color scales.

energetic proton flux distribution displayed in Figure 16a having energy from 0.1 to 10

MeV was translated to density and presented in Figure 22b. Even this population of

protons with a peak flux of order 10^8 cm^{-2}- sec^{-1}, 3 orders of magnitude greater than the

high-energy proton flux, corresponds to a density of less than 2 cm^{-3}.

However, it is the lowest energy population of trapped particles, the "warm"

plasma previously absent in radiation models, that provides the greatest contribution to

the radiation density. Separating the 1 to 100 keV total plasma radiation shown in Figure

Particle Type	Energy Range (MeV)	Peak Flux (#-cm^{-2}-sec^{-1})	Peak Density (#-cm^{-3})	Shell (L)	Appx. Altitude (km at equator)
Proton	10 - 2000	2.5 x 10^5	0.00044	1.6	3,500
Proton	0.1 - 10	1.2 x 10^8	1.9	3.6	16,000
He$^+$ ion	0.001 – 0.1	7.5 x 10^6	1.9	3.9	18,500
H$^+$ ion	0.001 – 0.1	6.2 x 10^7	4.5	4.1	20,000
O$^+$ ion	0.001 – 0.1	3.2 x 10^7	16.2	3.8	17,500
Total	0.001 - 2000	1.9 x 10^8	23.4	3.9	18,500

Table 2. AE9AP9 energy range and peak flux for trapped particles by species and the corresponding density.

16b by species, the flux for He$^+$, H$^+$, and O$^+$ was converted into density with the resulting

ion distributions provided in Figure 23. Comparing the H$^+$ ion peak of 4.5 cm^{-3} in Figure

23b to the maximum for protons of 1.9 cm^{-3} in Figure 22b, the importance of the energy

distribution on density becomes immediately apparent. The 0.1 to 10 MeV protons have

nearly twice the flux of the 1 to 100 keV H$^+$ ions, however the lower energy population

Derive Density for Warm Trapped Ions
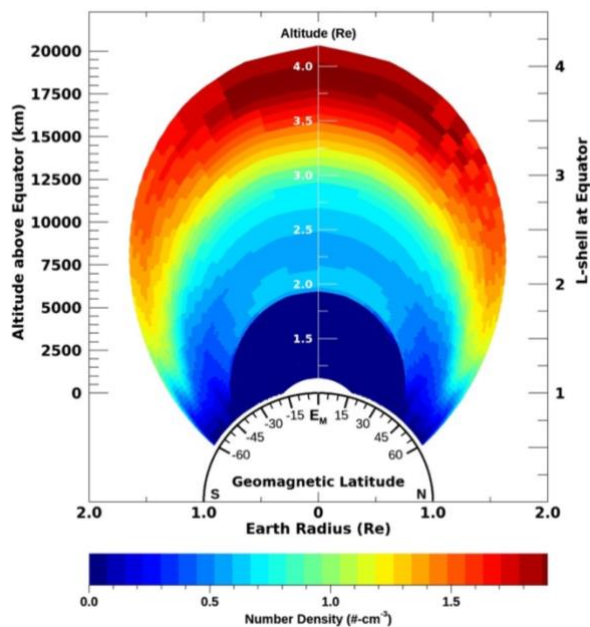
a) He⁺ Density
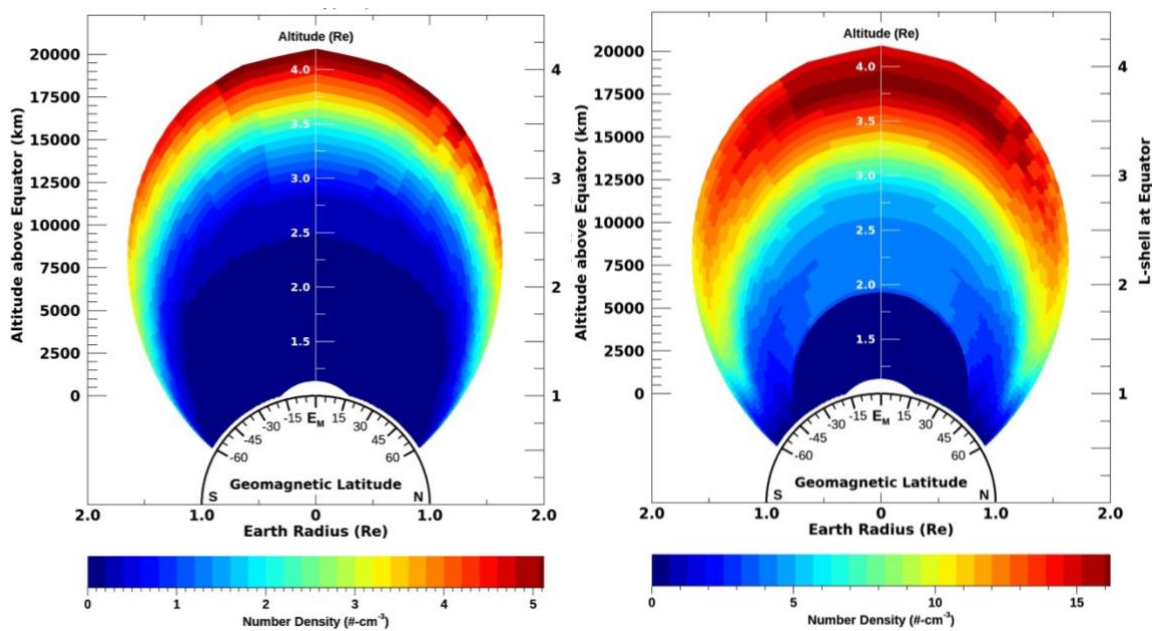
b) H⁺ Density

c) O⁺ Density

Figure 23. AE9AP9 flux derived density distribution for He⁺ H⁺ and O⁺ ions having energy from 1 to 100 keV. The maximum density for He⁺, H⁺ and O⁺ is 1.9, 4.5 and 16.2 cm⁻³ respectively. Note the color scales are different for each species.

represents more than twice the density. In Figure 23a, the dependence on the mass of the

particle is easily observed. The peak He$^+$ flux is 16 times less than protons with energy

from 0.1 to 10 MeV, yet the lower energy ions with 4 times the mass results in an

equivalent density of 1.9 cm^{-3}. Last, the O$^+$ ion having both lower energy and the largest

mass accounts for two-thirds of the total density from the radiation. As shown in Figure
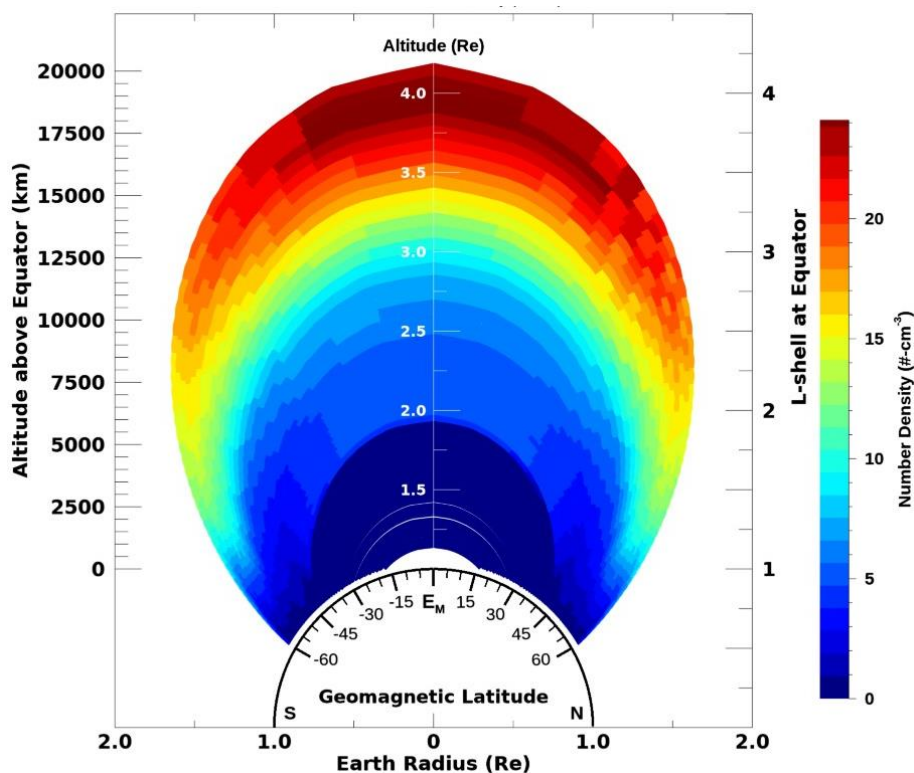
Figure 24. AE9AP9 derived total density for all energetic protons and
ions with energy spanning 1 keV to 2000 MeV. The maximum density
is 23.4 cm^{-3} and located L = 3.9.

23c, with a maximum of 16.2 cm^{-3} at L = 3.8, O$^+$ has the greatest contribution to the total

energetic particle density. Table 2 provides a comparison of the maximum value and

location of the flux for each AE9AP9 particle type along with a representative density.

The larger mass of the trapped O$^+$ particles results in a greatest contribution to the overall

hot particle density. Aggregating the proton and plasma density derived from the AE9AP9 flux for the three energy ranges, a total density distribution was created for the inner magnetosphere, Figure 24. Including radiation belt particles with energy spanning 1 keV to 2000 MeV, the noted maximum density is 23.4 cm^{-3} and located L = 3.9. As indicated in the table above, it is the lower-energy "warm" plasma, with the predominate contribution from O$^+$, that dominates the total density distribution. Employing this representation of radiation flux as a density of charged particles, Chapter 4 will compare the radiation environment to the plasmaspheric density and explore any possible dynamics between the two.

CHAPTER IV

RESULTS

The approach for investigating the effects of the energetic trapped particles in the radiation belts on the relatively cold ionosphere-plasmasphere is based on generating independent samples of each environment, modeling the interaction and then looking for perturbations in the background plasma density due to the hot particles. Within this chapter a simple simulation is used to identify the bounding conditions and select the corresponding plasmasphere and radiation belt environment for investigation. Using the representative density for the two environments, the coupled model is run and the results are compared to the original background to evaluate the effect.

The Bounding Conditions for Plasmasphere and Radiation Belt Interaction

A simple ionospheric simulation was used to survey the environmental conditions expected to yield the smallest and greatest effect of the radiation density interaction with the plasmasphere. In Appendix E, the simulation of an artificial layer of protons inserted into a one-dimensional background ionosphere resulted in the redistribution of ionospheric plasma about the new layer. Although the simulation was highly idealized, it is analogous to the situation in the outer plasmasphere where the H^+ ion dominates and the density distribution is constrained along a flux tube. The results of the one-dimension simulation demonstrated that the perturbation in the O^+ and electron density is proportional to the ratio of the added proton density and the background O^+ density. Applying these results to the study of interest, the greatest effect of the radiation belt is

expected when the radiation particle density is comparable to the background plasma density.
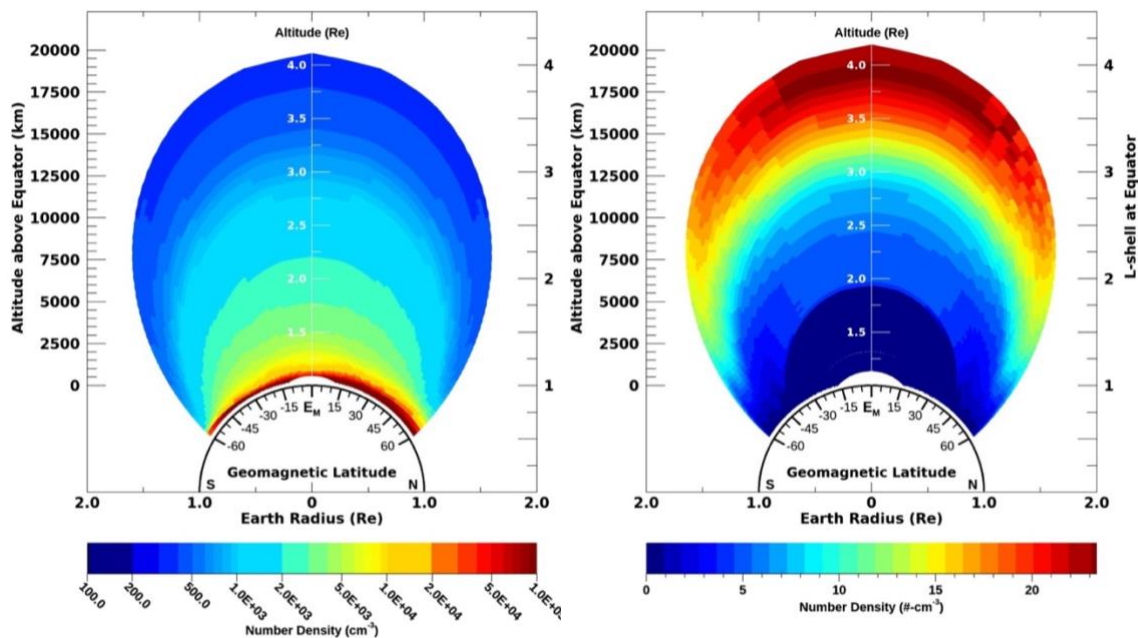
a) IPM Total Ion Density   b) AE9AP9 Total Particle Density

Figure 25. Comparison of a) total ion density from IPM and b) total warm particle density from AE9AP9 during solar minimum conditions for northern hemisphere summer. Note the different color scales.

A comparison of the ionosphere-plasmasphere environment presented in Chapter 2 and the hot particles density derived from the radiation environment in Chapter 3 quickly reveals that the interaction of these two populations is mostly negligible. This quick assessment is possible since the background plasma density is predominately several orders of magnitude greater than the maximum radiation particle density, Figure 25 a & b. As indicated in Chapter 3, the maximum density of hot particles is of order 20 cm^{-3} and is located at the equator along L = 3.9 (18,500 km). Due to limitations in the

AE9AP9 model discussed previously, the maximum radiation density for this study does not change with local time and season and has little variation with the solar cycle.

In contrast to the background ionosphere-plasmasphere described in Chapter 2, the density in the ionosphere has a peak of greater than 10^6 cm^{-3} and decreases three to four orders of magnitude in the upper plasmasphere. Although changes in the plasma density due to local time, season, solar and geomagnetic activity span an order of
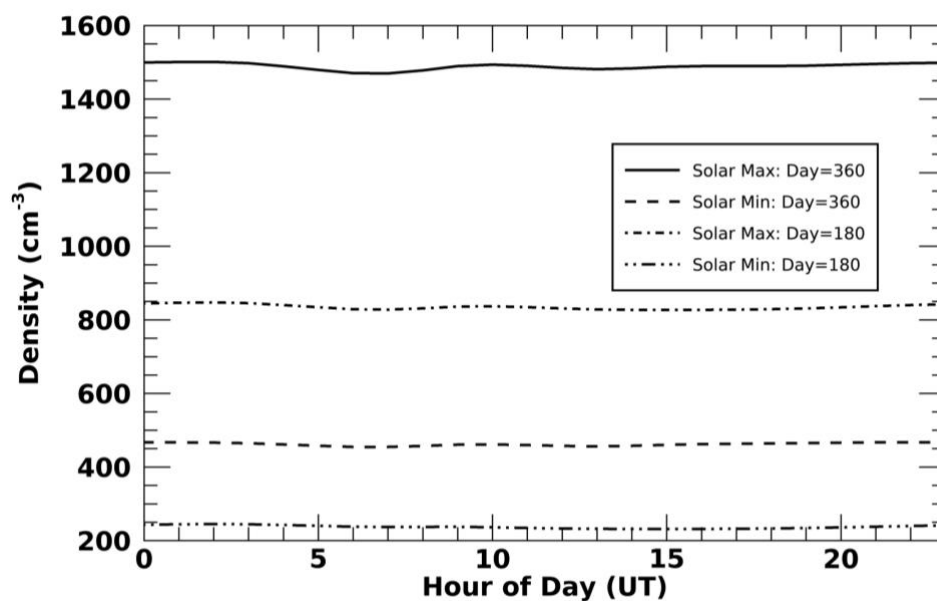
Figure 26. Hourly variations in total ion density at 18,500 km above the Equator on day 360 and 180 for solar minimum and maximum conditions.

magnitude or two in the region below 1000 km, at the equator along L = 3.9 (18,500 km) these variations are at most a factor of 7. As seen in Chapter 2, the greatest total ion density in this outer region is 1500 cm^{-3} occurring in 2001 on day 360 while the lowest density is around 250 cm^{-3} in 2008 on day 180. These two bounding conditions

Expected Effect (at equator, L = 3.9)	Year	Day	Season (Northern Hemisphere)	Solar Conditions
Greatest	2008	180	Summer	Minimum
Smallest	2001	360	Winter	Maximum

Table 3. Environmental conditions providing the greatest and smallest effect of the radiation particles interacting with the plasmasphere.

correspond to northern hemisphere winter, day 360, during solar maximum and northern hemisphere summer, day 180, during solar minimum, Figure 26.

It is only within the region of maximum radiation density, L = 3.9 around the equator (18,500 km), where an appreciable resemblance in density to the cold plasma can occur. Within this region during solar minimum the hot particle density in the outer radiation belt is approaching 10% of the background plasmasphere while it is less than
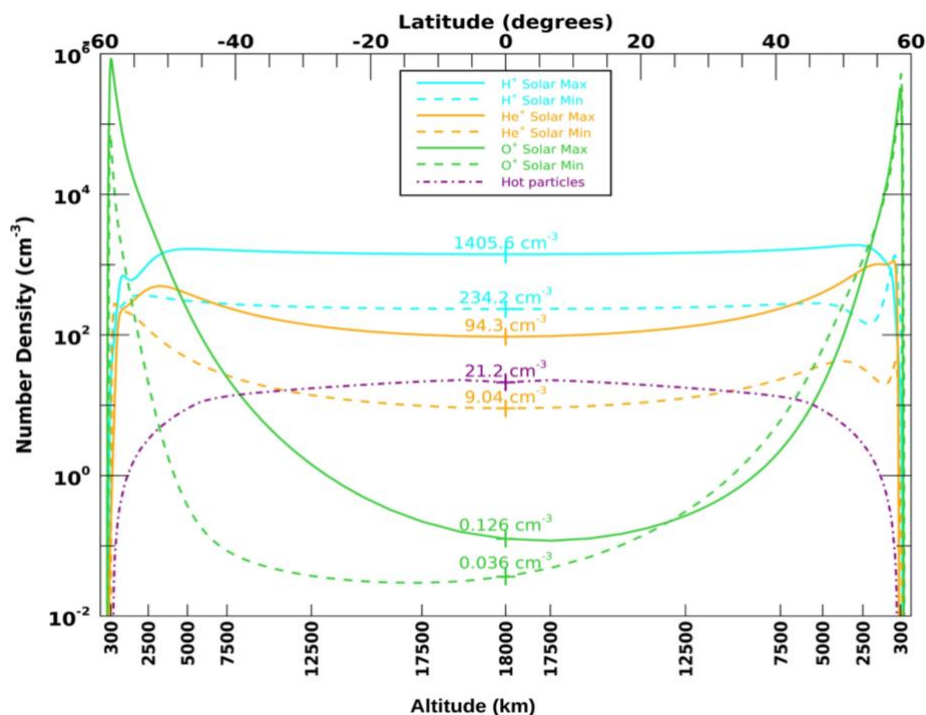
Figure 27. Relative abundance of the cold plasma ion species and radiation particles along the L = 3.9 flux tube at UT=00 during solar minimum, 2008 Day 180, and maximum conditions, 2001 Day 360.

2% during solar maximum. As such, the greatest and smallest effect from the interaction

with the radiation particles is expected during solar minimum and solar maximum,

respectively, at the equator along L = 3.9. These conditions become the bounds for this

study with northern hemisphere summer solar minimum in 2008 on day 180 and northern

hemisphere winter solar maximum occurring in 2001 on day 360, see Table 3. As

described in Chapter 2, at 18,500 km near the equator, the H^+ ion dominates the plasma

density with a small fraction of He^+ and O^+, Figure 27. As such, a variation in the cold

plasma in the region of the hot radiation particles is expect to be most noticeable in H^+

density.
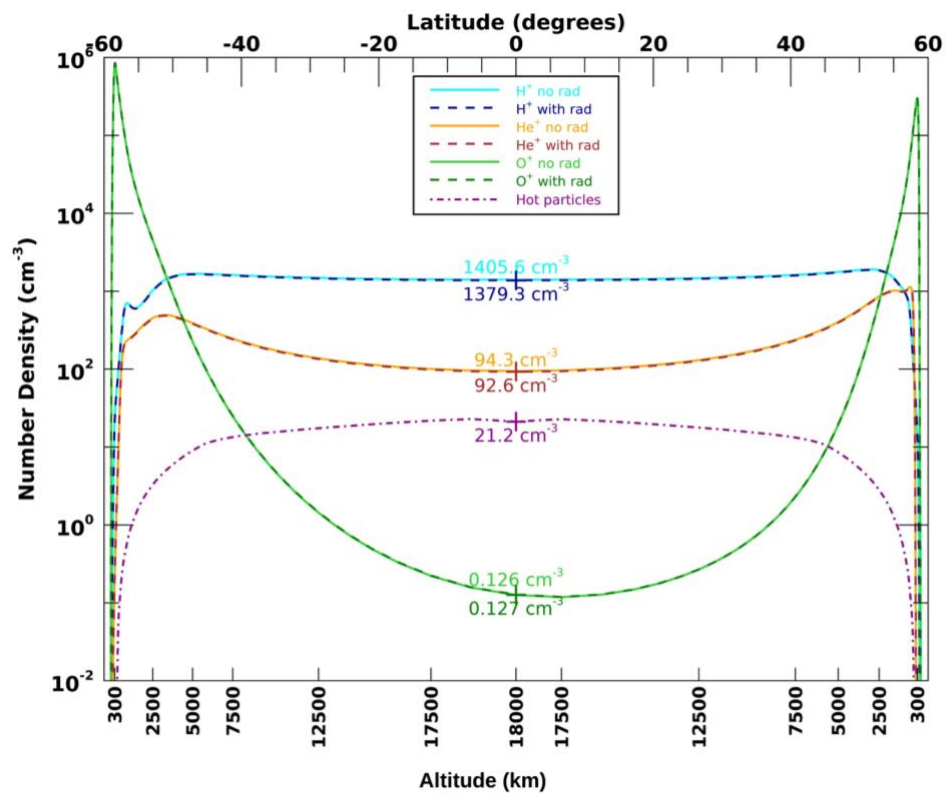
Figure 28. Solar maximum background cold ion density along flux tube
L = 3.9 and IPM response with the addition of warm particles from the
radiation belt are nearly identical.

Simulation of Plasmaspheric Response to the Radiation Belt Particles

The IPM simulations in Chapter 2 were repeated and after the model had warmed

up and stabilized, the hot particle distributions described in Chapter 3 were inserted as an

independent species similar to the simulation in Appendix E. The simulation was allowed

to continue after the injection of the hot particles until the plasma density stabilized

again. IPM simulations with the warm particles were produced for solar maximum and

solar minimum, the two bounding conditions discussed previously. The results along flux
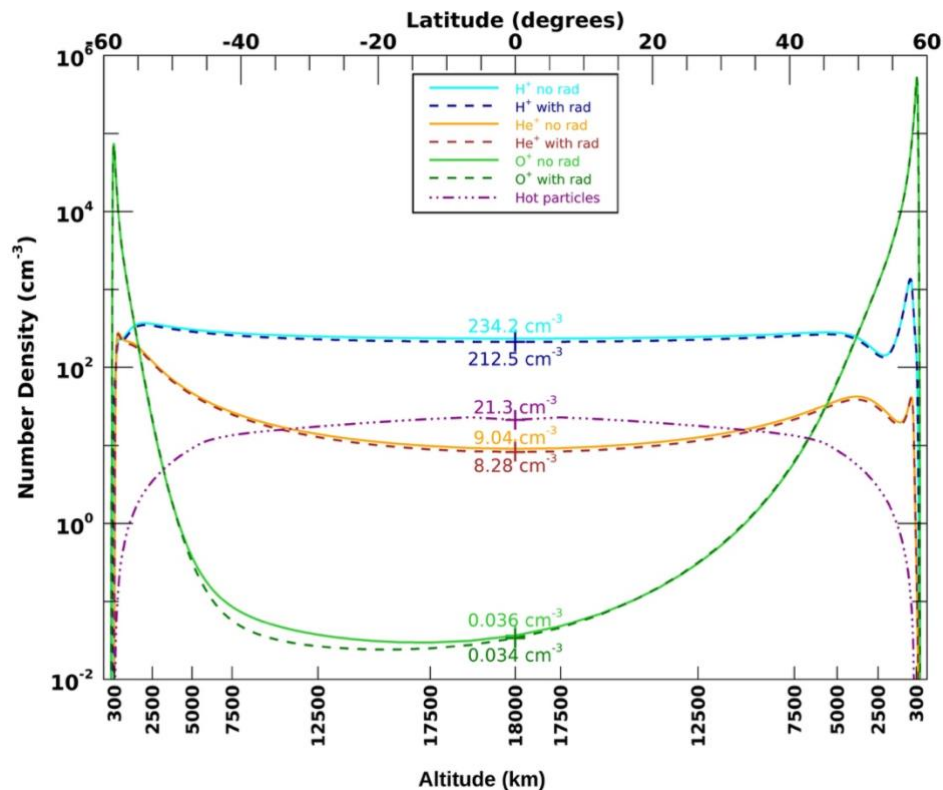
Figure 29. Solar minimum background cold ion density along flux tube
L = 3.9 and IPM response with the addition of warm particles from the
radiation belt. A modest decrease in the background ion density is
observed in the region of the warm particles.

tube L = 3.9 for the bounding conditions with the warm particles were compared to the original background plasmaspheric density, Figures 28 and 29.

As expected, during northern hemisphere winter solar maximum conditions the addition of hot particles resulted in a minor decrease at 18,500 km near the equator; less than 2% reduction in the background ion density. During NH summer solar minimum, the background ion density is substantially less. Under these conditions the warm particle density at 18,500 km near the equator is greater than the He^+ ion density by a factor of 2. The IPM results under these conditions produced a decrease in the total ion density approaching 10%. Focusing only on the equatorial region with the greatest deviation, the
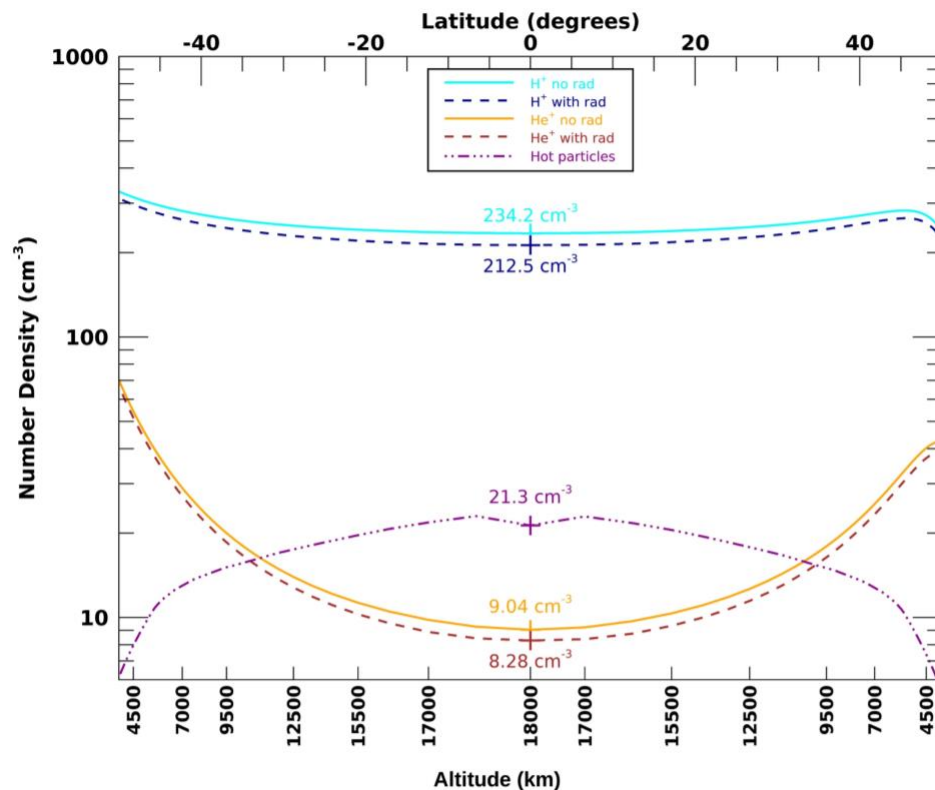
Figure 30. High-altitude portion of the L = 3.9 flux tube indicating variation in the cold plasma density, H^+ and He^+, due to the presence of warm particles from the radiation belt.

radiation particles reduce the background H^+ ion density by 9% and the He^+ ion density by 8% , Figure 30.

As demonstrated above, the low density of the energetic radiation belt particles results in a small perturbation to the cold plasma in a fully populated plasmasphere. However, under particular circumstances the presence of the hot particles can be more significant. One example of such unique conditions occurs when the plasma density in the outer flux tubes is depleted after a geomagnetic storm.

Storm Depleted Plasmasphere and Recovery

The presence of a solar and geomagnetic storm increases the radiation belt ion population and decreases the outer plasmasphere density. Such events cause significant changes in the relative populations of energetic and cold particles, suggesting the outer radiation belt may at times have a greater influence on the plasmaspheric density. Although the approach employed here for coupling the plasmasphere and radiation belt is too simplistic to fully examine the interaction of the two systems, the coupled IPM model can offer some insight into the refilling of depleted flux tubes during events with enhanced trapped particle flux.

Frequently, the impinging solar wind particles and geomagnetic response drive large variations in the radiation belts and plasmasphere, not exhibited in the very quiet behavior modeled in Chapters 2 and 3. As described in Appendix C, during high geomagnetic activity, strong electric fields accelerate H^+, He^+ and O^+ ions out of the ionosphere and inject them into the outer radiaiton belts. These moderate solar and geomagnetic storms often compress the plasmapause, typically located at $L = 5$, to below $L = 3.5$ significantly decreasing the plasmaspheric density in the outer region. Such

events are relatively frequent, taking place approximately 5 to 40 times per year with more than 20 occurrences in most years. Satellite observations of storm conditions indicate at L = 4.12, the plasmaspheric density decreases an order of magnitude with refilling rates on the order of 67 to 166 #/cm^3/day, taking days or weeks to return to pre-storm conditions (Dent, Mann, Goldstein, Menk, & Ozeke, 2006). Given the frequency for moderate geomagnetic storms to reduce plasmaspheric density and the extended duration for refilling, the outer flux tubes are typically only partially filled.

a) Full flux tubes   b) Depleted outer flux tubes
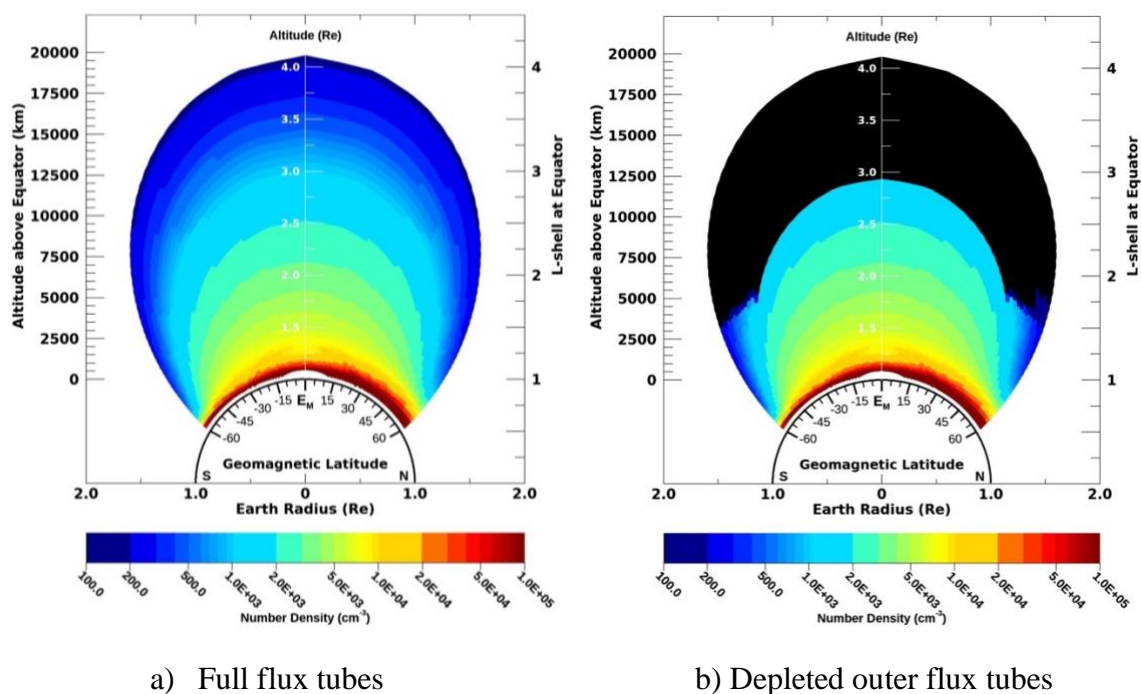
Figure 31. Depiction of IPM total density during full flux tubes (a) and then immediately after depleting the ions an order of magnitude above 12,500 km (b).

AE9AP9 does not include the radiation belt response to geomagnetic storms. However, in situ observations from recent satellite missions provide an indication of the enhancement of protons and oxygen ions during small-scaled injections in the innner magnetosphere. As explained in more detial in Appendix C, the Van Allen Probe data

indicates moderate geomagentic storms efficiently enhance the proton flux by a factor of

3 to 5 and the oxygen ion flux by a factor of 2 to 4 in the radiaiton belts around L=6 and

possibly extending as low as L = 4 (Keika, et al., 2016). The combination of efficient

acceleration of O^+ into the outer radiation belts and the depletion of cold plasma in the

outer plasmasphere during geomagnetic storms, indicates energetic O^+ ions frequently

become the dominant species in this region (Horwitz, et al. 1984).
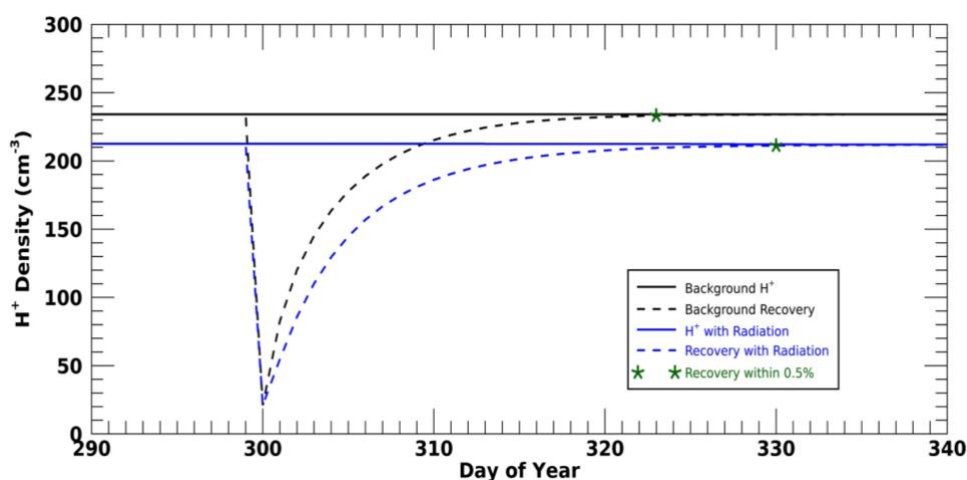
Figure 32. Refilling time for a flux tube at L = 3.9 during solar
minimum conditions in the presence of warm particles takes 30%
longer to refill.

The couple IPM model provides a simplistic simulation of the interaction of the

outer plasmasphere and radiation belt during a geomagnetic storm. As described in

Appendix D, IPM was modified with an option to deplete the cold plasma density in the

outer flux tubes simulating a geomagnetic storm event. When the setup parameters for a

depletion event are included, IPM momentarily reduces the background density in the

flux tubes above L = 3 (12,500 km) to a specified background without changing the

radiation particles if any. Within any one of these depleted outer flux tubes, the reduced

density is constant from the peak to 7000 km altitude where it smoothly transitions to the undisturbed value, see Figure 31b. The density in this region is only momentarily reduced, allowing upward diffusion of cold plasma along the flux tubes to slowly refill the plasmasphere as the simulation continues.

To explore the refilling of depleted flux tubes in the presence of the hot particles from the radiation belt, IPM was configured for a single flux tube at L = 3.9 using solar minimum conditions starting on 2008, day 180. After stabilization of the background plasma density, the hot particles were injected on day 250 and the simulation continued another 50 days to reach steady state again. On day 300 the outer flux tube density was decreased by an order of magnitude leaving a total density of approximately 24 cm^{-3}. The simulation continued after the depletion allowing the cold plasma to refill the flux tube and stabilize again. The same simulation was repeated without the additional hot particles providing the nominal background plasmasphere, depleting the outer flux tubes on day 300 and subsequent refilling. A time series plot of the depletion and recovery of H^+ density at UT=00 for the two simulations is provided in Figure 32. Examining the flux tube along L = 3.9, when radiation particles are not present, the cold H^+ density returns to within 0.5% of the pre-depleted values in 23 days. However, in the presence of the hot particles equating to 8% of the total plasma density, the recovery of H^+ takes 30 days, about 30% longer.

A complete depletion and recovery simulation for a geomagnetic storm was attempted with IPM using 4 times the AE9AP9 radiation density to approximate the trapped particle enhancements of factors of 4 and 5 in O^+ and H^+ observed by the Van Allen Probes. With the application of a factor of 4, the hot particle density over the

equator along flux tube L = 3.9 becomes ~94 #/cm^3. Under these enhanced conditions the trapped particle population represents little more than 6% of the background plasmasphere during solar maximum but nearly 40% of the cold plasma density during solar minimum conditions when the flux tubes are completely full. However, during a geomagnetic storm when the cold plasma in the outer flux tubes is depleted by an order of magnitude, the enhanced radiation particles are more than 60% of the background plasma for solar maximum and nearly 4 times the background density during solar minimum. For reasons described at the end of Appendix D in Coupled Model Limitations, an IPM simulation injecting hot particle with a density approaching 30% of the background plasmasphere unsuccessful due to numerical instabilities. Based on the simulation presented in figure 32, where electrostatic repulsion of hot radiation particles and the cold background plasma caused a 30% increase in refilling time, a storm enhanced radiation belt trapping additional H$^+$ and O$^+$ particles and increasing the total radiation density a factor of 4 is expected to substantially increase the refilling time during solar minimum. Likewise, a factor of 4 enhancement in the trapped particle density during a storm under solar maximum conditions would result in the total radiation particles being 6% of the cold plasma background. Although smaller, under these conditions the refilling time of the outer plasmasphere during solar maximum would be 20% longer.

CHAPTER V

CONCLUSION

Since the discovery of the radiation belts as early as 1958, the continued

exploration of the composition of high energy electrons, protons and ions trapped along

the Earth's magnetic field lines has been studied largely independent of the dynamical

processes in the Plasmasphere. Likewise, research involving the relatively cold plasma

produced at low altitudes in the ionosphere and transported along field lines filling the

plasmasphere has not taken into the possibility of an effect due to the radiation belts. As

research on the magnetospheric response to geomagnetic storms advanced, several

complex mechanisms for terrestrial ions populating the outer radiation belt and the

relationship to the plasmapause were formed. However, the high energy of outer belt

particles and low density of the co-existing cold plasma suggested any interaction

between the two species was negligible. Recent radiation belt probes with greater

dynamic range and sensitivity to lower energy particles, including warm ions of

terrestrial origin, have illuminated the existence of a robust populations of warm trapped

ions. Although still believed to be under represented, some new radiation belt models,

such as the AE9AP9 include the warm population of trapped particles making it possible

to explore the potential interaction with the plasmasphere.

This study of the interaction of the plasmasphere and radiation belts used the

Ionosphere-Plasmasphere Model to provide the cold ion density and transport along

magnetic field lines and AE9AP9 to provide a static representation of the radiation

particles trapped in the same region. In Chapter 2, representative samples of the

background plasmasphere density and radiation belt fluxes were obtained using the IPM and AE9AP9 models spanning solar and geomagnetic conditions. Initially a simple experiment was conducted to get an idea about how the plasmasphere and radiation particles interact. Using the simple one-dimensional model described in Appendix E, an independent and static ion species was inserted into the F region ionosphere. The response of the F region ionosphere was observed when the independent species was varied in total density and altitude. From the modeled response, expectations for the resulting interaction were used to bound the interaction of the plasmasphere variability to conditions of solar minimum, year 2008 day 180, and maximum, year 2001 day 360.

Described in Chapter 3, the approach to determine density from the radiation flux was employed to evaluate the inner and outer belt populations. The approach highlighted the relative importance of the lower particle energy and greater species mass to contributed to density. As indicated, the "warm", 1 to 100 keV, trapped O^+ ions provided the greatest contribution to radiation belt total density. Due to data limitations in the early releases of AE9AP9, the model output did not exhibit diurnal or season variability and little change due to solar cycle, especially the O^+ ions. As a result, the maximum AE9AP9 trapped radiation density, about 20 #/cm^3, remained constant for the study conditions. As indicated in Appendix C and reiterated in Chapter 4, the increases observed by the Van Allen Belt Probes in outer radiation belts flux during geomagnetic storms were approximated by manually increasing the trapped proton and oxygen ion density from AE9AP9 by a factor of 4. The location of the maximum density of trapped ions was identified as the region of interest for this study having a peak about the equator along the field line L = 3.9, about 18,500 km in altitude.

Modifications to IPM, described in Appendix D, enabled warm static radiation particle density generated from AE9AP9 flux to be inserted as an independent and static species in the calculation of the cold ion density and field line transport in the plasmasphere. Simulations were conducted for the solar minimum and maximum conditions and the results were compared to similar runs without the warm particles. The greatest variation in plasma density occurred at the peak in the radiation density, a region about the equator along L = 3.9, 18,500 km in altitude. In this region during solar maximum, the radiation was 1.4% of the total background ion density of 1500 $\#/cm^3$. During the IPM simulation, the inclusion of the hot particles resulted in a negligible decrease in density for H^+ and He^+ with the greatest change being 1.8% in the region with the maximum radiation density. In this region during solar maximum, the radiation was 1.4% of the total background ion density of 1500 $\#/cm^3$. For the similar solar minimum simulation, where the hot particles were 8% of the total background ion density of 250 $\#/cm^3$, the decrease in density in the H^+ and He^+ was 9% and 8%, respectively. Neither simulation indicated a significant change in the background plasmasphere distribution in the presence of the hot particles form the radiation belt.

Simulations to evaluate the impact of a geomagnetic storm on plasmasphere refilling was conducted for solar minimum conditions. For this scenario, the cold plasma density in the outer flux tubes of the plasmasphere was briefly decreased an order of magnitude, simulating a geomagnetic storm depletion, followed by up flow from the ionosphere and refilling. Comparison of the IPM simulations for this arrangement with and without the inclusion of the warm particles indicated it took 30% longer to return the cold ions to pre-depletion values in the presence of the radiation density. Also, during a

geomagnetic storm the radiation density can increase with time by a factor of 4. A simulation of the storm-time enhancement of trapped radiation was attempted, but proved unsuccessful. Under these conditions the radiation particles were 30% of the background ion density and together with an increasing density with altitude, produced large differential errors where the grids points were sparse resulting in incorrect solutions, often terminating the simulation.

In summary, this study provided an initial survey of the effect on the plasmasphere of "warm" ions trapped in the outer radiation belt. Recent observations indicate that these warm ions are greater in flux, especially at lower energy, than previously expected. This study identified that variations in trapped oxygen ions result in the greatest impact to the refilling of the plasmasphere during solar minimum conditions near the equator at 18,500 km altitude, although the overall effect is small. The impact of the radiation belt during solar maximum conditions was determined to be negligible, however this study provided an indication that frequent enhancements of trapped O^+ during moderate geomagnetic storms may have a more significant effect on the outer region of the plasmasphere, warranting more studies. Additional observations of trapped lower energy ions will continue to clarify the population and variability in the outer radiation belts. Additional studies will require a reformulation of the coupling of the radiation belt and plasmasphere model to address trapped particle density that are comparable, and under special conditions greater, than the upward flowing ions filling the plasmasphere.

REFERENCES

Air Force Research Laboratory. (2016). *AE9/AP9/SPM Radiation Environment Model - Application Programming Interface.* Kirtland, NM: AFRL Virtual Distributed Laboratory.

Albert, J. M., Ginet, G. P., & Gussenhoven, M. S. (1998, May). CRES observations of radiation belt protons 1. Data overview and steady state radial diffusion. *J. Geophys. Res., 103*(A5), 9261-9273.

Baker, D. N., Jaynes, A. N., Hoxie, V. C., Thorne, R. M., Foster, J. C., Li, X., . . . Lanzerotti, L. J. (2014, November). An impenetrable barrier to ultrarelativistic electrons in the Van Allen radiation belts. *Nature, 515*, 531-534.

Baker, D. N., Kanekal, N. G., Horne, R. B., Meredith, N. P., & Glauert, S. A. (2007, October). Low-Altitude measurements of 2-6 MeV electron trapping lifetimes at $1.5 <= L <= 2.5$. *Geophysical Research Letters, 34*, 1-5.

Baker, D. N., Kanekal, S. G., Li, X., Monk, S. P., Goldstein, J., & Burch, J. L. (2004, December). An extreme distortion of the Van Allen belt arising from the 'Halloween' solar storm in 2003. *Nature, 432*, 878-881.

Banks, P. M., Schunk, R. W., & Raitt, W. J. (1976). The topside ionosphere: a region of dynamic transition. *Annual Review of Earth and Planetary Sciences*, 381-440.

Birn, J., Thomsen, M. F., Borovsky, J. E., Reeves, G. D., McComas, D. J., Belian, R. D., & Hesse, M. (1998). Substorm electron injections: Geosynchronous observations and test particle simulations. *Journal of Geophysical Research, 103*(May), 9235-9248.

Conrad, E. E., Gurtman, G. A., Kweder, G., Mandell, M. J., & White, W. W. (2010). *Collateral Damage to Satellites from and EMP Attack.* Defense Threat Reduction Agency. Ft. Belvoir: Defense Threat Reduction Agency.

Daglis, I. A., Thorne, R. M., Baumjohann, W., & Orsini, E. T. (1999). The terrestrial ring current: Origin, formation, evolution and decay. *Rev. Geophys., 37*, 407-438.

Defense Threat Reduction Agency. (2001, April). *Anti-Satellite Weapons.* Retrieved July 13, 2019, from Federation of American Scientist: www.fas.org/spp/military/program/asat/haleos.pdf

Dent, Z. C., Mann, I. R., Goldstein, J., Menk, F. W., & Ozeke, L. G. (2006). Plasmaspheric depletion, refilling, and plasmapause dynamics: A coordinated ground-based and IMAGE satellite study. *Journal of Geophysical Research Volume 111*, 1-14.

European Space Agency. (2013, September 10). *EARTH'S PLASMASPHERE AND THE VAN ALLEN BELTS.* Retrieved June 18, 2019, from http://sci.esa.int/jump.cfm?oid=52831

Facchinetti, G., Sasanelli, N., Davis, M., & Cucinella, G. (2016, December). *Space Intership Program - Small Satellite Economic Trends.* Retrieved January 23, 2018, from Southern Australia - The Defense State: http://www.defencesa.com/upload/Facchinetti%20G.%20Small%20Satellites%20Economic%20Trends%20Dec%202016-FINAL.pdf

Farley, T. A., & Walt, M. (1971). Source and Loss Process of Protons of the Inner Radiation Belt. *Journal of Geophysical Research, 76*(34), 8223-8240.

Fillius, R. W. (1966, January). Trapped Protons of the Inner Radiation Belt. *Journal of Geophysical Research, 71*(1).

Fraser, B. J., Horwitz, J. L., Slavin, J. A., Dent, Z. C., & Mann, I. R. (2005). Heavy ion mass loading of the geomagnetic field near the plasmapause and ULF wave implications. *Geophysical Research Letters*, 1-4.

Gardner, L. (2013). Personal notes on the variables and inner working of IPM. Logan, Utah.

Ginet, G. P., O'Brien, T. P., Houston, S. L., Johnston, W. R., Guild, T. B., Friedel, R., . . . SU, Y.-J. (2013). AE9, AP9, SPM: New Modles for SPecifying the Trapped Energetic Particle and Space Plasma Environment. *Space Science Review, 179*, 579-615.

Hardy, D. A., Gussenhoven, M. S., & Holeman, E. (1985). A statistical model of auroral electron precipitation. *Journal of Geophysical Research*(90), 4229-4248.

Hedin, A. E. (1991). Extension of the MSIS thermosphere model into the middle and lower atmosphere. *Journal of Geophysical Research*(96), 1159-1172.

Hedin, A. E., Spencer, N. W., Biondi, M. A., Burnside, R. G., Hernandez, G., Johnson, R., . . . Virdi, T. S. (1991). Revised Global Model of Thermosphere Winds Using Satellite and Ground-Based Observations. *J. Geophys. Res.*(96), 7657-7688.

Hess, W. (1962). Energetic Particles in the Inner Van Allen Belt. *Space Science Reviews, 1*, 278-312.

Hess, W. (1964). *The Effects of High Altitude Explosions.* National Aeronautics and Space Administration, Goddard Space Flight Center. Washington, DC: NASA.

Hoerlin, H. (1976). *United States High-Altitude Test Experiences.* Los Alamos Scientific Laboratory of the University of California. Los Alamos: National Technical Information Services.

Horwitz, J. L., Comfort, R. H., & Chappell, C. R. (1984). Thermal ion composition measurements of the formation of the new outer plasmasphere and double plasmapause during storm recovery phase. *Geophysical Research Letters*, 701-704.

Jones, C. B., Doyle, M. K., Berkhouse, L. H., Calhoun, F. S., & Martin, E. J. (1982, April 30). *Operation ARGUS 1958.* Retrieved February 23, 2018, from Defense Technical Information Center: http://www.dtic.mil/docs/citations/ADA122341

Keika, K., Seki, K., Machida, S., Miyoshi, Y., Lanzerotti, L. J., Mitchell, D. G., . . . Larsen, B. A. (2016). Storm time impulsive enhancements of energetic oxygen due to adiabatic acceleration of preexisting warm oxygen in the inner magnetosphere. *Journal of Geophysical Research: Space Physics*, 7739-7752.

Kuznetsov, N. V., Nikolaeva, N. I., & Panasyuk, M. I. (2010). Variation of the Trapped Proton Flux in the Inner Radiation Belt of the Earth as a Function of Solar Activity. *Cosmic Research, 48*(1), 80-85.

McIlwain, C. E. (1961, November). Coordinates for Mapping the Distribution of Mangetically Trapped Particles. *Journal of Geophysical Research, 66*(11), 3681-3691.

McIlwain, C. E. (1996). Processes Acting Upon Outer Zone Electrons. In J. F. Lemaire, D. Heynderickx, & D. N. Baker (Eds.), *Radiation Belts: Models and Standards, Volume 97* (pp. 15-26). American Geophysical Union.

Melissinos, A. C. (1993). Nicholas C. Christofilos: His contribution to physics. In S. Turner (Ed.), *Advance Accelerator Physics* (pp. 1067-1081). Geneve: CERN.

Miyoshi, Y., Morioka, A., & Misawa, H. (2000). Long Term Modulation of Low Altitude Proton Radiation Belt by the Earth's Atmosphere. *GeoPhysical Research Letters, 27*(14), 2169-2172.

Nakano, G., & Heckman, H. (1968, April). Evidence for Solar-Cycle Changes in the Inner-Belt Protons. *Physical Reveiw Letters, 20*(15), 806-809.

NASA. (1985). *International solar-terrestrial physics program: A plan for the core spaceflight missions.* Solar Physics. NASA.

NOAA. (2019, May 22). *Solar Cycle Progression*. Retrieved from Space Weather Prediction Center: http://swpc.noaa.gov

O'Brien, T. P. (2017, January 31). Private communication on the internal energy grid of AE9AP9.

Parsec vzw. (2019, June 10). *The Interplanetary Magnetic Field*. Retrieved from SpaceWeatherLive: https://www.spaceweatherlive.com/en/help/the-interplanetary-magnetic-field-imf

Picone, J. M., Hedin, A. E., Drob, D. O., & Aikin, A. C. (2002). NRLMSISE-00 empirical model of the atmosphere: Statistical comparison and scientific issues. *Journal of Geophysical Research, A12*(107), 1468.

Roeder, J. L., Chen, M. W., Fennell, J. F., & Friedel, R. (2005). Empirical models of the low-energy plasma in the inner magnetosphere. *SPACE WEATHER, 3*, 1-11.

Scherliess, L., & Fejer, B. G. (1999). Radar and Satellite Global Equatorial Vertical Drift Model. *J. Geophys. Res., 104*(A4), 6829–6842.

Scherliess, L., Schunk, R. W., Sojka, J. J., & Thompson, D. C. (2004). Development of a physics-based reduced state Kalman filter for the ionosphere. *Radio Sci., 39*(RS1S04).

Schunk, R. W., & Nagy, A. F. (2009). *Ionospheres.* Cambridge, United Kingdom: Cambridge University Press.

Schunk, R. W., Eccles, J. V., Sojka, J. J., Thompson, D. C., & Zhu, L. (2003). *Assimilation Ionosphere Model (AIM).* Final report, Space Environment Corporation, Providence, Utah.

Schunk, R. W., Scherliess, L., Sojka, J. J., Thompson, D. C., Anderson, D. N., Codrescu, M., . . . Howe, B. M. (2004). Global Assimilation of Ionospheric Measurements (GAIM). *Radio Science, 39*(1).

Selesnick, R. S., Looper, M. D., & Mewaldt, R. A. (2007). A theoretical model of the inner proton radiation belt. *Space Weather, 5*(S04003), 1-19.

Shprits, Y., Elkington, S., Meredith, N., & Subbotin, D. (2008). Review of modeling of losses and sources of relativistic electrons in the outer radiation belt II: Local acceleration and loss. *Journal of Atmospheric and Solar-Terrestrial Physics, 70*, 1694-1713.

Singh, A. K., Singh, R. P., & Siingh, D. (2011). State studies of Earth's plasmasphere: A review. *Planetary and Space Science, 59*, 810-834.

Stassinopoulos, E. G. (2015). The STARFISH Exo-atmospheric, High-altitude Nuclear Weapons Test. *Hardened Electronics and Radiation Technology (HEART) 2015 Conference* (pp. 1-5). Chantilly: NASA on nepp.nasa.gov.

Titheridge, J. E. (1998). Temperatures in the upper ionosphere and plasmasphere. *J. Geophys. Res., 103*, 2261-2277.

Van Allen, J. A., Frank, L. A., & O'Brien, B. J. (1963, February). Satellite Observations of the Artificial Radiation Belt of July 1962. *Journal of Geophysical Research, 68*(3), 619-627.

Van Allen, J. A., Ludwig, G., Ray, E. C., & McIlwain, C. (1958, September). Observations of High Intensity Radiation by Satellites 1958 Alpha and Gamma. *Journal of Jet Propulsion, 28*(9), 588-592.

Van Zele, M. A. (2002). Contributions to the Ring Current Energy During Geomagnetic Storms. *Studia Geophysica et Geodaetica, 46*, 33-41.

Vassiliadis, D. (2003, February). Modes of energy transfer from the solar wind to the inner magnetosphere. *American Institute of Physics, 10*(2), 463-473.

Walt, M. (1994). *Introduction to Geomagnetically Trapped Radiaiton.* New York: Cambridge University Press.

Weimer, D. R. (2001). An improved model of ionospheric electric potentials including perturbations and application to the Geospace Environment Modeling November 24, 1996, event. *Journal of Geophysical Research, 106*(407).

Zhao, H., & Li, X. (2013). Modeling energetic electron penetration into the slot region and inner radiation belt. *J. Geophys. Res.: Space Physics, 118*, 1-10.

Zou, H., Zong, Q. G., Parks, G. K., Pu, Z. Y., Chen, H. F., & Xie, L. (2011). Response of high-energy protons of the inner radiation belt to large magnetic storms. *Journal of Geophysical Research, 116*(A10229), 1-11.

Appendices

APPENDIX A

RADIATION BELT IMPACT ON SPACE SYSTEMS

The importance behind understanding the morphology, dynamics and underlying physical processes of the Earth's radiation belts goes beyond scientific curiosity. Since the dawn of the space age, civilization has become increasing dependent on services and information uniquely provided by artificial satellites. The orbits of the artificial satellites encircling the Earth are optimized based on the intended purpose. For some satellite missions the closest distance to the Earth is the best orbit, others are selected to remain geographically stationary, while others are intended to linger over a particular region before moving on to another. The majority of these satellites orbit the Earth with altitudes ranging as low as 300 km and as high as 36,000 km in addition to a few with highly elliptical orbits reaching even greater altitudes. This range of optimum altitudes coincides with the most intense regions of the radiation belts, starting above the atmosphere (~200 km) and spanning equatorial altitudes from 1000 km (L = 1.15) associated with the inner edge of the proton belt to the outer edge of the electron belt nominally at ~38,000 km (L = 7). Because of the detrimental effects of energetic particles on material as well as humans, accounting for the radiation environment is critical to the success of a space system.

Motivation for Model Improvement

Depending on the characteristics of the orbit, satellites will endure varying doses of radiation while traversing the radiation belts over their lifetime. The interaction of energetic particles with the spacecraft can result in temporary and permanent damage to

solar cells, integrated circuits, sensors, and other critical components. For many materials exposure to these energetic particles results in property changes and incremental performance degradation that accumulates over time. Excessive exposure to energetic particles increases the likelihood of producing false signals or reducing performance from degraded components and in the worst case the failure of a sensor or the satellite. Investigations into anomalous spacecraft behavior have also found correlations with significant space weather events and geomagnetic storms. Due to the detrimental effects of radiation the accumulated impact of the background environment and transient space weather events, satellite materials, designs, orbits and operations must be carefully selected and reviewed to ensure the system will function throughout the intended lifetime (Walt, 1994).

With the uncertainty in the solar driven radiation environment and the probabilistic nature of a radiation effect, typical engineering practices encourage satellite designs for accumulated exposures that are two or more times greater than expected during the planned lifetime. Additional measures are taken to address more transient concerns, such as spacecraft charging and crossing the South Atlantic Anomaly. Although these practices increase the likelihood for survival in the radiation environment, they increase cost and reduce performance of the satellite system. The miniaturization of electronics in space systems has greatly reduced the size and power but complicates the design because these devices are often more susceptible to energy deposition from incoming ions. The recent availability in lower-cost launch services has also encouraged the use of commercial components for space applications. Although these commercial components are designed for use inside the safety of our atmosphere, a detailed

knowledge of the radiation environment and the radiation properties of the materials have shown that such systems are practical for spacecraft with limited lifetimes and low altitude orbits. The struggle to develop high performance, yet cost competitive, space systems is the promise of the ongoing "NewSpace" revolution (Facchinetti, Sasanelli, Davis, & Cucinella, 2016). Understanding the composition and energy of the background radiation belts, as well as the expected frequency and magnitude of their variations over time, becomes essential for optimizing of the space system designs for the future.

Anthropogenic Radiation Belt Variations

In 1957, before the discovery of the Van Allen belts, Nicholas Christofilos theorized that large quantities of energetic electrons from the neutron and beta decay of fission products and ionization of the warhead materials from a high-altitude nuclear explosion (HANE) could be injected and trapped along magnetic field lines in the magnetosphere. Additionally, he postulated that a very dense layer of these trapped energetic electrons might have military implications by degrading radio and radar transmissions and damaging or destroying the arming and fusing mechanisms of Inter-Continental Ballistic Missiles warheads passing through the belts (Melissinos, 1993). During that same time, the United States was conducting experiments on the effects of nuclear weapons. Within a few short months after Christofilos published his theory, additional tests were added exploring detonations at higher altitudes. In less than five years a total of seven HANE tests were conducted by the United States and Russia. The earliest occurred in the South Atlantic from August to September of 1958 and were known as operation ARGUS. The ARGUS tests included three nuclear detonations of warheads with approximately 1.7 kilotons TNT equivalent at 200 km (L = 1.7), 240 km

(L = 2.1), and 540 km (L = 2.0). Measurements by Explorer IV and sounding rocket campaigns confirmed the Christofilos theory and the creation of an artificial belt between L = 1.7 and L = 2.2 and having an order of magnitude greater radiation than typically found in that region. These temporary radiation belts contained 3 MeV electrons and exhibited decay times from 30 seconds to 15 days (Jones, Doyle, Berkhouse, Calhoun, & Martin, 1982).

In 1962 the United States planned additional HANE tests under the operations known as FISHBOWL. The FISHBOWL tests were conducted with extensive instrumentation to assess changes in the radiation belt, impacts to radio and radar propagation, and the effect on missile and warhead systems. One of these tests STARFISH PRIME, with a yield of 1.4 megatons TNT equivalent, was exploded on July 9, 1962, at approximately 400 km (L= 1.12) in the South Pacific and about 700 miles southwest of Hawaii. The explosion released about 10^{27} energetic fission electrons into the magnetosphere, creating a thin crescent shaped region of radiation centered at L = 1.2 and with decreasing intensity to 10% of the peak at L = 1.8 (Van Allen, Frank, & O'Brien, 1963). At the time of the test, four satellites Injun, Ariel I, Telstar I, and TRAAC were equipped with electrons detectors capable of sampling changes in the Van Allen belt population. Injun was launched in 1961 and its nearly circular 1000 km orbit provided the first contour maps of the new radiation belt along with a comparison of the environment prior to the test. Measurements from Ariel I indicated that high-energy electrons appeared at high latitudes shortly after the detonation and extended up to L = 5, possibly greater. Additionally, the TRAAC satellite monitored the decay of the low altitude electrons, while Telstar provided measurements above 1000 km (Hoerlin, 1976).

Within a few months, additional satellites were launched with sensors further characterizing the decay of the artificial radiation belt from STARFISH as well as the effects from three Soviet HANE tests in October later that year. These observations illuminated several similar attributes about the inner radiation belt, such as the high-energy proton flux, typically about 2×10^4 /cm^2-sec, did not change appreciably after the detonation. Also, at 400 km where the magnetic field is weaker over the South Atlantic, an increase in 55 Mev protons was observed for about 3 weeks before decaying. Overall, the largest enhancement to the inner zone was the increase of energetic electron with peaks about 10^9 /cm^2-sec, two to three orders of magnitude greater than the natural flux. It was noted that an interesting feature of these artificial belts is the complexity in the observed decay rates of the energetic electrons. At altitudes below L = 1.3, electrons are quickly lost by Coulomb scattering with the atmosphere. Similarly, high-energy electrons above L = 1.7 are also rapidly lost by processes unknown at the time, but suspected to be due to magnetic disturbances. However, for the region between L = 1.3 and L = 1.7 the electron decay rate was found to be greater than a year, in some cases more than 3 years (Hess, 1964). The results from these satellites pieced together a general picture of radiation belt "pumping" associated with a HANE and supported numerous scientific studies for the next two decades.

The United States and Soviet Union were at the dawn of the space age when the HANE tests were conducted. Although the tests were intended to explore the Christofilos concept to neutralize approaching missiles, an unintended consequence of the STARFISH detonation and enhanced electron population in the Van Allen belts was the rapid degradation of orbiting spacecraft. At the time of the tests, 24 satellites were

already in orbit or would be launched in a few weeks. The detonation increased the total

ionizing dose to levels critically impacting several satellites within months after the test.

At least eight satellites suffered damage directly attributable to detonation and within a

year six of them had completely failed. Of these losses the Transit 4B, TRAAC, Ariel,

OSO-1, and Anna-IB satellites failed as a result of power loss from damaged solar arrays

(Conrad, Gurtman, Kweder, Mandell, & White, 2010). The Telstar communication

satellite, launch a day after the STARFISH detonation suffered component failure after

one month. The satellite was temporarily recovered by a commanding work around until

a complete failure occurred 5 months later. It has been estimated that the STARFISH test

resulted in a total dose to the spacecraft that was 100 times larger than expected from the

natural occurring radiation belts (Stassinopoulos, 2015).

By September 1962, concerns were mounting in the United States over the rapid

loss of multiple satellites and the possible interference of the artificial radiation belts with

the upcoming launch of the NASA manned space flight of Mercury 8. Using flux maps of

radiation levels measured one week after the STARFISH detonation, an astronaut on a

six-orbit mission was expected to receive a total dose of 1 Rad (Hess W. N., 1964). The

NASA administrator at that time, Dr. Webb, met with Chief Scientific Advisor to the

President, Dr. Wiesner and President Kennedy to discuss the potential health risk to

astronaut Walter Schirra if additional high-altitude nuclear tests were conducted. Dr.

Webb recommended a delay in the next detonation until after the Mercury launch and

limit future nuclear space experiments to low altitudes. As a result of Dr. Webb's

persuasive argument, the next nuclear detonation Uracca, planned for 1300 km, was

cancelled and the remaining US tests were limited to 10's of kilometer in altitude. By

August 1963, a treaty was signed between the US and Russia prohibiting nuclear weapon tests or explosions in space, the atmosphere, or under water, ending a nearly five-year run with over a dozen high-altitude nuclear detonations (Conrad, Gurtman, Kweder, Mandell, & White, 2010).

Renewed Threat

The United States has a large investment and dependence on satellite systems for military and intelligence purposes as well as services for civil infrastructure. Although the effects of naturally occurring radiation on satellites from solar events has also upset, degraded, and destroyed scores of satellites over the years, the high-altitude nuclear detonation tests from 1958 to 1962 dramatically illustrated the impact on space systems without sufficient protection. Decades of science and engineering investments have resulted in radiation protection and tolerant technology and devices enabling extended lifetimes of space systems in a severe environment. These technologies have been applied to harden some military satellites against credible radiation threats. However, for most satellite designers the increased cost and performance limitations for protection beyond the natural space environment are not advantageous (Walt, 1994).

The increasing threat of the North Korean nuclear and missile programs has renewed concerns about the vulnerability of satellites to a HANE. The North Korean nuclear program successfully conducted 10 kT and 20 kT detonations in 2016 and a larger 140-250 kT detonation in 2017. Additionally, the successful launch of a satellite in 2016 and the demonstration of the Hwasong-15 missile in 2017 create the alarming possibility of a nuclear intercontinental ballistic missile. In 2001, the Defense Threat Reduction Agency (DTRA) conducted the HALEOS study to understand the current treat

of a HANE on low-Earth orbiting satellites. To support the study, the radiation environment was simulated for a low-yield (10 to 20 kT) nuclear detonation above North Korea at 125-300 km altitude. The simulation results indicate that a day after a detonation the radiation along the magnetic field lines corresponding to North Korea and passing through the inner belt increases 3 to 4 orders of magnitude with greater than 1 Mev particle fluxes at 10^8 electrons/cm^2-sec. Additionally, the simulation indicated that after two years collision losses reduce the flux rates at the lower altitudes, but across the inner belt the enhancement remains around 10^8 electrons/cm^2-sec. The study concluded radiation hardening typical of commercial satellites in LEO orbit would be insufficient protection and mission failure could result in as little as weeks to months (Defense Threat Reduction Agency, 2001).

By 2010 it was estimated that there were approximately 1000 Earth orbiting satellites with about 550 in Low Earth Orbit (LEO), many of which are designed, built and operated by commercial entities. Previously, satellites providing critical services were dedicated systems with designs addressing the risk for creditable threats. The evolution of technology and changing economic drivers has altered the paradigm whereby services are also provided through dual-use and leased commercial satellites (Conrad, Gurtman, Kweder, Mandell, & White, 2010). Yet these same changes have also resulted in a divergence in the commercial sector between the traditional space industry and an entrepreneurial space sector identified as "NewSpace." The enticement for new business prospects based on the lower entry cost into space through commercial launches and small, lower reliability and complexity satellites drive the NewSpace sector. A 2010

DTRA Technical Report expressed the concern for commercial satellites to address

radiation threats.

> "Hardening commercial satellites against even one high-altitude nuclear explosion—admittedly an unlikely event in the world view of most investors—would raise costs, reduce financial benefits and, given limits on booster payloads, quite possibly reduce satellite capabilities and competitive position". (Conrad, Gurtman, Kweder, Mandell, & White, 2010)

Yet the projection for the future is a greater reliance on commercial space services,

including the proliferation of small satellites. Although predictions vary greatly on the

contribution for small low-cost satellites to become a relevant stake of the industry, the

potential for this growth sector is evident by the 3000 estimated launches between 2016

and 2022 (Facchinetti, Sasanelli, Davis, & Cucinella, 2016). The risk for military and

civil dependence on NewSpace services, potentially vulnerable to natural or manmade

events of low-probability but highly disruptive, is an important consideration for the

commercial value proposition.

APPENDIX B

CHARGED PARTICLES IN A MAGNETIC FIELD

Particle Trapping in a Magnetic Field

Inside the magnetosphere, the closed magnetic field lines of the Earth dominate the motion of the charged particles. Due to the initial velocity of a charged particle entering the magnetosphere, the particle crossing a field line will experience a force altering its original motion. Known as the Lorentz force, this force is the result of a charged particle moving in a uniform magnetic field. The force on a non-relativistic charge particle is described by

$$\mathbf{F} = q(v \times \mathbf{B} + \mathbf{E}), \tag{B.1}$$

where q is the charge, v the vector velocity of the particle, B the magnetic field and E the electric field. In the absence of an electric field, E=0, the Lorentz force F is perpendicular to both the velocity and magnetic field and dependent on the perpendicular velocity $v_\perp$ to the magnetic field. The Lorentz force results in the charged particle circling the field line with a path described as gyroscopic motion. The radius of the gyroscopic motion is known as the gyroradius ρ and is given by

$$\rho = mv_\perp^2/Bq, \tag{B.2}$$

where m is the mass of the charge particle and B is the magnitude of the magnetic field. Due to the polarity of charged particles, the gyroscopic motion for ions and electrons is in opposite directions. Additionally, an angular frequency Ω of the gyroscopic motion can be written as

$$\Omega = Bq/m, \tag{B.3}$$

and is express in radians per second and is independent of energy. The component of the particle's initial velocity parallel to the magnetic field moves the center of the gyroscopic motion. In a uniform magnetic field and no electric field, the initial parallel motion of the particle results in a helix about the field line (Schunk & Nagy, Ionospheres, 2009).

There are a few additional key relationships representing the motion of a gyrating particle in a magnetic field. For a gyrating particle in a uniform magnetic field, not under the influence of an electric field, the magnetic moment μ must be conserved. The magnetic moment for a non-relativistic particle is defined by

$$\mu = mv_\perp^2/2B, \tag{B.4}$$

where m, $v_\perp$, and B are the same as before. Additionally, in the presence of only magnetic forces, v, the magnitude of the velocity of the gyrating particle is a constant of motion given by the familiar equation,

$$v^2 = v_\perp^2 + v_\parallel^2. \tag{B.5}$$

The significance of these equations is recognized when the strength of the magnetic field about which a particle is gyrating changes. Satisfying the conservation of the magnetic moment, a change in the magnetic field requires an equal change in the velocity perpendicular to the field. Since the magnitude of the velocity is a constant of motion, a change in the perpendicular velocity necessitates an opposite change in the parallel velocity. For helical motion, the effect of increasing the magnetic field decreases a particle's motion towards the stronger field but does not change the gyration. The changing motion or helical pitch of a particle due to an increasing or decreasing magnetic field can be represented by the angle between the velocity and the magnetic field. This convenient term called the pitch angle can be expressed by

$$\alpha = \tan^{-1}(v_\perp/v_\parallel), \tag{B.6}$$

where $v_\perp$ and $v_\parallel$ are the perpendicular and parallel components of the velocity relative to the magnetic field B. A pitch angle approaching 0o describes a motion nearly entirely parallel to the field line, while a pitch angle approaching 90o is predominantly circular motion. In the special case for $\alpha = $ 90o, the parallel velocity is zero and the motion of the particle is a circle about the field line (Walt, 1994). The pitch angle provides a simple relationship for expressing various combinations of particle species, initial velocities and magnetic field strength that yield the same helical motion at the same location. These equations are essential for understanding the motion of charged particles in a magnetic field and are the basis for the radiation belts in the Earth's geomagnetic field.

Guiding Center and Motion in Non-uniform Magnetic Fields

For individual electrons and protons, the Earth's magnetic field appears nearly uniform over the scales of the gyromotion. However, it is the accumulation of slight variations from the helical motion due to non-uniformities in the field that result in important behaviors in the bulk motion of the particles. When working with the motion of charged particles in a magnetic field, it is often convenient to separate the helical motion from the extended trajectory of the particles. This separation is done by representing the motion of particle by the center of the circular motion, called the 'guiding center'. This can be done by expressing the instantaneous position **r** of the particle in terms of the gyroradius ρ and the position of the center of gyration **R** such that $r = R + \rho$. Expanding the magnetic field **B** about the guiding center **R** in a Taylor series and inserting it back into the equation for the Lorentz forces, an equation of motion can be written in terms of the time derivatives of **R** and ρ. Expressing ρ at time t in a

coordinate system with a unit vector $<e_1, e_2, e_3>$ in the direction of B over the cyclotron period Ω, the first and second derivatives can be determined. These derivatives can then be inserted back into the equation of motion and averaged over time by integrating over a complete cyclotron period. Recognizing all time averages of ρ and derivatives of ρ equal zero, with a lot of algebraic manipulation (Walt, 1994), the equation of motion can be reduced to

$$m(d^2\mathbf{R}/dt^2)= q[d\mathbf{R}/dt \times \mathbf{B}(\mathbf{R})] - q\rho^2\Omega\nabla B/2 + \ldots \qquad (B.7)$$

where higher order terms have been neglected and the approximations become less valid as the gyroradius increases. It is more useful to understand the motion of these particles by looking at the components of the guiding center motion parallel and perpendicular to the magnetic field. The parallel motion is extracted by forming the scalar product with the unit vector in the direction of the magnetic field as describe by

$$dv_\parallel/dt = -v^2_\perp(\nabla B)_\parallel/2B, \qquad (B.8)$$

Thus, for motion parallel to the magnetic field the guiding center of a particle will be accelerated in a direction opposite to the gradient in the field. The force on a particle circling the z-axis can be written as

$$F_z = - (mv^2_\perp/2B) \, \delta B/\delta z \, \mathbf{e}_z, \qquad (B.9)$$

where the magnetic field is in the direction of the positive z axis and the gradient is in the –z direction. This force is known as the 'mirroring' force and is independent of the sign, positive or negative, of the charged particle. The significance of this relationship is that a charged particle moving into a stronger field will be repelled regardless of the type of particle or direction of the field.

The perpendicular motion can be determined by taking the vector product of the equation of motion with the unit vector in the direction of the magnetic field. After some math and approximations (Walt, 1994) the velocity perpendicular to the magnetic field can be written in the form

$$dv_\perp/dt = \mathbf{e}_1 \times [(mv^2_\perp/2q\mathrm{B}^2)\nabla\mathrm{B}+(m/\mathrm{B}q)v^2_\parallel\delta\mathbf{e}_1/\delta\mathbf{s}], \qquad (\text{B.10})$$

where s is a unit length along the field line. The first term in brackets is describe as the gradient drift and through time integration with B represented by the first two terms of the Taylor series the gradient drift velocity can be approximated by

$$\mathbf{V}_\mathrm{G} = (mv^2_\perp/2q\mathrm{B}^3) \, (\mathbf{B} \times \nabla\mathrm{B}), \qquad (\text{B.11})$$

Since the velocity is in the direction both perpendicular to $\mathbf{B}$ and $\nabla\mathrm{B}$, the gradient drift will carry the guiding center of a particle azimuthally around the Earth crossing field lines of equal magnetic strength. The second term of the perpendicular velocity is known as the curvature drift and in absence of an electric field can be conveniently describe in a similar form (Walt, 1994) by

$$\mathbf{V}_\mathrm{C} = (mv^2_\parallel/q\mathrm{B}^3) \, (\mathbf{B} \times \nabla\mathrm{B}), \qquad (\text{B.12})$$

allowing the guiding center to translate across field lines of constant B. In both drift cases the velocity is dependent on the charge and energy of the particle. As such the drift motion for negative particles is opposite that of positive ions, resulting in an electric current. An important difference between the two drifts velocities is that the gradient drift is driven by particles with large pitch angle while the curvature drift responds to particles with large $v_\parallel$. The gradient and curvature drift motion along with the mirroring force

describe the essential physics behind the trapping of particles in the Earth's magnetic field (Walt, 1994).

Geomagnetic Particle Trapping

The helical pattern from the equations described previously dominate the motion of charged particles in the magnetosphere because the variations in the geomagnetic field are small compared to the gyroradius. However, it is these deviations in the helical motion due to small non-uniformities in the magnetic field that supports the most interesting effects and governing processing in the magnetosphere. As seen previously, the changes in the magnetic field of the Earth's dipole are very small compared to the gyroradius, so the equations described for a uniform field still apply for electrons and protons of many MeV in the geomagnetic environment. As such, Lorentz forces alter the motion of a charged particle entering the magnetosphere with initial velocity v_{init}, to follow a helical path along the geomagnetic field. Due to the convergence of field lines at the magnetic poles, a particle spiraling along a field line will experience an increase in field strength as it approaches a pole. Through the conservation of the magnetic moment and the constant of motion relation, the initial field aligned velocity of the particle traveling in the direction of the pole will decrease as the particle spirals along its path toward the pole. As the particle continues to approach the pole, the magnetic field strength increases and field parallel velocity decreases until it stops ($v_{\parallel} = 0$). This point on the field line where the strength of the magnetic field has reduced the velocity parallel to the field to zero is known as the *magnetic mirror point* and corresponds to a pitch angle of 90° ($\alpha = 90$).

Even though the parallel velocity has ceased, the particle continues its circular gyration around the field line with the initial gyroradius ρ. Since $v^2 = v_\perp^2 + v_\parallel^2$ remains a constant of motion, the perpendicular velocity of the particle at the mirror point equals the magnitude of the initial velocity ($v_\perp = v_{init}$). Due to the motion and field gradient, the mirroring force will reverse the parallel component of the velocity and drive the particle back up the field line towards the equator, propelling it into the opposite hemisphere. Once in the opposite hemisphere, the particle experiences the same reversal at the conjugate mirror point and returns. It is worth noting that the repulsion of the particle entering a stronger magnetic field is independent of the sign of the charge of the particle or the direction of the magnetic field. The cyclic motion of a particle bouncing between conjugate mirror points traps the particle on a magnetic field line (Walt, 1994). *This trapping of charge particles along geomagnetic field lines is the storage mechanism behind the formation of the Earth's radiation belts.*

Mirror Point

There are several interesting aspects of the magnetic mirror point that are important for the trapping of charged particles in the magnetosphere. First, the geometric alignment between the geographic spheroid and geomagnetic dipole ensures that the mirror point is the lowest altitude a trapped particle experiences along the field line. Depending on the energy and particle species, the transit time between mirror points can range from a fraction to several seconds. If energy is not lost through charge exchange or collision with another particle and the magnetic field remains stable, a particle will remain trapped on the field line bouncing between mirror points. The deceleration and acceleration about the mirror point results in the particle remaining in the location of

greatest atmospheric density for a significant fraction of the transit time. Due to the extended transit time, the altitude of the mirror point dominates the probability of losing energy through a collision and freeing the trapped particle. The extended time at lower altitudes combined with the exponential decrease in atmospheric density results in a sharp cutoff at the lowest mirror point. Depending on the species, the typical lower limit for the mirror point of trapped particles range from 200 km to 1000 km in altitude (Hess, Energetic Particles in the Inner Van Allen Belt, 1962).

The consequence of the increased probability of collision with the atmosphere is the elimination of trapped particles with initial pitch angles below a critical value. Referenced at the equator, the range of initial pitch angles for which a trapped particle will likely be lost through collision with the atmosphere is described as the loss cone. The loss cone is defined as all angles less than the critical pitch angle associated with the lowest mirror point. Due to the approximate 10° offset in the geographic and geomagnetic axis, known as the magnetic tilt, the altitude of the conjugate mirror points will vary. Although this difference may appear small, as particles drift around the Earth at particular geographic locations, the mirror point corresponds to a lower altitude causing previously trapped particles to be lost through collisions with the atmosphere.

With charged particles trapped along magnetic field lines, a convenient representation for the position in a dipole-like field is expressed in polar coordinates with the McIlwain L-parameter, denoted by L. The L-parameter, expressed in units of Re (1 R_e = 6371 km), is the geocentric distance on the equatorial plane of a field line passing through the particle's location,

$$R = L \cos^2 \lambda, \tag{B.13}$$

where R is the geocentric distance in Re and λ is the geomagnetic latitude of the particle position in the meridian plane of the field line (McIlwain C. E., 1961). Tracing the path of a particle along a field line to the surface of the Earth, magnetic latitude can be associated with a particular L value. The geomagnetic latitude ranges from 35° to 67° for L = 1.5 to 7 are the inner more stable regions. Due to distortions in the magnetic field, a simple dipole representation for L does not accurately reflect the magnetic latitude, and magnetic latitudes greater than 65° are not typically accessible to trapped particles.

Ring Current

As a particle spirals into an increasing magnetic field a mirroring force reflects its motion along the field line trapping it between the two poles. The gradient and curvature of the dipole magnetic field imparts small variations in the perpendicular velocity. These velocity variations result in the trapped particles drifting longitudinally around the Earth. Table B.1 compares the gyroradius, gyration period, bounce period and the slower longitudinal drift period for trapped electrons and protons.

Particle at Equator 2000 km altitude	Gyration Radius (cm)	Gyration Period (sec)	Bounce Period (sec)	Revolution Period (min)
50 kev Electron	5×10^3	2.5×10^{-6}	0.25	690
1 Mev Electron	3.2×10^4	7×10^{-6}	0.10	53
1 Mev Proton	1×10^6	4×10^{-3}	2.2	32
10 Mev Proton	3×10^6	4.2×10^{-3}	0.65	3.2
500 Mev Proton	2.5×10^7	6×10^{-3}	0.11	0.084

Table B.1 Characteristic motion for electrons and protons in the magnetic field 2000 km above the equator (Hess, Energetic Particles in the Inner Van Allen Belt, 1962).

The gradient and curvature drifts drive electrons eastward and ions westward establishing a toroidal electric current around the Earth, known as the *ring current*. All particles trapped on field lines in the inner magnetosphere contribute to this westward flow of this current. Due to the negligible energy density of the electrons, it is estimated that 90% of the ring current is due to ions injected from the plasma sheet. These ions have energies from 15 keV to 250 keV and result in a peak current density around $L = 5$. The origin of the ions in the plasma sheet feeding the ring current are from the solar wind and the ionosphere. During magnetically quiet times, the ring current is dominated by solar protons transferred from the magnetotail. During high geomagnetic activity, strong induced electric fields efficiently accelerate O^+, H^+ and He^+ ions out of the ionosphere and into the plasmasheet. *Because of the efficient acceleration of O^+ from the ionosphere during intense storms, this terrestrial ion becomes the dominate species in the ring current* (Daglis, Thorne, Baumjohann, & Orsini, 1999).

When a strong and persistent interplanetary magnetic field (IMF) is orientated south with respect to the Earth's magnetic field ($B_z < 0$), particles in the solar wind can couple and reach the magnetosphere. It is this coupling that injects and accelerates a large number of lower energy protons and heavier ions into the ring current from $L = 2$ to 7, significantly increasing the westward current density. This increased current together with other magnetospheric currents, such as the cross-tail current, induce an opposing global field that decreases the horizontal component of the Earth's intrinsic magnetic field. A sharp decrease in the magnetic field associated with a shock wave of solar effluents is known as a *geomagnetic storm*. The horizontal component of the geomagnetic field is continuously monitored at several equatorial locations on the surface

of the Earth and is used to generate the *disturbance storm time index* (D_{st}). The D_{st} index can range from -50 nT to -600 nT and represents the severity of the geomagnetic storm impacting particles trapped in the magnetic field. The size of a geomagnetic storm is classified as moderate for -50 nT $>$ Dst > -100 nT, intense for -100 nT $>$ Dst > -250 nT, or a super-storm where Dst < -250 nT. Once the IMF changes to north ($B_z > 0$), the ring current is decoupled and the energy decays with O^+ dissipating quickly and protons more slowly (Van Zele, 2002).

APPENDIX C

RADIATION BELT CHARACTERISTICS

Overview

The Earth's magnetic field is largely unaffected by the solar wind out to approximately 7 R_e (R_e = 6371 km). The stability of this portion of the magnetosphere supports the trapping of energetic charged particles along field lines for extended durations. Regions of enduring enhanced energetic electrons and ions circling the Earth are known as radiation belts. The existence of these radiation regions was originally reported by Van Allen in 1958 when describing unexpectedly high-count rates observations from Geiger tubes aboard Explore I and Explore III spacecraft (Van Allen, Ludwig, Ray, & McIlwain, 1958). In the years that followed Van Allen's discovery, numerous experiments were conducted to explore the distribution, composition and physical processes governing the radiation belts. Those experiments led to the characterization of three distinct regions of radiation in the inner magnetosphere: a varying outer belt formed predominately from solar electrons accelerated to higher energies, a middle "slot" region denoted by a low flux of energetic electrons, and a stable inner belt of trapped high-energy protons and electrons.

In the outer limits of the magnetosphere, typically greater than 7 R_e, the variability in the Earth's magnetic field due to changes in the solar wind pressure and less effective population and acceleration mechanisms do not sustain a significant accumulation of energetic trapped particles. This outer region from the mostly stable Earth magnetic field and the shocked solar wind contains the magnetopause and

magnetosheath. These regions are identified with a rapid decrease in particle density but are highly dynamic with large variations due to changes in the solar wind and geomagnetic activity. Penetration of the outer magnetosphere with particles from the solar wind during geomagnetic storms provide a source of particles, while sudden pulses in the solar wind compress the field lines on the dayside potentially leading to large losses of trapped electrons to the magnetopause (Shprits, Elkington, Meredith, & Subbotin, 2008). Although this region of the magnetosphere constitutes only a small fraction of the radiation compared to the outer and enduring inner radiation belts, it is a significant contributor to the production and loss mechanisms supporting the inner magnetosphere.

Outer Radiation Belt

One of the most significant regions for trapped radiation is the outer belt comprised of electrons from the solar wind accelerated to energies from tens of keV to a few MeV. In lower concentrations, energetic protons and other ions predominately sourced from the ionosphere also occupy this region, but are not contributors to the trapped radiation. The high-energy electrons are trapped on magnetic field lines spanning $L = 3.5$ to 7. Nominally this outer belt has a peak at $L = 5$ with a typical electron flux on the order of 107 cm^{-2} s^{-1} sr^{-1} and energy ranging from 100 keV to relativistic (several MeV). Fluxes in this region are enhanced due to changes in the solar wind speed, D_{st}, and geomagnetic storms, with responses on the order of 2 to 3 days (Shprits, Elkington, Meredith, & Subbotin, 2008). It is the least completely understood of the trapping regions in the magnetosphere due to the complexity of the physical processes that govern the

population and depletion mechanisms, the variety of timescales, and the limited observational data across the spatial vastness (Vassiliadis, 2003).

Although the magnetosheath is recognized as the predominant source for electrons in the outer radiation belt, the lower energy of this decelerated solar wind flow is an indicator that there are more complex processes involved than direct insertion into the inner magnetosphere. Instead the energetic particles are the result of a more convoluted path from the solar wind on the dayside, along the magnetosheath to the magnetic tail on the night side and into the magnetosphere through the plasma sheet (Schunk & Nagy, Ionospheres, 2009). Once inside the magnetosphere, the general agreement for the quiescence population mechanism is that electrons from the plasma sheet, with energies from 10 to 100 eV during quiet conditions and up to tens of keV during storms, are injected into the ring current along with ions from the ionosphere and plasmasphere. In the ring current, internal processes accelerate the particles, with some of the trapped electron energies exceeding 7 MeV (Vassiliadis, 2003).

Resonant Wave-particle Interaction

The relatively cold ions and electrons in the plasmasphere support a variety of propagating wave types. The interaction of the hot trapped particles with plasma waves is an important aspect of the acceleration and loss mechanisms in the outer radiation belt. This key mechanism is known as wave-particle interaction and describes conditions enabling energy tranfer between streaming charged particles and plasma waves. From the variety of plasma wave types in the region where particles stream along magnetic field lines, VLF whistler-mode waves, with typically frequencies of a few kHz, dominant the loss of trapped electrons above L = 1.3.

The whislters of interest in the outer radiation belt are right-hand circularly polarized plasma waves traveling parallel to the magnetic field lines. These waves encounter trapped electrons gyrating about the same magnetic field lines. From a stationary observation point, the velocity υ_z of the guiding center of the electron gyration and phase velocity υ_{ph} of the plasma wave in the opposite direction, the sense of these rotation vectors are the same. Further more, the relationship between the wave phase veleocity and frequency is given by the dispersion relation

$$\upsilon_{ph} = c[\omega\,(\Omega_e - \omega)]^{1/2}/\omega_p, \tag{C.1}$$

where $\omega_p = (e^2\,N/\varepsilon_0 m_e)^{1/2}$ is the plasma frequency of the medium, ω is the wave frequency, Ω_e is the electron gyration frequency, N is the electron number density and m_e is the electron mass. The electric ($\mathbf{E}$) and magnetic ($\mathbf{b}$)components of the circular wave exert forces on the electron of charge $-e$ describe by

$$d\mathbf{v}/dt = -e/m\,[\,\mathbf{E} + \mathbf{v} \times \mathbf{b}\,]\,, \tag{C.2}$$

where the components of $d\mathbf{v}/dt$ parallel and perpendicular to the magnetic field line in the z direction are given by

$$d\upsilon_z/dt = -(e/m)\,b\upsilon_\perp \sin\phi, \tag{C.3}$$

and

$$d\upsilon_\perp/dt = (e/m)\,b(\upsilon_{ph} + \upsilon_z) \sin\phi, \tag{C.4}$$

where ϕ is the difference in phase, $\phi = \phi_e - \phi_d$, between the rotation vectors of the gryrating electron and circularly polarized plasma wave. Changes in υ_z and $\upsilon_\perp$ will result in changes to the kinetic energy and pitch angle of the gyrating electron. If the parallel velocity υ_z of the electron satisfies

$$\upsilon_z = (\Omega_e - \omega)/\,k, \tag{C.5}$$

where k is the wave number, then the electron is said to be in resonance with the wave requiring ϕ to be a constant. While the electron and wave remain in resonance, the forces from the rotating electric and magnetic fields of the plasma wave continue to tranfer energy with the gyrating electron. A consequence of the dependance on $\sin \phi$ in the relationships for the change in υ_z and $\upsilon_\perp$ is that the direction of energy transfer between the electron and wave varies over ϕ. For $0 < \phi < \pi$, the electron gains energy at the expense of the energy in the wave, while for $\pi < \phi < 2\pi$, the electron will lose energy to the wave. The change in the kinetic energy of the gyrating electron will result in a corresponding change in pitch angle (Walt, 1994).

Although VLF whistler-mode waves were used as an example to articulate energy transfer for resonant wave-particle interactions, electron flux enhancements in the outer radiation belt are the result of various waves types. As previously described, resonant wave-particle interaction allows trapped electrons to diffuse in pitch-angle as well as energy. An example of pitch-angle diffusion occurs during storms when high-speed streams within the solar wind launch Very, Ultra and Extremely Low Frequency (VLF, ULF, and ELF) whistler-mode plasma waves in the magnetosphere. Near the boundary, these wave-particle interactions are extremely effective in changing the pitch angle and releasing trapped electrons to the magnetopause (Vassiliadis, 2003). Similar, but significantly more complicated, processes are understood for the interaction of other types of waves and particles, such as those for protons. The resonant wave-particle interaction describe previously is sufficiently illustrative as an example of an acceleration and loss mechanism for electrons, the predominate particle in the outer radiation belt.

Radial Diffusion

Wave-particle interaction is a significant mechanism for the acceleration and loss of trapped radiation in the outer belt, but it does not address the observed radial transport of these field-line trapped particles across the L shells. Outside of storm conditions, charge particles entering the outer boundary on closed field lines in the magnetosphere would remain trapped, unable to decend to lower L. The primary process for transporting particles across L shells and dispersing them throughout the inner magnetosphere is known as *radial diffusion*. This important process is possible when the geomagnetic field changes faster than the drift period of the trapped particles; typical of compression due to increasing solar wind. Additionally, for the particles to remain trapped the change in the geomagnetic field must be greater than the gyration and bounce periods. Similarily, the solar wind compresses the geomagnetic field on the dayside of the Earth, so the strength of a particluar field line also changes as it corotates from day to night. In both situations the approximation $\delta\mathbf{B}/\delta t = 0$ remains valid and the particles will remain trapped during the compression and expansion of the geomagnetic field. A consequence of particles remaining trapped while undergoing a change in the strength of the magnetic field is a change in momentum to maintain a constant magnetic moment. This variation in momentum along with the asymmetry in the increase and decrease in the solar wind lead to the diffusion of particles in the magnetosphere.

Since typical drift periods vary from tens of seconds to days, particles will remain trapped along a field line during a geomagnetic perturbation. Rapid increases in the solar wind compress the geomagnetic field and increase the momentum of the trapped particles. As the solar wind gradually decreases, the geomagnetic field relaxes back to its

original strength while expanding towards the original location. The slower expansion of the field allows time for the particles to disperse around the Earth according to their distribution in drift velocity. The change in field strength as the particles drift around the Earth results in a dispersion of momentum and phase as well. During the outward expansion of the geomagnetic field, the asymmetry of the compressed field lines from the dayside to the nightside disperses the particles into a broad band of L shells. The net motion of this process is to transport a small number of particles on the dayside inward, losing energy and decreasing pitch, and while particles on the nightside outward will increase energy and pitch angle. The continuous fluctuations in the solar wind pressure provides a pumping effect, dispersing particles in energy and pitch angle across the outer radiation belt (Walt, 1994).

As discussed, the major mechanisms for changes in the flux density and energy distribution in the outer radiation belt during quiet conditions are from resonant wave-particle interaction, collision losses with the atmosphere, and transport and dispersion from radial diffusion. However, many more nuanced mechanisms are also in play adding complexity to the structure and dynamics of this region. For example, large-scale depletions of the outer magnetosphere occur due to rapid changes in the solar wind, resulting in an outward flow of trapped electrons from the outer boundary.

In contrast, an impenetrable barrier exists on the inner boundary of the outer radiation belt, preventing ultra-relativistic electrons, greater than 5 MeV, from migrating below L = 3.5. This observed barrier was previously thought to be due to wave-particle pitch-angle scattering within the plasmasphere. However, more recent studies show that when exceptionaly strong solar winds compress the plasmapause below L<3, a

population of trapped ultra-relativistic electrons were formed at L = 2.8 lasting 100 days even after the plasmapause returns to L = 5 (Baker, et al., 2014). It is the complexity of this outer region that continues to elicit the attention of experimental and theoretical research.

Slot Region

Early observations of the near-Earth radiation environment identified two separate zones with a persistent void between them. Known as the middle or "slot" region from 2.5 < L < 3.5, it is recognized as a region devoid of trapped high-energy particles. There is general agreement that the slot region is the result of fast scattering losses from strong wave-particle interactions between high-energy electrons in the outer belt and plasmasphere waves propagating in the whistler mode. These plasmaspheric waves known as hiss are trapped inside the plasmapause by refraction. These confined waves strongly scatter trapped electrons into the 'loss cone' causing them to be lost to the atmosphere. This mechanism produces losses of MeV electrons on timescales of 5 to 20 days for L > 2.5. This rapid loss mechanism addressed the elimination of trapped high-energy electrons below the plasmapause, yet lower-energy electrons (~100 keV) would continue to diffuse inward. However, observations from the Van Allen Probes, starting in 2012, indicated high-energy electrons (~10 MeV) were transported to L = 2.8, frequently below the plasmapause location of L = 4. Currently, the accepted explanation for the sharp upper bound of the slot region is that when a strong solar wind event pushed the plasmapause to a low L, below L = 3, exceptionally slow inward radial diffusion of high-energy electrons and weak but persistent pitch angle scattering inside the plasmasphere creates an impenetrable barrier of ultra-relativistic electrons. The lower the plasmapause

descends, the shaper the barrier of impenetrable electrons. This barrier will decay slowly, lasting on order of 100 days, even after the plasmapause has returned to more typical distances around L = 4 (Baker, et al., 2014).

Inner Radiation Belt

In contrast to the outer belt, the inner radiation belt was extensively investigated during the first decade of space exploration, starting with unexplained Geiger count rates from Explorer I. With the addition of observations from Explorer III and the many that followed, this region of trapped protons and electrons is the best understood. With a maximum at L = 1.5, the inner belt is very stable, with energy from a few keV to hundreds of MeV, where protons account for the highest energy, > 10 MeV. The primary reason behind the stability of this region stems from the strength of the Earth's intrinsic magnetic field dominating perturbations from all other sources, such as fields generated by the ring current, effects of field compression from the solar wind, and penetration by solar storms (Hess, 1962), (Fillius, 1966). Below 10 MeV, the population of trapped electrons and protons is the result of radial diffusion or plasma sheet injection, as mentioned previously. However, the unique enhancement of high-energy protons is the result of cosmic rays.

The most significant distinction between the inner belt and trapped radiation at greater L values is the source of the protons with energies greater than 10 MeV. Within the magnetosphere, there are no known mechanisms for solar wind or ionospheric protons to accelerate to energy greater than 10 MeV. These high-energy protons are the result of the spontaneous decay of energetic neutrons produced by cosmic ray collisions with the atmospheric nuclei. As the flood of cosmic rays from outside our solar system

penetrate deeper into the Earth's atmosphere, the probability of a collision with the nucleus of a oxygen or nitrogen atom increases. A product of a cosmic ray collision and a nucleus is a high-energy neutron. Some of these neutrons produced by cosmic rays escape the top of the atmosphere without additional collisions. With a half-life of 630 seconds, a small fraction of the neutrons will decay prior to leaving the magnetosphere. Neutron decay results in a proton, electron, and neutrino. Electrons and protons created by the decaying neutron may be trapped along magnetic field lines if their pitch angles are outside the loss cone. The proton, with a mass much larger than the electron and neutrino, has nearly the same velocity as the energetic neutron before decay. Protons with the highest energy cannot be trapped for $L > 2.5$ because the gyroradius becomes comparable to the diameter of the Earth. As such, the highest energy particles (>10 MeV) trapped below $L = 2.5$ are protons from neutron decay of cosmic ray collisions (Walt, 1994). However, the production rate for trapped protons by this process is very small so the accumulation of a noteworthy population in the inner belt highlights the importance of the low loss rate for trapped particles in this region.

In the inner radiation belt, the time scales for the loss and radial diffusion of high-energy protons is on the order of years. The stability of the magnetic field along with long time scales for production and loss enabled early explorers to establish the sources, sinks and transport mechanisms governing the inner radiation belt. However, long timescale variations due to the 11-year solar cycle are known to exist for this region (Nakano & Heckman, 1968). The increased shielding of the Earth from cosmic rays during high solar activity reduces the already low production of the high-energy protons. Also, during high solar activity the atmosphere expands due to heating and increases the

probability of trapped protons at low drift shells (L = 1.14 to 1.2) to undergo Coulomb collisions with electrons in the plasmasphere or charge exchange with background hydrogen. The net effect for the high-energy protons in the inner belt across the solar cycle is an increase in flux levels during solar minimum and a decrease during solar maximum (Albert, Ginet, & Gussenhoven, 1998).

Electrons in the inner belt are predominatly the result of inward radial diffussion from the outer belt. Although the distribution of electrons in the outer belt includes energies up to several MeV, only the lower energy electrons are able to diffuse across the slot region. Due to the transport from the outer belt, the electron fluxes in the inner belt are correlated to variations in the solar activity. This correlation also results in changes with the solar cycle, but they are asynchronous with the variations observed in the high energy protons. Specifically, during solar maximum there is a greater influx from the outer belt and a lower loss to collisions in the contracted atmosphere of the inner belt electrons. This asymmetry leads to two distinct zones for electron variablilty in the inner belt. The outer region of the belt is dominated by the source and increases during solar maximum, while the inner region undergoes the loss (Albert, Ginet, & Gussenhoven, 1998).

An intersting anistorpic region in the inner belt over the South Atlantic resutls from the alignment offset between the Earth's geographic and magnetic dipoles. Known as the South Atlantic Anomaly (SAA), this is a region where the magnetic field has a geographically local minimum allowing trapped particles to reach low altitudes. When the guiding centers of trapped particles drift across this region, the shift and tilt of the magnetic field results in the mirror point at a lower altitude. Consequency, the lower

altitude corresponds to a denser atmosphere and a greater loss of trapped particles, especially those with the highest energy. Beyond being a phonemom of interest, the SAA poses a hazard to spacecraft traversing this region due to the localized increase in high energy particles, typically only experienced at higher altitudes (Baker D. N., Kanekal, Horne, Meredith, & Glauert, 2007).

Radiation Belt Variability

The trapped particle distributions in the magnetosphere respond to solar variations on multiple times scales; as long as 11-years for the solar cycle and less than a day for solar and geomagnetic events (Walt, 1994). While an increase in inner belt protons occurs during solar minimum with decay times measured in years, the greatest variations in the magnetosphere occur in the trapped electron population following a geomagnetic storm. The geomagnetic storm related variations are predominantly observed in regions for L > 3, where electron fluxes can increase by a factor of 1000 in a few hours and last for days. These changes are the result of complex dynamical processes in the magnetosphere responding to the arrival of interplanetary shock waves and coronal mass ejections launched by the Sun. Moderate solar storms, where IMF is south (Bz < 0) and D_{st} < -50 can launch geomagnetic storms that decrease the geomagnetic field strength for L > 3, in less than a day as well as compress the plasmapause and radiation belts. The impinging solar wind particles and geomagnetic response drive large variations in composition, energy and flux distributions, taking days or weeks to return to pre-storm conditions. Compared to typical quiescent conditions, where the outer radiation peak is at L = 4 and plasmapause around L = 5, storms can drive the plasmapause below L = 3.5 and compress, deplete or enhance the existing belt of trapped energetic electrons.

Depending on the solar cycle, moderate solar and geomagnetic storms that result in the compression of the plasmapause and changes in outer radiation belts, are relatively frequent, taking place approximately 5 to 40 times per year with more than 20 occurrences in most years. Unlike quiescent conditions where the key processes underlying the production and loss in the radiation belts are understood, solar and geomagnetic storms drive temporal and spatial variations that challenge our understanding of the competing mechanisms that dominate the observed dynamic behavior of the radiation belts (Baker D. N., Kanekal, Horne, Meredith, & Glauert, 2007).

There have been many observations correlating solar and geomagnetic storms with dramatic changes in the outer radiation belts, but the enhanced energetic electron flux does not coincide with the impingement of the solar effluence and compression of the magnetic fields. Instead, the greatest enhancement occurs during the declining phase of solar activity, indicated by a decrease in D_{st} and an increase in the solar wind velocity (Baker D. N., Kanekal, Horne, Meredith, & Glauert, 2007). This delayed response in the outer radiation belt indicates that more complicated processes are in play in this region than the direct trapping of solar wind particles. This extended process can be considered in three phases starting after the interplanetary shock waves and coronal mass ejections launched from the Sun impact the Earth's magnetosphere. This first phase is denoted by the arrival of the fast-solar streams and a compression of the magnetosphere, while the decreasing D_{st} indicates the onset of a geomagnetic storm. Although it is not clear what process dominates, the compression results in an immediate reduction of trapped electron for $L > 3$, with the greatest losses at larger L. The start of phase two occurs

approximately a day after the arrival of the fast wind stream when electron rates start to increase rapidly for L = 4 to 6. The electron population in this region can increase by a factor of 10 to 100 in one day and typically includes an increase in the energy across the distribution. The third and final phase is characterized by a continued slow increase for a few days followed by a gradual decline back to pre-storm conditions over several weeks (McIlwain C. E., 1996).

Penetrating Solar Wind

At times the fast streams from solar events penetrate deep into the inner magnetosphere. These occurrences are potentially the most significant natural events, driving rapid variations in the energy, density and composition of particle populations above L = 3. These high-energy solar wind streams often exceed 500 km/sec and penetrate the magnetosphere outward of L = 5. Such streams of charged particles inject electrons into the magnetotail with energy ranging from 100 eV to 1 MeV (Birn, et al., 1998). If not lost by collision with the atmosphere or wave-particle interaction along the magnetopause boundary, the electrons injected by these streams are trapped along field lines and undergo radial diffusion across the inner magnetosphere. In addition to radial diffusion for electrons resonating with quasi infinite palsma waves, the transient solar streams create finite plasma waves, resulting in shock driven radial diffusion. Shock radial diffusion from these transient streams is a more effective dispersion mechanism owing to greater off-frequency particle–wave resonance coupling. Through shock radial diffusion, electrons from a penetrating solar wind stream trapped along a field line more efficiently diffuse in pitch angle, and after the storm subsides and the geomagnetic field returns to its nominal state, the electrons disperse across different field lines (Walt, 1994).

Occasionally, stronger solar events occur where the wind penetrates inside L = 5, compressing the plasmapause and entering the outer radiation belt. These events result in a more complicated competition between the acceleration and loss mechanisms across the radiation belts. Many of the mechanisms for the acceleration, loss and transport of particles during large solar events are still not fully explained and continue to be the focus of much research. As such, these large solar events become naturally occurring experiments for exploring the critical processes governing the behavior of the radiation belts.

One example of a large solar event sustaining scientific interest for many years was a storm observed from October to November 2003. This storm drove $|D_{st}| >200$nT and the solar wind penetration below L = 3, producing exceptional variability in the radiation belts, and is uniquely identified as the Halloween storm of 2003 (Baker D. N., et al., 2004). During the Halloween storm, the Earth's radiation belts were altered in a very short time. An immediate consequence of the solar effluence striking the Earth's magnetosphere on 31 October was the depletion of the radiation belts at all values of L, including protons in the outer region of the inner belt. During this time the plasmasphere was compressed from the nominal L = 4-5 to inside L = 2 and at some longitudes L = 1.5 and remained in this compressed state for many days. Similarly, for two weeks, the outer radiation belt of high-energy electrons was compressed from L = 4 to inward of L = 2.5, the region typically devoid of radiation. For three days following, the energetic electron populations increased to exceptionally high level but in unexpected locations. For several weeks the slot region was filled with high-energy electrons of a greater intensity than typically found at L = 4 in the outer belt (Baker D. N., et al., 2004). Additionally, the

"impenetrable" barrier preventing high-energy electrons from crossing the lower boundary of the slot region was penetrated. The inner radiation belt, previously depleted of protons from $1 < L < 2$, was filled with high-energy electrons having a very slow decay on a timescale of 100 days (Baker, et al., 2014). These enhanced electron populations formed temporary radiation belt for $2 < L < 3$ and a new belt of relativistic electrons in the inner belt $L < 2$ (Zou, et al., 2011). Modeling of the energetic electron penetration indicates that inward radial diffusion supported the flux enhancements observed in the inner belt and slot region (Zhao & Li, 2013).

In situ observations from recent satellite missions provide an indication of the enhancement of protons and oxygen ions during geomagnetic storms with small-scaled injections in the innner magnetosphere. Analysis of data from instruments aboard the Van Allen Probes during storm events indicate a rapid, tens of minutes, increase in radiation belt proton and oxygen ion flux at $L = 6$ but also extending as far down to $L = 4$. A study by Keika on impulsive energetic oxygen enhancements in the inner magnetosphere during the 6 June 2013 geomagnetic storm examined data from the Radiaiton Belt Storm Probes (RSBP) Ion Composition Experiment (ICE) and the Helium, Oxygen, Proton, and Electron (HOPE) RSBP (ECT) instruments aboard the Van Allen Probes. Analysis of RBSP-ICE data for energies <150 keV indicated proton flux increased by a factor of 3 to 5 while oxygen ions increased by a factor of 2 to 4 for the storm event. Additionally the data from HOPE indicated that oxygen ion flux with energy from 100eV to 10keV increased by an order of magnitude between $L = 5$ and $L = 6$ just before the storm (Keika, et al., 2016). Keika attributes the enhancement as the result of a large nubmer of cold and

warm oxygen ions in the inner magnetospehre prior to the storm being transported by strong spatially localized electric fields generated during the storm.

Radiation Belt Summary

Charged particles trapped in the inner magnetosphere form two distinctive belts of natural radiation varying in origin, composition and dynamics. The inner belt of protons from $L = 1.2$ to 2.5, with energy from 1-200 MeV, is the result of nuclear decay of a cosmic ray colliding with an atmospheric atom. These high-energy protons are trapped on the inner field lines for years. Variations of this population fluctuate with the solar cycle due to the expansion of the atmosphere during solar maximum. The expanding atmosphere increases the probability of collision with a trapped proton, resulting in the deterioration of the inner most layers around $L = 1.2$ to 1.5. During large geomagnetic storms, the proton population remains largely unchanged. However, a large population of electrons from the solar wind and ionosphere can be accelerated and transported to this region. Once the storm subsides this overlapping energetic electron population will take weeks to decay to pre-storm conditions.

In contrast, the outer radiation belt from $L = 4.5$ to 7 is predominately populated with electrons and responds on the order of days, and in some cases hours, to the variability in the solar wind. Radial transport, wave-particle interactions and other internal magnetospheric processes continue to accelerate and transport solar wind and ionospheric electrons to relativistic energies (~1-9 MeV). These trapped electrons are stable, however competing wave-particle interaction processes near the magnetopause and solar wind compression of these outer field lines results in significant population losses. Overlapping this region is the ring current where impulses of solar effluences

increase global fields opposing the Earth's intrinsic magnetic field, resulting in geomagnetic storms. The injection of particles into the ring current also provides free energy for the excitation of chorus and EMIC waves, where resonant wave-particle interactions produce fast scattering losses on the dayside but even fast accelerations to MeV energies on the night side.

Intense solar wind streams compressing and penetrating the magnetosphere and geomagnetic storms drive the dynamics of the trapped electron population. Although field compression during the onset of large events may initially strip away these electrons, a day later the trapped electron population will begin to increase by factors of 10 to 100 times per day until the geomagnetic storm reaches its maximum. Even after the geomagnetic storm begins to reside, the outer belt electron population continues modest gains before entering a slow decay phase, taking months to return to pre-storm levels. Typically, a minor species in the outer radiation belt during geomagnetic storms, oxygen ions are efficiently transported and accelerated from the ionosphere by induced electric fields. Frequently, the O^+ ion becomes the dominant species in the outer radiation belt during strong geomagnetic storms. However, due to their larger gyroradius these heavier ions have a greater interaction with the atmosphere, resulting in pitch angles migration to the loss cone and a rapid decimation of the population.

In between the two belts exists the slot region, known for its absence of radiation. Not long after its discovery this region was given little attention by the scientific community compared to its neighboring belts. This region is strongly influenced by the location of the plasmapause and defines the bottom of the outer radiation belt, typically between $L = 4$-5 during quiescent times. Inside this boundary loss dominates through the

wave-particle interaction with plasmaspheric hiss efficiently diffuses electrons in pitch angle and energy and precluding the transport to lower L values. Solar and geomagnetic storms compress and erode the plasmasphere, changing the dynamics of the acceleration and loss mechanisms in this region. The recent the discovery of a temporary radiation belt and an enduring relativistic electron population at $L = 1.8$ after a super storm has rekindled interest and spurred new scientific investigations.

From the discovery of the radiation belts at the dawn of the space age the hazards to orbiting systems was evident. The energetic particles trapped in the Earth's magnetic field resulted in damage to critical spacecraft systems, degrading their performance. Significant enhancements in the radiation belts due to solar events has spurred scientific curiosity as well as developing solutions to mitigate the impact to space systems. Within a few years of the first orbiting satellite, intentional nuclear testing demonstrated the devastating effects to satellites from artificially pumping the radiation belts. Unlike solar driven enhancements, trapped electrons from the beta decay of a high-altitude nuclear detonation may take months, often years, to return to background levels. Although techniques and technologies are available to reduce the impact to space systems from these atypical events, the trend for greater reliance on simpler shorter life satellites reopens concerns about vulnerabilities to the space environment.

APPENDIX D

DEVELOPMENT OF THE COUPLED MODEL

As described in Chapter 2, the models selected for this investigation include the

global Ionosphere-Plasmasphere Model (IPM) and the radiation belt specification model

AE9AP9. Chapter 3 outlined an approach whereby the radiation belt can be represented

in the plasmasphere as an independent species while solving the transport equations for

the density distribution of cold plasma in a flux tube. However, the practical aspects of

coupling the two models had to contend with different units, coordinate systems, and

input parameters as well as reconcile two computational environments, operating

systems, software languages, libraries, interfaces and operating schemes. As a result, this

study entailed a significant software development effort consisting of three major parts;

modifying IPM to deplete the outer field lines and adding an independent species of

energetic particles, creating the EQRAD routines incorporating AE9AP9 and converting

flux into a density, and developing graphical tools to represent the flux and density. This

appendix supplies information important when running the coupled model or modifying

it for future studies. This appendix also captures the reasons for the IPM-AE9AP9

architecture and provides specific details related to the software components, interfaces

and operations used in this study.

Evolution of the IPM-AE9AP9 Architecture

The concept for exploring the interaction of the low-energy radiation and the

plasmasphere was formed prior to the availability of the AE9AP9 model. Early work

using a surrogate, the precursor radiation model AP8, examined the feasibility of adding

an independent species into IPM. Incorporating AP8, a Fortran based model with simple

inputs and outputs, into IPM was straight forward. A test case using AP8 was devised

creating the subroutine EQRAD to encompass the radiation model, retrieving radiation

flux along a field line and converting it into a particle density for use in IPM. The

EQRAD subroutine, including AP8, was compiled and linked with IPM to form a single

executable. The IPM-AP8 model was run and an estimate for the additional

computational time appeared to be a modest, about 10% increase. The output from IPM-

AP8 was not examined because AP8 did not contain the population of lower energy

proton and ion radiation that was the focus of the study.
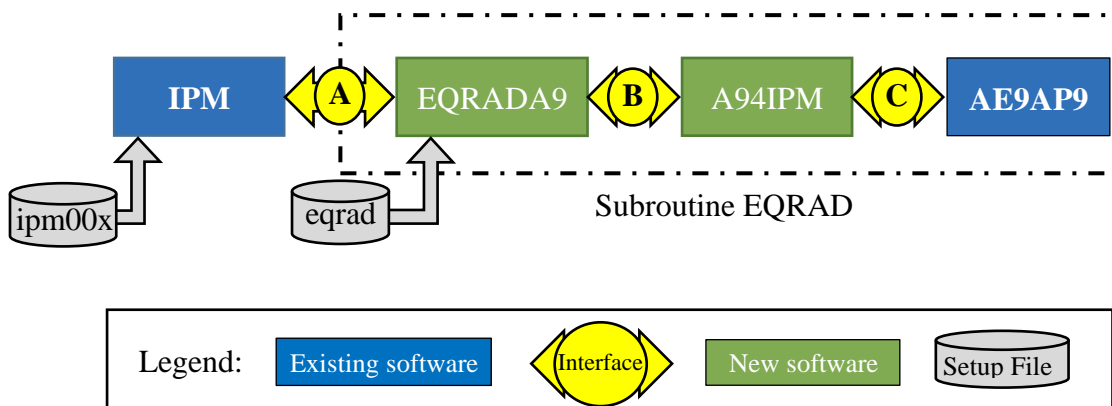
Figure D.1. Block diagram of the software modules and interfaces within
EQRAD intended to provide density to IPM derived from AE9AP9
radiation flux.

Initial distribution of the AE9AP9 model was an executable for the PC computing

environment. Upon the release of the AE9AP9 source code, necessary to compile and

link the model with IPM in the Linux environment, it was immediately apparent that

incorporating the new model would be substantially more complicated than anticipated.

The most significant difference between AP8 and AE9AP9 was the code development in

C and the use of APIs linking the model with external C or Fortran programs. This new

approach required establishing multiple variables supporting 6 APIs to configure

AE9AP9, 1 to retrieve the flux and another to clean up the model. Additionally, these

APIs limited some choices for the input parameters requiring additional conversions for

time and coordinates.
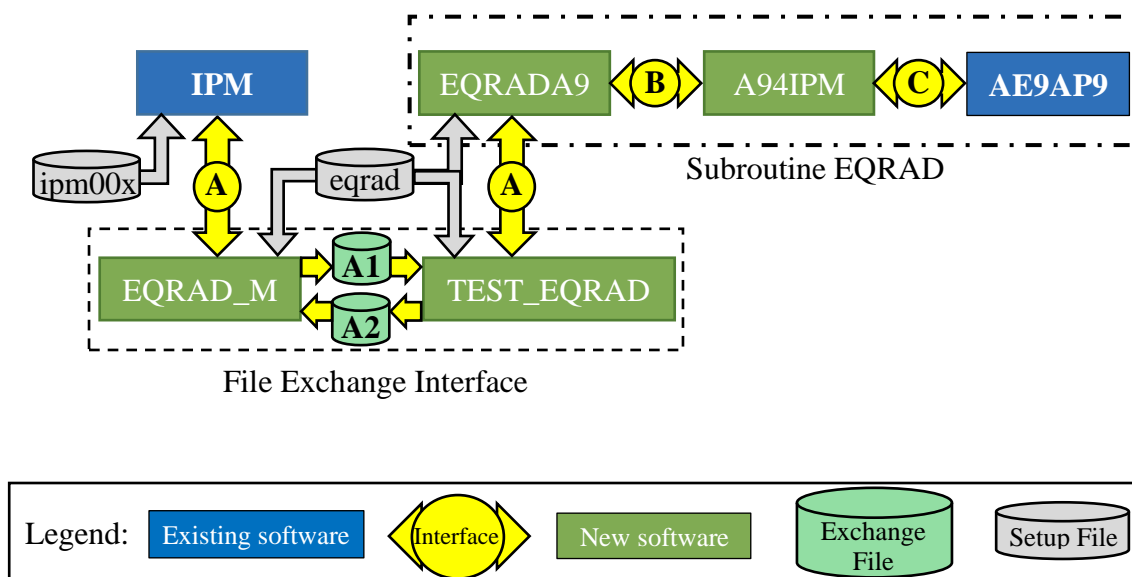
Figure D.2. Block diagram depicting the replacement of the direct link
between IPM and EQRAD with an interface using EQRAD_M,
TEST_EQRAD and the intermediate exchange files A1 and A2.

The original construct for EQRAD was altered to support the Fortran APIs

provided in AE9AP9 release 1.30.01 resulting in two intermediate software modules

EQRADA9 and A94IPM shown in Figure D.1 (Air Force Research Laboratory, 2016).

The two addition of the two subroutines in EQRAD separated distinct functions

simplifying testing. Subroutine EQRADA9 takes the IPM flux tube sample locations,

performs the unit conversion, calls A94IPM providing the radiation flux, converts the

flux to a particle density, aggregates multiple species if required and returns a total density to IPM. When called from EQRADA9, the subroutine A94IPM establishes the variables and calls the APIs to configure AE9AP9 and return the retrieved flux. In its entirety, EQRAD computes the number density at every IPM flux tube sample location from a sum across the energy distribution for one or a combination of particle species (e.g. H^+, He^+, O^+ or e^-) found in the radiation belt.

During integration of the subroutine EQRADA9 into IPM, numerous seemingly small differences in the development environments of the two institutional models necessitated a less sophisticated approach to integration. The simplification having the least impact on the existing software was the separation of two model through a file-based interface. As depicted in Figure D.2, the new interface was inserted at "A" through the creation of two programs using two files "A1" and "A2" to exchange information. EQRAD_M, linked with IPM, creates a file containing the sample locations for every flux tube. It also reads files containing the number density for an independent species along the IPM flux tube. The program TEST_EQRAD was developed to run EQRADA9 independent of IPM. TEST_EQRAD is designed to read the IPM flux tube sample location files and simulate the IPM interface when calling EQRADA9. Once the number density along a flux tube is returned by EQRADA9 the result is written to a file read by EQRAD_M. The use of a file exchange interface instead of linking IPM and EQRADA9 simplified the integration and provided a better opportunity for incremental testing and verification of the system during development. Additionally, the file-based interface allows the two models, IPM and AE9AP9 to be run independently in the most favorable operating environment.

Major Software Development Efforts

Three distinct software development efforts were undertaken for this study; incorporating an additional species into IPM, generating the trapped particle density samples, and developing graphical tools for the 2D representation of the flux and density in the magnetic field. The primary software effort included the cleaning up the Global IPM source code and making the modification necessary to incorporate the warm trapped particles into the solution for the energy and momentum equations as well as support flux tube depletion. The second major software development EQRAD, managed the production of the radiation density under study. The components in EQRAD included the AE9AP9 wrapper, converting the radiation flux into a number density and the handling routines for the file exchange interface. Finally, the IPM unique data grid together with the volumes of data from multiple species and output files across days of simulations necessitated the development of specialized graphical tools. These unique tools enabled the representation and comparison of the AE9AP9 flux and IPM density along the magnetic field lines in a single longitudinal plane. The three efforts presented unique challenges in the completion of this study and a brief description of problem and resolution is presented below along with important information about the models not easily found in other documentation.

IPM Modifications

The Ionosphere-Plasmasphere Model (IPM) continues to provide the foundation for studies involving the evolution of individual plasma flux tubes using first-principals physics. Described in Chapter 2, IPM uses a field aligned numerical solution for the ion and electron continuity and momentum equations for the three major ions (O+, He+, H+)

in the upper F-region and plasmasphere. The IPM core is an efficient and compact set of routines for determining the density along a single flux tube at an instant in time (Schunk, et al. 2004). The extension of the IPM single flux tube core to a three-dimensional global model consisted of roughly 42 Fortran modules including the central program called EQMAIN. The input, output and setup files are ASCII text and the supporting script files are constructed for a Linux host. In the output file, number density ($\#/cm^3$) along the flux tube is specified for every species and is located in space using the spherical coordinates. The IPM output coordinates $<\rho, \varphi, \phi>$ are defined such that ρ is the distance (cm) from the center of the Earth, φ is the colatitude in radians where zero is in the direction of the south pole, and ϕ is the longitude in degrees measured from Greenwich.

When examining the version of IPM provided for this study, it became apparent that EQMAIN had been modified on multiple occasions to conduct different experiments. Lacking descriptive comments within the code, the primary source of documentation for the global IPM came from the notes of Larry Gardner identifying the more significant variables and routines (Gardner, 2013). Although Gardner's notes provided a basic understanding of the IPM code, after attempting to make the initial modifications to introduce a new species, it became necessary to explore the global model in more detail. During this learning effort some modest housekeeping was attempted including internal documentation, expanding the logfile content and cleaning up code fragments from previous experiments. An iterative approach was employed to identify the modification necessary for incorporating the radiation particles. The iterations started by simply adding the external particle density into the computation of H^+, the dominate ion where the radiation density is the greatest. Numerous iterations with increasing complexity were

explored until IPM remained stable with the inclusion of the warm trapped particles. The

following modifications were made to Global IPM:

- Addition of an execution script to simplify the creation of the multiple setup files
- Addition of internal version reporting for major modules
- Additional setup parameters for warm particles and flux tube depletion
- Double precision for all calculations (MSIS, GWS5, & EDM remained unchanged)
- Set lower limit for ion density to control numerical stability
- Disable flux tube shuffling (simulating ExB drift) when using a single flux tube
- Update time and date variables to support year change
- Update MSIS with date, year and solar parameters (originally initial conditions only)
- Create a common block for variables related to radiation density
- Include the radiation density in the solution for H^+, He^+ and O^+
- Include the radiation density as an additional species in the diffusion coefficient
- Call EQRAD to update the radiation density on specified intervals and start date
- Settings to limit the rate radiation particles are added and a scaling of the maximum value
- Option to reduce the cold ions in the outer flux tubes to specified value and given date
- Updated output file to include the radiation density

The majority of changes to IPM occurred in the module EQMAIN, responsible

for establishing all variables, initializing the model, and performing a warm-up on the

previous day of interest. After the warm-up, EQMAIN continues the time evolution of

the numerical solution, updating the global inputs and specifying the species density at

regular time increments. Within every time step a numerical solution for O^+ is obtained

first, followed by H^+ and finally He^+. Once the desired date is reached for injecting the

independent particles, EQRAD_M is called updating the trapped particle density variable.

Although initialized to zero, terms for the additional specie was included in the

calculation of the diffusion and numerical solution coefficients in EQAP, EQAPJ and

EQAPK. An artifact of inserting the radiation species with a density distribution

significantly different than the atmospheric ions caused an instability in the numerical

solution that was only partially resolved; see the section on Coupled Model Limitations for more details.

As IPM steps forward in time, a solution is obtained and the plasma distribution is recorded on user selected intervals; every 30-minutes for this study. The naming convention and format of the IPM output files remains the same as before. The only exception is the addition of one variable at the end of the output file to record the trapped particle density. The IPM filename format is *output_DDD_HH_MM.dat* where DDD is the day of year, HH the hour of the day in universal time and MM is the 15-minute increment. Although consistent with previous IPM output, the filename limits simulations to less than a year. The output file is ASCII and structured without index or descriptors in three blocks providing longitudinal slices through the ionosphere and plasmasphere. The first block lists the local time, universal time, day of year, number of flux tubes and the longitude for every slice around the globe. The second block provides details about the flux tubes. In this block the longitudinal sections are listed in the same order as block one, but the number of grid points, apex, and vertical drift are provided for every flux tube in that slice. The final block is the data block where the fields identified in Table D.1 represent the simulation results for the species density and velocity at the output interval. The fields in Table D.1 are listed in order for every sample position in a flux tube, then repeated for every flux tube in the longitude section, and finally reiterated for all sections around the globe. The density fields used to represent the plasmasphere are H^+, He^+ and O^+ and are identified in bold. The density of the new independent species was added to the data block of the output file as the last entry in the data fields. IPM simulations without an independent species will contain zero for this field.

IPM Data Block Field Label	Units
Chi coordinate along the magnetic field	
Dipole altitude of the grid point	cm
Dipole latitude	radians
NO^+ density	$\#/cm^3$
O_2^+ density	$\#/cm^3$
N_2^+ density	$\#/cm^3$
O^+ density (low altitude)	$\#/cm^3$
H^+ density	$\#/cm^3$
He^+ density	$\#/cm^3$
O^+ density (plasmasphere)	$\#/cm^3$
O^+ velocity	cm/sec
H^+ velocity	cm/sec
He^+ velocity	cm/sec
Electron velocity	cm/sec
Ion temperature	Kelvin
Electron temperature	Kelvin
Colatitude (zero points south)	radians
Radius from the surface of the Earth	cm
Longitude	degrees
Trapped particle number density	$\#/cm^3$

Table D.1 IPM output file data block with the labels and units for the fields provided in order. Bold indicates the plasmasphere density fields.

Additional modifications to IPM provided options to briefly reduce the ion density in the outer flux tubes simulating a geomagnetic storm. Seven new parameters were added to the IPM setup file ipm001.dat controlling the start of the depletion event, affected flux tubes, gradients across the transition, and the altitude and the minimum density within a flux tube. The parameters contained in ipm001.dat are listed in Table D.2. The parameters controlling the reduction of density in the outer flux tubes are indicated in bold. Within IPM, the density of the H^+, He^+ and O^+ species are decimated to the minimum allowed value one time. This event occurs at UT=00 on the day specified in the setup file.

Setup file parameter description	Units
Solar 10.7cm flux	real number
Average solar 10.7 cm flux	real number
Planetary geomagnetic activity index	real number
Combined year and day to start simulation	Integer (Year - 1900) * 100 + DoY
Day of year (DoY) for start of simulation	integer, same as previous
Suggested number of flux tubes per plane	1 – 100 however IPM will add and subtract as needed
Bottom altitude	cm
Top altitude	cm
Deplete tubes after (days)	Days after start of simulation
Deplete tubes on day (DoY)	Deplete flux tubes on specific day
Lowest deplete flux tube	Flux tubes above the equator crossing altitude (in cm) will be depleted
Lowest altitude tube to altitude	Lowest altitude for depletion within a flux tube (in cm)
Minimum depletion density	Minimum density allowed, 0=internal stability criteria
Discontinuity control within a tube	1=in-tube transition algorithm (exponential) 0=abrupt change; discontinuity
Discontinuity control across flux tubes	1=in-tube transition algorithm (exponential) 0=abrupt change; discontinuity

Table D.2 Parameters and description for setup file "ipm001.dat". Bold indicates the new parameters.

Finally, a more comprehensive version of the Linux setup script, *ipm3Drun.sh*, was generated to simplify the initialization of IPM and reduce common user errors due to the multiple setup files and interdependencies within the parameters. The new script automates the creation of the four IPM set files, adds flexibility to select the number of flux tubes, moves the output files to unique folders, creates a text record detailing the parameters in the simulation and terminating all processes when complete. Once the user adjustments are complete, executing the script will build the setup files and launch one or more of the IPM executables. The substantial alterations in the setup script simplified

repetitious interactions and reduced mistakes during the multitude of unique runs required for this study. Although IPM can be executed manually, it is recommended to use this script to maintain configuration as well as providing a document for the conditions establishing each run.

Subroutine EQRAD

As describe previously, EQRAD refers to a group of routines providing IPM the density of radiation particles within a flux tube. The functions performed by EQRAD are translating IPM native units and formats into the inputs required by AE9AP9, running the model and retrieving flux along a field line, converting the flux into a number density, and returning the density for use by IPM. Not including the AE9AP9 model components, EQRAD accomplishes these functions using four distinct software modules, each developed in Fortran specifically for this study. The four software modules are AE94IPM providing the wrapper for the AE9AP9 model components, EQRADA9 for unit conversions and two routines EQRAD_M and TEST_EQRAD handling the file exchange interface with IPM. These software modules are described in more detail below.

By itself, the AE9AP9 model is highly configurable with a variety of options for input parameters and output data products. The model was developed in C++ for use on a Windows host and supports a command line interface or graphical user interface. In AE9AP9 release 1.30.001, the development suite contained an Application Programming Interface (API) in Fortran along with an option to build the model under a Linux host. Although the APIs simplified the integration of the AE9AP9 model written in C++ with the Fortran based IPM, they are more restrictive in input and output options necessitating additional conversions for time and coordinates. Employing the APIs to run AE9AP9

entails calling eight separate routines to setup, run and cleanup the model, Figure D.3(b). The setup APIs select the database for the species of interest, provide the magnetic coordinate model, initialize two neural net databases, establish the adiabatic coordinates and provide the specific parameters for the time, date, location and energy of interest. After setup, an API is called to return the AE9AP9 flux. Finally, the last API is called to reset the model interface and exit. The subroutine A94IPM was created as a wrapper to execute the required APIs and return the radiation flux.

Although multi options are available to produce different products, A94IPM uses the API called *ae9ap9app_flyinmean_f* to specify the radiation flux. The *ae9ap9app_flyinmean_f* API provides the omnidirectional mean flux for the given particle type, time, position, direction, energy along the path of a satellite. Instead of a satellite track, the locations of the IPM flux tube grid was provide to the API. Spherical coordinates were selected as input to AE9AP9 requiring minimal conversion of the IPM flux tube grid. For AE9AP9, spherical coordinates $<R, \varphi, \phi>$ are defined with R as the distance from the center of the Earth in units of Earth radii (R_e), φ the colatitude in degrees and ϕ is the longitude in degrees. To minimize the error in representing the particle velocity, the flux is retrieved as a 2-pt differential. A limitation of the API required the specification of time in Modified Julian Date. A94IPM provides the AE9AP9 omnidirectional mean flux for a requested species in units of #/cm^2/sec/MeV for an entire IPM flux tube.

The next major component in EQRAD is EQRADA9. The primary function of EQRADA9 is translating data structures and units between the native environments of IPM and AE9AP9 as well as converting the trapped particle flux into a density along the

flux tube. The block diagram in Figure D.3(a) identifies the major activities in

EQRADA9. These functions include obtaining the flux tube sample locations provided

by IPM, performing the unit conversion, calling A94IPM to retrieve flux, converting the

AE9AP9 flux into a number density, aggregating multiple species if required, and
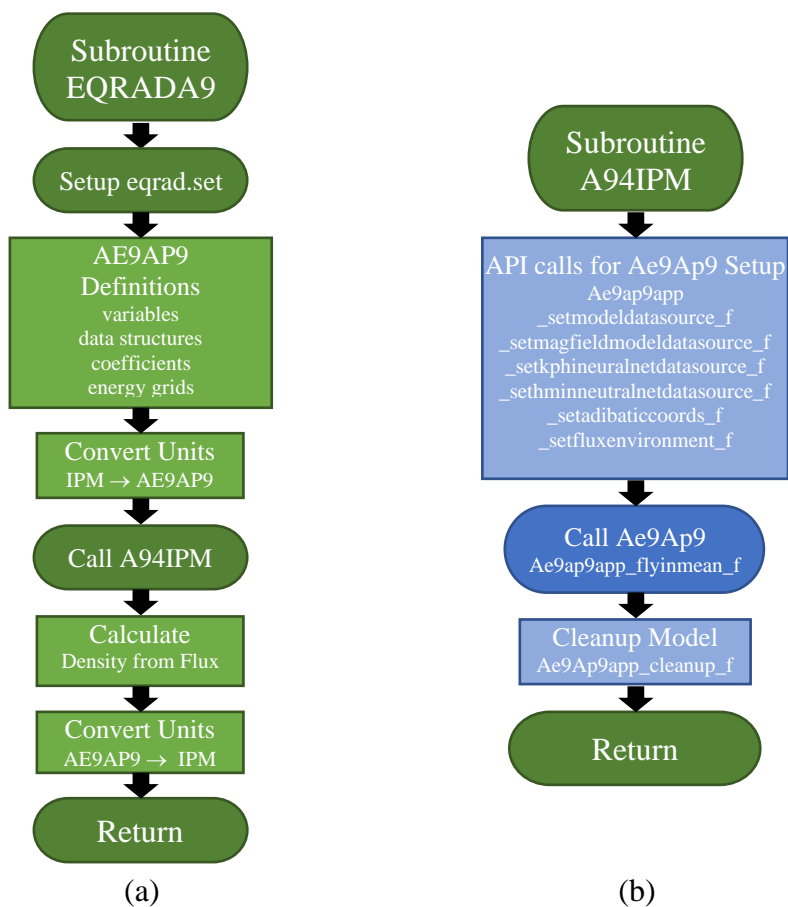
Figure D.3 Block diagrams for the two subroutines (a) EQRADA9
providing all unit conversions and (b) A94IPM forming the AE9AP9
wrapper.

returning a total density to IPM. The subroutine accesses all simulation values, sample

point locations and time, including the return of the computed total density using IPM

common block variables. EQRADA9 uses the setup file "eqrad.set" generated during the

initialization of IPM to determine the radiation species of interest. The "IA9Model"

parameter in the setup file has six switches, one for every particle type available in

AE9AP9; energetic proton and electrons and energetic plasma H, He and O ions, Table

D.5. The switches are used to setup the data structures and parameters to invoke a

specific model, AE9, AP9 or SPM. If more than one switch is selected, EQRADA9 calls

A94IPM for each species and combines them producing a total density.

Prior to calling A94IPM, several conversions are required. The IPM altitude and

the reversed coordinates of colatitude referenced from south are changed to AE9AP9

spherical coordinates $<R, \varphi, \phi>$. Additionally, the IPM time specification of year, day of

year, and seconds in universal time is converted to Modified Julian Day for AE9AP9. As

AE9 > 0.1 MeV protons	0.1, 0.2, 0.4, 0.6, 0.8, 1.0, 2.0, 4.0, 6.0, 8.0, 10.0, 15.0, 20.0, 30.0, 50.0, 60.0, 80.0, 100.0, 150.0, 200.0, 300.0, 400.0, 700.0, 1200.0, 2000.0
AP9 > 0.04 MeV electrons	0.04, 0.07, 0.1, 0.25, 0.5, 0.5, 0.75, 1.0, 1.5, 2.0, 2.5, 3.0, 3.5, 4.0, 4.5, 5.0, 5.5, 6.0, 6.5, 7.0, 8.5, 10.0
SPM $1.15 - 100$ keV H^+, He^+, O^+	1.15, 2.1, 3.7, 6.5, 11.5, 20.4, 36.0, 63.7, 85.0, 100.0
SPM $1.0 - 40$ keV electrons	1.0, 1.3, 1.7, 2.1, 2.8, 3.6, 4.6, 5.9, 7.7, 10.0, 13.0, 16.0, 21.0, 27.0, 35.0, 40.0

Table D.3 Energy grid points used to bin fluxes for the models AE9, AP9 and SPM.

described in Chapter 3, the accuracy of the flux to density calculation is dependent on the

representation of the particle velocity across the band of energy. To minimize the error in

velocity, A94IPM is setup to retrieve a differential flux across 2-points in energy using

the AE9AP9 internal grid (O'Brien, 2017). The internal grid points used to bin the energy

vary by model and species and are provided in Table D.3. To avoid overlap in model output, the AE9AP9 documentation recommended crossover point of 0.1 MeV for protons and 0.04 MeV for electrons was adopted for A94IPM. Once configured, A94IPM is called and the trapped particle flux is returns for the specified time, locations and energy grid. Using the technique described in greater detail in Chapter 3, EQRADA9 calculates a total density from the flux distributions provided by A94IPM, fills the variable RADHP in the common block RADRB for use by IPM. The subroutine EQRADA9, together with A94IPM and the embedded AE9AP9 interfaces, produce the particle density for the requested radiation species along a single IPM flux tube.

File Exchange Modules

As mentioned in the first section, the idea of dynamically linking AE9AP9 into IPM was abandoned due to nuisance differences between the libraries and compiler settings supporting the native environment of the two models. A less sophisticated but ultimately more practical approach to integration of the two models was the use of a file transfer interface. The file interface allowed the two models to be run independently and in separate environment. Changing the interface between IPM and EQRAD from a dynamic link to the file exchange had several advantages. First, it enabled independent testing of the various components simplifying the verification of the flux to density calculation. Additionally, the file interface allowed the generation of the energetic particle density for all flux tubes prior to starting IPM, reducing the overall run time for each case. Finally, the interface files provided an independent record of the of radiation belt density and enabled graphical representation of the EQRADA9 results without running IPM. As mentioned previously, the modules inserted for the file exchange

interface preserved the original interface between IPM and EQRADA9. As depicted in

Figure D.4, the new module EQRAD_M was linked with IPM. Likewise, TEST_EQRAD

was linked with EQRADA9. Each module created and read the interface files A1 and A2

to exchange information between them. The two modules EQRAD_M and

TEST_EQRAD together with interface files A1 and A2 comprise the File Exchange

Module.

File Exchange Interface
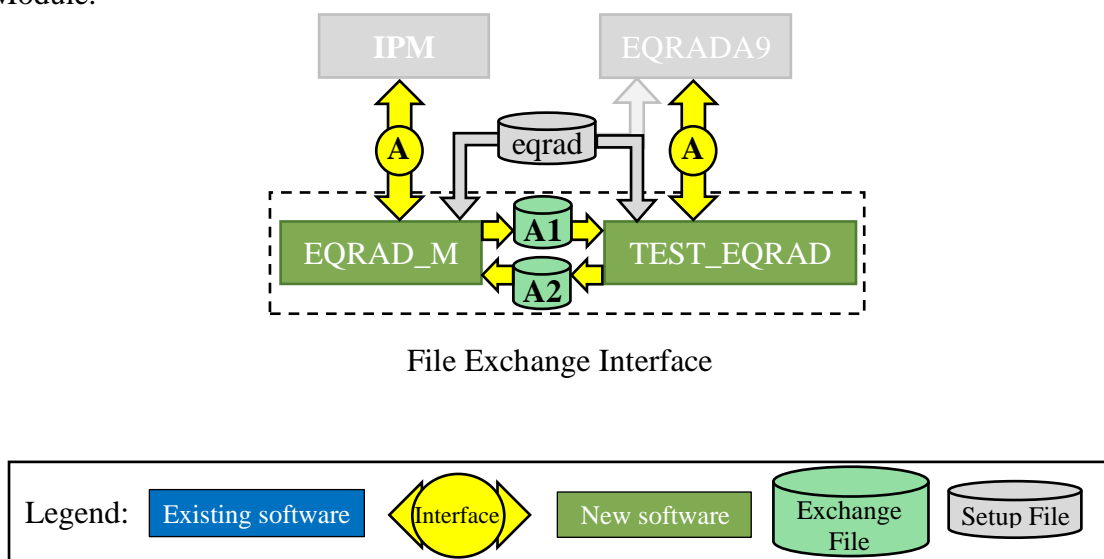
Figure D.4 Block diagram of the file exchange modules providing the
interface between IPM and EQRADA9 using exchange files A1 and A2.

The subroutine EQRAD_M is called by IPM to provide the density of trapped

energetic particles within a flux tube. To maintain the interface developed for

EQRADA9, the energetic particle density is transported between IPM and EQRAD_M

within the same variable RADHP and common block RADRB. The EQRAD_M

subroutine has two functions, either create a new file defining the IPM grid along a flux

tube or read a file containing the density at the prescribe grid points into IPM. As detailed

in Table D.4, the parameters identifying a particular flux tube are captured in the

filename, while the sample points along the flux tube are provided in fields internal to the

A1 and A2 File Name Definition		
A1 template	IPM2Rad_LLL_LON_YYYY_DDD_HH_JJJJ.par	
A2 template	IPMAp9_SS_LLL_LON_YYYY_DDD_HH_JJJJ.dat	
Parameters	Description	Example
SS	Species identified by the array IA9MODEL (only used for A2)	For electrons > 0.04 MeV, IA9MODEL(2) = 1; SS = IA9MODEL(1) + 2 * IA9MODEL(2) + 4 * IA9MODEL(3) + 8 * IA9MODEL(4) + 16 * IA9MODEL(5) + 32 * IA9MODEL(6) = 2
LLL	L Shell *100	L = 1.25; LLL = 125
LON	Longitude in degrees	270 degrees; LON = 270
YYYY	Start Year for IPM model run	Year 2014; YYYY = 2014
DDD	Day of year for current IPM iteration	May 6; DDD = 126
HH	2-digit universal time hour for the current iteration	UT =6.5; HH = 6
JJJJ	Grid points in the IPM flux tube (2000 max)	Index J = 1 to 1599; JJJJ = 1599
A1 and A2 File Content Definition		
Labels	Description	Notes
IPM call for tube ZEQ	Apex altitude (in cm) for the IPM flux tube	magnetic equator crossing
JJ	Number of IPM grid points in flux tube	Identical to filename parameter
UTYEAR	Year for the start of the IPM run	Identical to filename parameter
UTDAY	Day of year for the current IPM iteration	Identical to filename parameter
UTTIME	Universal time in seconds of current iteration	
RATL(1:JJ)	Array of altitudes (in cm) along the flux tube at every grid point (surface defined as radial 6371 km)	
RELONG(1:JJ)	Array of geographic longitudes (in degrees) for every grid point in the flux tube	
RTH(1:JJ)	Array of geographic colatitudes (in radians) for every grid point in the flux tube	Zero indicates due south
RADHP(1:JJ)	Number density (#/cm^3) of trapped particles for every grid point in the flux tube	Every value in this array is set to zero for files with prefix IPM2RAD (A1)
Flux (1:JJ)*	Setup file Action option to include total flux	

Table D.4 Filename and file content definition for interface files A1 and
A2.

file. The reading or writing of files in EQRAD_M is controlled by parameters in the setup

file "eqrad.set" and will be described in greater detail in the next section. When the setup

file action indicates "read," the IPM call to EQRAD_M results in a search for an A2 file

with a filename prefix "*IPMAp9*", extension ".*dat*", and matching the parameters for the

IPM requested flux tube. When the action is set to "write", EQRAD_M creates the A1

file with the prefix "*IPM2RAD*" and extension ".*par*", capturing the IPM sample

locations for a flux tube. However, in this case, the subroutine returns no trapped particle

density for the entire flux tube and zero is recorded in the file for every grid point.

Similarly, TEST_EQRAD is designed to read A1 files produced by EQRAD_M

and output A2 files containing the values for the trapped particle density produced by

EQRADA9. Using the parameters in the setup file, TEST_EQRAD parses the A1 file

into data structures and calls EQRADA9 to determine the density of trapped particles

along the flux tube. Upon the completion of the EQRADA9 call, TEST_EQRAD write

an A2 file with the prefix "*IPMAp9*" and extension ".*dat*" indicating the radiation density

field has been populated. TEST_EQRAD and EQRADA9 are both controlled by the

same setup file, "eqrad.set", and the same parameters as used by EQRAD_M minimizing

mistakes during model initialization and operation. The description for the EQRAD_M

and TEST_EQRAD output and input files are provided in Table D.4, with A1 and A2

using the identical internal format. The only distinction between the two files is the file

prefix and extension for the sole purpose of aiding human readability and organization.

EQRAD_M, TEST_EQRAD, and EQRADA9 are all controlled by the same setup

file, "eqrad.set" and share the same parameters and file. Although the setup file was

originally created for use by only EQRDA9, adding a few additional parameters allowed

one file to control the sequential flow of the three modules or to run independently.

Additionally, the setup file supported testing each module separately, together, and while

running with IPM without any code changes. The setup file is label and position sensitive

Setup file eqrad.set			
Label	Description	Canonical	Possible values
Debug	Integer value controlling the generation of status messages to the screen or log file. Critical messages (failures) are always displayed	1	0 messaging off |1| major functions |2| values of critical variables 3 dump all variables to screen -3 creates a file for each species > 0 written to screen < 0 written to log file
Action	Integer value for the operating mode of the modules including testing with a simulated density, manual. When set to 1 the density is set to zero. Note: If IPM and EQRADA9 are directly linked this parameter is ignored	2	TEST_EQRAD & EQRAD_M 0 Creates A2 with simulated data 1 Creates A1 file, density=0 2 Convert file type A1 to A2 3 Loads IPM requested A2 4 value of L at tube peak, else 0 5 appends total flux to end of file
IA9Model	Integer array of 6, position sensitive, switching on or off the particles of interest; 1 – selected 0 – ignored Note: selecting multiple species produces a total density	1,0,0,0,0,0	Position, Specie 1, > 0.1 MeV protons 2, > 0.04 keV electrons 3, < 0.04 keV electrons 4, < 0.1 MeV protons 5, < 0.1 MeV H_e atoms 6, < 0.1 MeV O atoms
RBstart	Day of year to include the radiation density	Start day +3	>365 indicates the next year
RBscale	Used by IPM to scale the radiation density	1.0	>0
RHPadjst	Use to modify radiation density (RADHP) above/below 45/-45 degrees latitudes	0.0	0 Off <0 set RADHP = 0.0 >0 set RADHP = constant
RBinter	IPM time interval to update the radiation density	86400	Integer value no less than the IPM step interval, default is once per day
RB_out	Hours after particle injection to create an IPM output file every timestep	0	0 Off
Inj_rate	Allows a slow start for the injection of particles (0.01% ~ 30 days)	0.0	0 Off <100.0 percent increase per time step
JJ	Grid points in the flux tube (2000 max)	1599	Used only by TEST_EQRAD
LONG	Integer longitude in degrees	264	Used only by TEST_EQRAD
UTYEAR	Integer year for the start of the IPM run	2006	Used only by TEST_EQRAD
UTDAY	Integer day of year for current IPM time step	077	Used only by TEST_EQRAD
UTTIME	Integer universal time in seconds of iteration	28800	Used only by TEST_EQRAD
ZEQ	Real altitude (in cm) for the flux tube apex	6000.0	Used only by TEST_EQRAD
MDEC	Real magnetic declination for given longitude	-13.0	Used only by TEST_EQRAD
END	End of file marker regardless of value	0	

Table D.5 Valid labels and parameter descriptions for the setup file "eqrad.set". Note: all numerical values start in column 11.

so the label names must match exactly as described in Table D.5 and the associated values must start in column 11. If the leading characters do no match a valid label then the entire line will be ignored. If the file "eqrad.set" is not found, a warning statement is provided and default values stored internal to the program will be used. A description of the valid parameters for the setup file is presented in Table D.5 along with canonical values. The setup file "eqrad.set" is automatically created when IPM initialization script is run however the file is formatted for human readability and can be easily modified.

<u>Displaying Results</u>

The graphical representation of the IPM output in two-dimensions (2D), latitude and altitude, was an unexpected challenge this study. The effect of the radiation particles on plasmasphere is expected to be small and occur at the high altitudes where the background density is very low. Identifying this effect on the background plasma density requires comparing the IPM output at different times and on different days as well as across runs using different conditions. Using less than 1600 sample points per flux tube, IPM uses an irregular spacing to efficiently support the resolution required for the numerical solution where the density is large and change is the greatest and minimized excess computational burden in the low-density regions. This unique grid spacing within a flux tube combined with changing locations of the tubes eliminated the direct comparison of density at specific sample locations. Attempts to apply existing resampling algorithms to place the density onto a uniform grid for comparison resulted in relatively large errors in the lowest density regions due to the few sample points. Additionally, it was desirable to display the full extent of the flux tubes in as accurate a representation of

the geomagnetic fields to assist in interpreting the results. Numerous attempts with different graphing packages and existing algorithms were unsuccessful.

The solution used in this study for the 2D representation of the plasmaspheric density is not optimal but sufficient. Using the Interactive Data Language IDL, an algorithm for decimating the dense grid at lower altitudes, preserving the model results at high-altitudes, and smoothly transitioning between the two was created. The decimation algorithm was applied to every flux tube in the latitude-altitude plane at one longitude. Using the spacing of the new flux tube grid and calculating the distance between the tubes, a marker approximately filling the space between points and flux tubes is placed at every sample location in the plane. The color of the marker is chosen to represent the density at the sample location. A choice between a linear and logarithmic density-color scale is available with color banding to enhance the interpretability. However, this solution is slow where the plot using 100 field line can take up to 45 minutes. For a quick preview, options in the program can skip field lines or decimate the flux tube grid even more reducing the plotting time to about 5 minutes. At the end of the plotting there is an option to generate a graphics file. If save in a graphics file, the bottom edge of the image contains text identifying the data source, program version and output file name for provenance.

An additional program was created from the IPM 2D plotting routine for the displaying the interface files. Since each interface file contains only one flux tube, all files related to the 2D plane are read in prior to graphing. This additional program provides a tool to monitor the flux and derived density from AE9AP9 prior to ingesting

by IPM. These two programs were used to create the 2D density and flux plots prominent throughout Chapter 2.

Model Testing and Integration

The strategy for developing the coupled IPM and AE9AP9 model is based on identifying and building confidence with critical components prior to assembling them together as a system. Once the attributes of the individual components were understood and proper functions verified, they were sequentially integrated and tested. In coupling IPM and AE9AP9, five critical components were identified; installation and operations of the IPM and AE9AP9 models, interface development to call and exchange data with each model and the conversion of AE9AP9 particle flux into number density for use in IPM.

The installation of IPM was simplified by replicating a previous instantiation on the same server, thus ensuring the correct operating environment. After replication, several runs were made and the output verified against the results from the original version to the setup and operation was correct. For AE9AP9, AFRL was contacted to obtain a copy of the development suite. Although not onerous, the requirements to install and build AE9AP9 were similar yet different enough from the IPM environment that a standalone platform was used, avoiding any library or supporting software version conflicts. The AE9AP9 development suite included multiple test cases and gold standard results to verify the model was built and operated correctly. Next, test Fortran interfaces for IPM and AE9AP9 models were developed. For IPM the interface was used to identify the variables necessary for defining the grid point along the flux tube, determining how best the subroutine should handle them, and comparing the content in the test subroutine to the values inside the model. After testing the interface for IPM, this subroutine was

used to create EQRADA9. Developing an interface for AE9AP9 consisted of a

standalone program using the Fortran APIs to initiate the model and retrieve flux

distributions. The extracted AE9AP9 flux distributions were verified by comparisons to

values retrieved using the command line model interface. After testing was complete, this

program became the A94IPM subroutine. The final critical model component, the

conversion of the flux distributions into a density of trapped particles, did not have a

reference for verification. Since the calculations were moderately tedious, an Excel

spreadsheet was created as a cross-reference. A standalone Fortran program was created

for the conversion calculation and several samples were produced to compare the results

against the Excel spreadsheet. The core of this test program was copied into the

EQRADA9 subroutine.

Once the testing of the individual modules was complete, they were run in

conjunction with IPM. At first the "eqrad.set" Action parameter was set to 1, generating

A1 files for every flux tube, but also returning a value of zero for the trapped particle

density. The IPM results were compared to IPM results prior to making any code changes

to ensure that there were no unintended consequences. After completion of these tests,

EQRAD_M and TEST_EQRAD were modified to create a new mode for end-to-end

testing. When TEST_EQRAD is provided a zero for the Action parameter in "eqrad.set",

a simple parabolic density profile is simulated for every flux tube. This unique density

shape is written to A1 and A2 files and is easily identifiable in the IPM products as well

as in EQRADA9. Additionally, another test mode was added to the Action parameter. If

Action is set to 4, within EQRADA9 the L-shell value is inserted at the apex of every

flux tube and the remaining sample positions are identically zero. These modes are

tracers to use as end-to-end check for errors or issues across the interfaces and graphing routines.

Additional parameters exist in the setup file setup file "eqrad.set" support testing when integrating the subroutine into IPM. The "Debug" parameter controls the verbosity of details provided on-screen or log files. If the parameter is set to -3, files are created containing the flux and density for the individual species. Similarly, if the "Action" parameter, used primarily for controlling the file interface is set to 5, a total flux is included in the output exchange file.

Operating IPM with AE9AP9

The most efficient method for operating IPM with the added radiation density species is a three-step process. First IPM is run to obtain the undisturbed plasmasphere background and flux tube parameter files. The resulting parameter files are processed using TEST_EQRAD producing a radiation density file for every flux tube. Finally, IPM is rerun with the trapped particle density files, incorporating the radiation flux from AE9AP9 into the solution and capturing the results in the output files. To aide keeping track of the numerous simulations, the script file *ipm3drun.sh,* as described above, was created to simplify the launch of IPM and provide a record of the input parameters. In the *ipm3drun.sh* file header, the user can adjust the simulation unique condition such IPM start and end dates, when the radiation is injected into the simulation or the day the outer flux tubes are depleted. Additionally, within the file header the user can make a few adjustments to IPM internal model functions, such as the number of longitude planes, output time step, and the number of flux tubes in a longitude plane. The number of flux tubes can be set to as few as 1. When using more than 10 tubes, IPM can initiate multiple

concurrent runs to reduce processing time. Up to five concurrent runs can be established, with the boundaries set using the altitude of the flux tube apex (in cm). It is in the file header where the user can select IPM to produce the undisturbed background or incorporate the radiation density.

Prior to running an IPM simulation with trapped particles, a file containing the warm particle density for every flux tube is required. This is accomplished by first running IPM to produce an undisturbed background. To run IPM without the radiation particles requires the *Action* parameter in the *ipm3drun.sh* file header to be set to "1" prior to execution. An *Action* of "1" forces the creation of A1 (IPM2RAD) files for every flux tube and ensures the variable containing the radiation density is zero. With this setting IPM will produce the undisturbed plasmasphere background and generate the flux tube files for the next step. Next the A1 type files generated during the undisturbed run are processed using TEST_EQRAD. For every A1 file, TEST_EQRAD will determine the trapped particle density using AE9AP9 and create an A2 (IPMAp9) companion file. After the A2 files have been generated by TEST_EQRAD and placed in the same folder where the A1 files were created, the *Action* parameter in the *ipm3drun.sh* file header to be set to "3", and IPM launched. With the *Action* parameter set to 3, EQRAD_M will ingest the A2 files during the IPM call and inject the density of energetic trapped particles into the flux tube calculation. The format for the IPM output files with and without the trapped particles is the same and described in the previous section. The additional species is the last field in the output file and for cases without the trapped particles the density will be zero.

IPM Warm-up and Stabilization

After initialization, IPM must run for a period of time to "stabilize" before the output is considered dependable. This stabilization time is handled as an internal "warm-up" day with no output and the convention to wait an additional day of simulation before using the results. In effect, an IPM simulation should be initiated two days prior to the day of interest. However, a comparison of IPM output across multiple days revealed that the density in flux tubes above 7000 km take significantly longer to equilibrate and is dependent on solar activity and season. Although it is known that transport of ions from the ionosphere may take days or weeks to refill a flux tube in the outer plasmasphere, quantifying the few percent perturbations expected from the radiation particles necessitates the simulation reaching equilibrium.

To determine the IPM settling time for the outer region of the plasmasphere IPM simulations upwards of 180 days were made while keeping the environmental conditions fixed. Using a single flux tube with an equator crossing of 18,500 km, trends in IPM total density were examined for the same local time but different initial seasons, solar and geomagnetic activity. From these simulations, a settling time in days since model initialization was determined. As depicted in Figure D.5a, when initialized on day 355 for northern hemisphere winter, IPM reached equilibrium after 13 days for solar minimum and 106 day for solar maximum conditions. Similarly, Figure D.5b depicts settling times of 40 and 75 days for solar minimum and maximum conditions when the model was initialized on day 175, northern hemisphere summer. The reason for the reason for the extended equilibrium time by IPM in this region is unknown but is unlikely to impact the results of the study. However, to simplify quantifying the results in this study it was

prudent to wait until IPM had stabilized, 40, 75 or 110 days before injecting the warm

radiation belt particles.
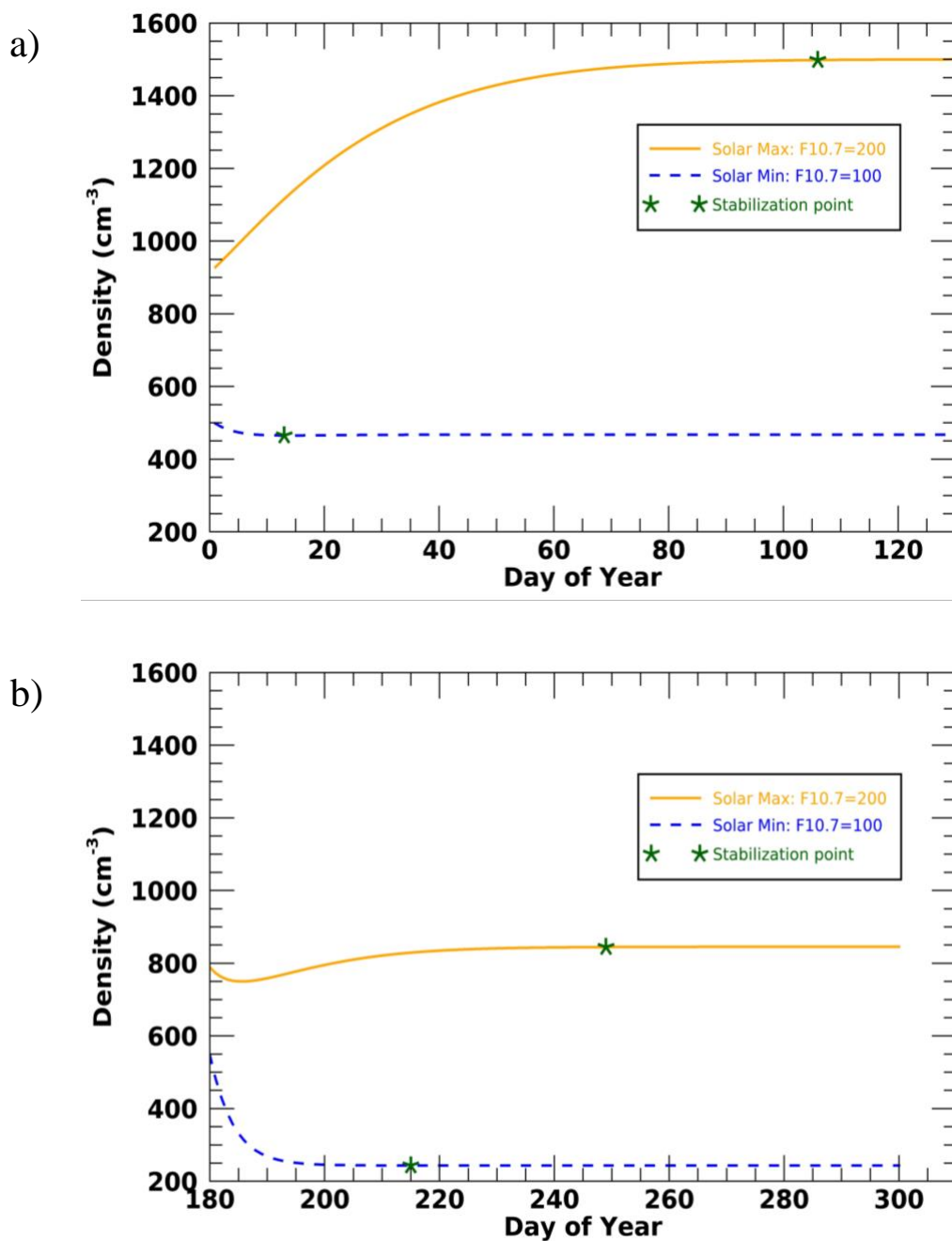
Figure D.5. Daily total density used to trend IPM equilibrium for solar minimum and maximum conditions when a) IPM is initialized on day 355 and b) IPM is initialized on day 175.

Coupled Model Limitations

There are several key limitations to IPM-AE9AP9 coupled model. Some are the result of the approach taken to couple the models and some are inherent to the model themselves. As described above, combining the two models into a single executable became unreasonably difficult. As an alternative, running the two models independently added complexity in the creation of interface files and careful record keeping throughout the numerous simulations. Additionally, the coupled model runtime became excessively long with 100 days of simulation of multiple flux tubes from 600 km to 20,000 km taking well over a week to complete. In an effort to minimize the time to test variations of the model under a variety of conditions, the coupled model was run for a single flux tube at L = 3.9 with an equator crossing of 18,500 km altitude, where the radiation belt particles were expected to have the greatest effect.

A limitation internal to the Ae9Ap9 model results from insufficient data sources to capture the diurnal, seasonal and storm effects of the radiation belt flux. This model limitation was mitigated by scaling the trapped particle density inside IPM simulating belt enhancements. However, the greatest limitation to this study was inherent in the numerical solution used in IPM. To solve the transport equations for the density distribution of cold plasma in a flux tube at every time step, IPM employees a numerical solution optimized for a density that decreases roughly exponentially with altitude. Additional computation efficiency is obtained through the use of an irregular grid where by more points are used at low altitude where the density is higher while fewer points are used where the density is typically lowest, higher altitudes. These two aspects of the IPM design caused a numerical instability when the warm trapped particle density approached

a few percent of the background plasmasphere density. The primary reason for the numerical instability is the increasing warm particle density at higher altitudes where the computational grid spacing is large. The large grid spacing and the differencing of first and second derivatives in the numerical solution drove the model to produce erroneous results. In an effort to resolve the instability, IPM was converted to double precision calculations. This modification resolved the numerical stability of the solution and enabled simulations where the trapped particle density was less than 10% of the background plasmasphere. When the warm particle density exceeds 10% of the background cold plasma, the numerical solution remains stable however the solver often converges on an erroneous distribution of plasma density. Additional investigations to examine the cause of the erroneous solution identified a mismatch in the change in density and the diffusion coefficient calculation across grid points along a flux tube at high altitude. Reviewing the approach and results of the initial F-region simulation described in Appendix E revealed that the numerical issue had been avoided, even for an independent layer comparable to the background ion, owing to a small spatial grid sampling compared to the change in density. Moderate efforts to resolve the mismatch were attempted however a more comprehensive approach was abandoned over concerns for maintaining the integrity of IPM. In the end, the implementation of the numerical solution in IPM limits the use of the IPM-AE9AP9 coupled model for more extensive studies of radiation belt enhancements and plasmasphere depletion during geomagnetic storms.

APPENDIX E

1-D MODEL FOR IONOSPHERE-RADIATION BELT INTERACTION

Background

A layer of charged particles inserted into an F-region plasma model is a highly idealized yet sufficient approximation to investigate the boundary between the radiation belt and the colder terrestrial plasma distribution in the ionosphere. In this appendix a simplified trapped energetic particle model and highly idealized F-region ionosphere model are combined to explore their interaction. Also presented is a sample of model results indicating the change in the plasma density near the trapped particles. This model was initially used to tests the physics behind the trapped particle interaction and identifies the characteristic responses in distribution of the ion and electron density from 120 km to 800 km. The results of this highly simplified representation of the energetic particle interaction with the cold plasma was used to lay the ground work for a more complex radiation belt – plasmasphere model.

The ionosphere model used for this test was adapted from the F-region ionization derivation provided in Appendix O of *Ionospheres* (Schunk & Nagy, Ionospheres, 2009) as a numerical solution to the continuity and momentum equations. The numerical technique results in a time dependent solution for the distribution of the electron and oxygen ion densities. The altitude distribution of the solution exhibits the characteristic shape of the F-region about the peak ionization. Simulating the energetic particles in the radiation belt, an independent non-varying proton layer, n_p, was inserted into the F-region derivation. The modified F-region model was run for a variety of proton layers of

different density and altitude. For every layer variation, the F-region model iterated in time until equilibrium was obtained. The resulting altitude-density profiles confirmed the expectation that a layer of stable protons causes a repulsion of the oxygen ions and attraction of electrons about the peak of the proton layer.

Model Development

The basis for the 1-dimensional F-region model is described in *Ionospheres* and relies on several simplifications to obtain a numerical solution. These assumptions are reasonable for a mid-latitude ionosphere and support the inclusion of an additional species representing the trapped charge particles. In this region of the ionosphere, the plasma is predominantly due to photoionization of neutral atomic oxygen and is lost in chemical reactions with N_2 and O_2. As stated in the *Ionospheres* derivation, the assumption of a horizontally stratified electron distribution reduces the continuity equation to

$$\frac{\partial n_e}{\partial t} + \frac{\partial}{\partial z}(n_e u_{ez}) = P_e - k_\beta n_e, \tag{E.1}$$

where the number density of electrons, n_e, equals the number density of O^+ ions, n_i, preserving charge neutrality. Additionally, the production rate for an optically thin atmosphere is given by

$$P_e = 4 \times 10^{-7}\, n_{[O]}, \tag{E.2}$$

and the loss rate for electrons is given by

$$k_\beta = 1.2 \times 10^{-12} n_{[N2]} + 2.1 \times 10^{-11} n_{[O2]} \tag{E.3}$$

where $n_{[O]}$, $n_{[N2]}$ and $n_{[O2]}$ represent the number density for neutral atomic oxygen, molecular nitrogen, and molecular oxygen, respectively, as a function of altitude z.

Further simplifications assume there is no neutral wind or imposed electric field and the magnetic field is aligned with the vertical altitude axis z. Additionally, it is assumed that the ion and electron temperatures are isothermal. The background thermospheric environment, including altitude profiles of O, N2 and O2 density and the neutral temperature, is provided by the empirical model NRLMSISE-00 Model 2001 (Picone, Hedin, Drob, & Aikin, 2002) and is expressed in cm^{-3}. The thermospheric environment is retrieved from NRLMSISE-00 to initialize the F-region model using the geographic location and local time under investigation. Additionally, the thermospheric model requires inputs for F10.7 and A_p, the indices representing the solar flux and planetary geomagnetic activity.

The influence of the radiation belt on the terrestrial plasma is modeled as a snapshot in time of the energetic particle flux incident on the top of the ionosphere. This instantaneous approximation allows the flux of particles to be represented as an additional species of protons with a static distribution. Additionally, this representation assumes these protons are not influenced by the cold ionosphere as well as imposing charge neutrality. A parabolic distribution in altitude was applied to these particles, forming a layer at a specified altitude and peak density. A more realistic representation of the radiation belt may have been a graduated density of charged particles with a cutoff at the magnetic mirror altitude. However, for the purpose of exploring the boundary interaction, this simple approach is sufficient.

Applying the afore mentioned assumptions and including a term for the energetic particle contribution, the momentum equation for the F-region becomes

$$n_e u_{ez} = -D_a \left[\frac{\partial n_e}{\partial z} + n_e \left(\frac{1}{T_p} \frac{\partial T_p}{\partial z} + \frac{1}{H_p} \right) + X^* \right],$$ (E.4)

where the scale height H_p and diffusion coefficient D_a are provided in Appendix O by Schunk and Nagy. The additional term X^* represents the contribution due to the static layer of protons and is expressed as

$$X^* = \frac{T_e}{(T_e + T_i)} \left(\frac{n_p}{n_e} \frac{\partial n_e}{\partial z} - \frac{\partial n_p}{\partial z} \right),$$ (E.5)

Following the derivation provided in *Ionospheres* and substituting the momentum equation into the continuity equation yields a second-order parabolic, partial differential equation for the electron density, given by

$$\frac{\partial n_e}{\partial t} = A_1(z,t) \frac{\partial^2 n_e}{\partial z^2} + A_2(z,t) \frac{\partial n_e}{\partial z} + A_3(z,t) n_e + A_4(z,t),$$ (E.6)

where A_1, A_2, A_3 are the same coefficients given in Appendix O, while A_4 is modified to include the layer of charged particles by

$$A_4 = P_e + D_a \left(\frac{\partial X^*}{\partial z} \right) + \left(\frac{\partial D_a}{\partial z} \right) X^*.$$ (E.7)

In Appendix O, Schunk and Nagy use an implicit numerical technique to solve this linear, parabolic, partial differential equation. Equating the production and loss processes at the lower boundary and allowing for diffusive equilibrium at the top boundary satisfies the two necessary boundary conditions for this differential equation. Additionally, equating the production and loss terms at all altitudes,

$$n_e = \frac{P_e}{k_\beta},$$ (E.8)

provides the initial condition for the electron density. Using space-centered derivates for

the partials of the electron density with respect to the altitude z and a forward time

derivative for the partial of the electron density with respect to time t, the electron density

terms in the partial differential equation form a tri-diagonal matrix. Inversion of this

matrix yields the electron density state at the next time step. A solution for the F-region

density is accomplished by using the electron density profile obtained in the previous step

to adjust the tri-diagonal matrix. The matrix is inverted again yielding the electron

density for the next time step. The electron density profile for the layer of protons is

added to the inversion results prior to adjusting the tri-diagonal matrix. This process is

repeated in a time loop to obtain the time-dependent solution.

Initialization

The F-region model described above includes a simple parabolic representation of

an independent species of protons used to explore the response of the ionosphere for

different layer conditions. The modified F-region model was run for various

combinations of peak altitude and peak density for the proton layer. The peak density for

the independent layer protons was varied from $1x10^4$ cm-3 to $1x10^6$ cm^{-3} while the range

of altitudes for the peak ranged from 450 km to 650 km. The combination of altitudes

and peak density where selected to represent the variety of energetic particle distributions

expected in the radiation belts.

Ionospheric parameters					
Lower bound	Upper bound	Δz	Ion Temp	Electron Temp	Δt
120 km	800 km	10 km	1000 °K	1000 °K	150 sec

Table E.1 F-region model ionosphere parameters.

For each model run, the ionospheric and thermospheric initial conditions were selected to represent a moderately active Sun. These parameters, summarized in Table 1 and Table E.2 below, remained constant for all combinations of altitude and density variations for the proton layer.

Thermosphere parameters						
Day of Year	Local Time	F10.7a	F10.7	A_p	Latitude	Longitude
172	Noon	220	220	4	45°N	0°

Table E.2 Thermosphere parameters used to obtain NRLMSISE-00 neutral density.

Model Results

The F-region model was initially run without the addition of a proton layer to provide an undisturbed ionosphere baseline identified as the background ion and electron density. Starting at an altitude of 450 km for the center of the layer, the model was run for eight proton density increments ranging from $1x10^4$ cm^{-3} to $1x10^6$ cm^{-3}. Figure E.1 through Figure E.4 are selected results from the simulation with the layer compared to the undisturbed the background.

The first indications of perturbations in the background ion and electron density occurred when the peak density of the independent layer of protons was within 10% of the background ion density at the same altitude. As the density in the proton layer increased the perturbations in the ion and electron density also increased. The F-region model was repeated simulating the same proton density variations with a layer altitude of 500, 550, 600, and 650 km. Three representative results were selected from the simulations and displayed in Figure E.5 through Figure E.7. For the represented proton

layer heights, similar perturbations in the ion and electron density were observed and

correlated to the relative density between the proton layer and the original background.
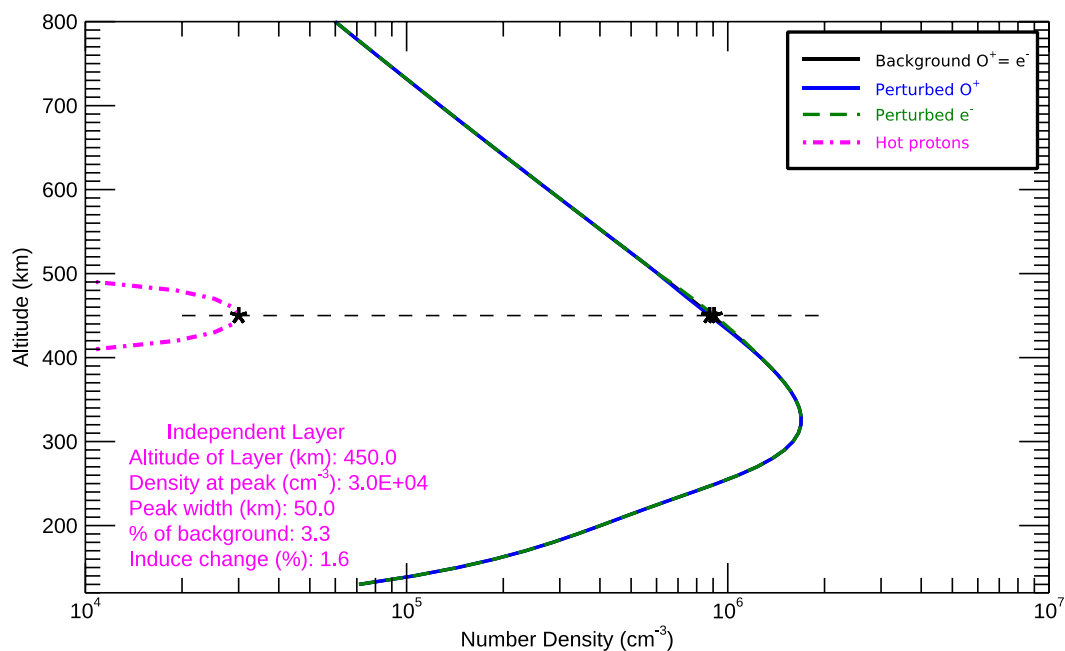
Figure E.1. Results after inserting a layer of protons at 450 km with peak $3x10^4$ cm^{-3}, ~3% of the background ion density at the same altitude, indicates little change in the ion (blue) and electron (green) density distributions.
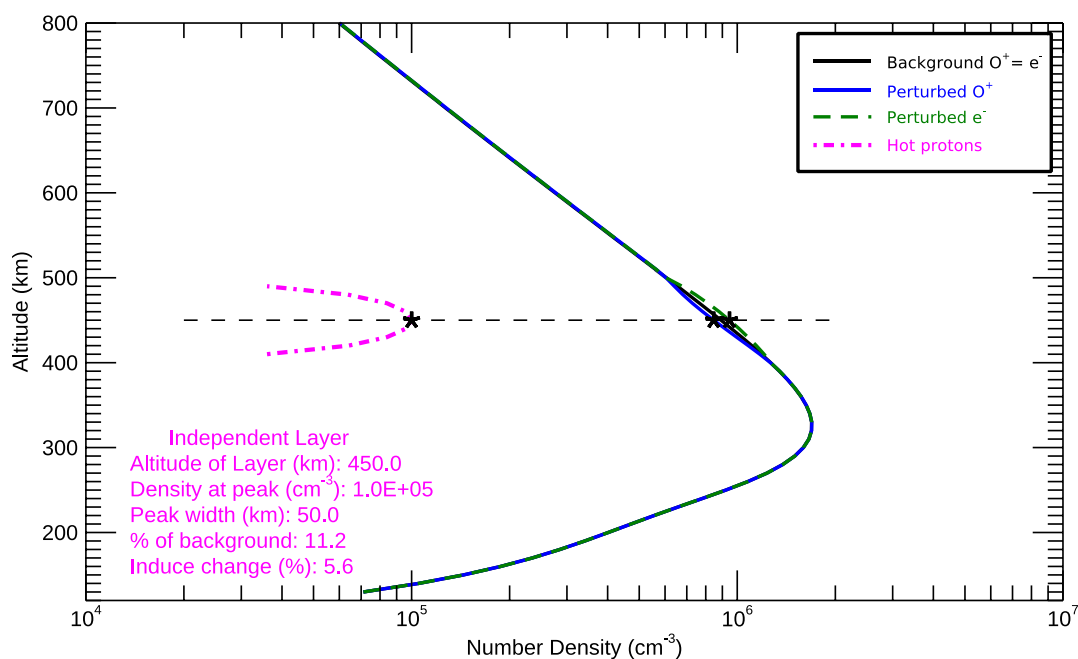

Figure E.2. Results after inserting a layer with peak density of $1x10^5$ cm^{-3}, ~11% of the background ion density, indicates a ~5% perturbation in both the ion (blue) and electron (green) density distributions.
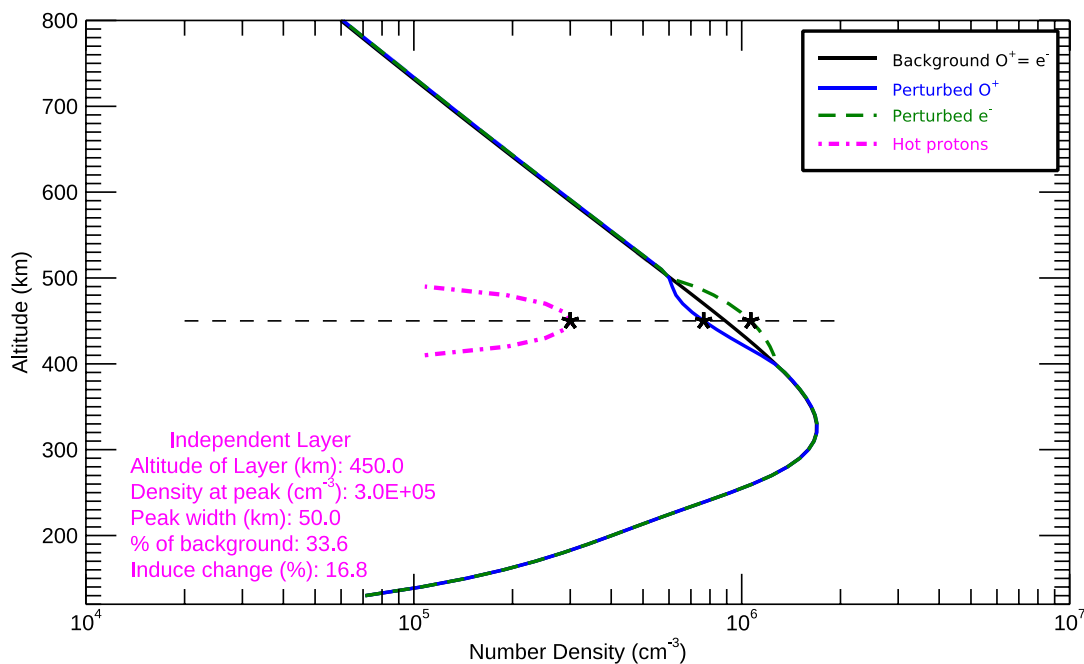
Figure E.3. Results after inserting a layer with peak density of 3×10^5 cm^{-3}, ~33% of the background ion density (black) at the same altitude, indicates a ~17% perturbation in both the ion (blue) and electron (green) density distributions.
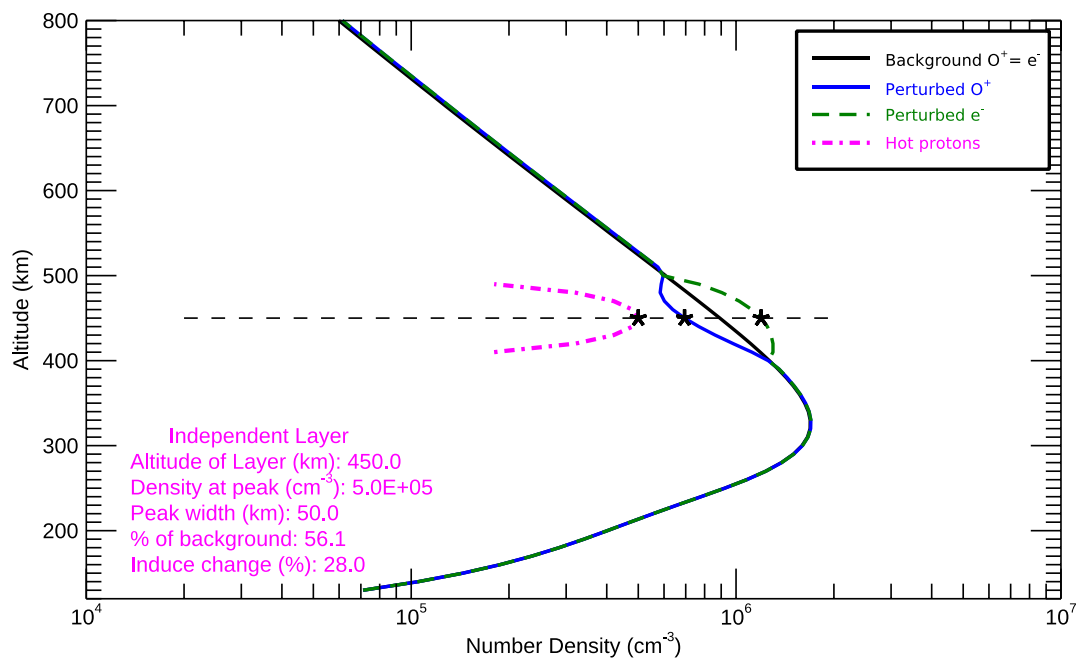

Figure E.4. Results after inserting a layer with peak density of 5×10^5 cm^{-3}, > 50% of the background ion density (black) at the same altitude, indicates a 28% decrease in the ion (blue) and similar increase in the electron (green) density distributions.
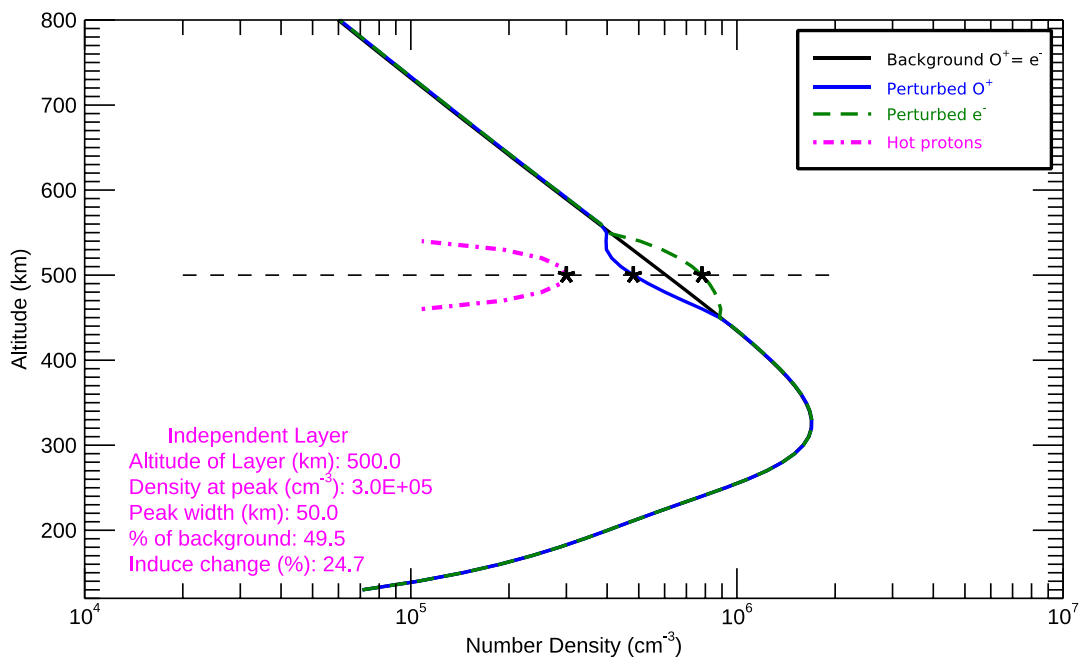
Figure E.5. Results for a proton layer peak density of $3x10^5$ cm^{-3} and center altitude of 550 km. Similar to Figure E.4, a layer with ~50% of the background ion density, decreased the ion (blue) and increased the electron (green) density each by 25%.
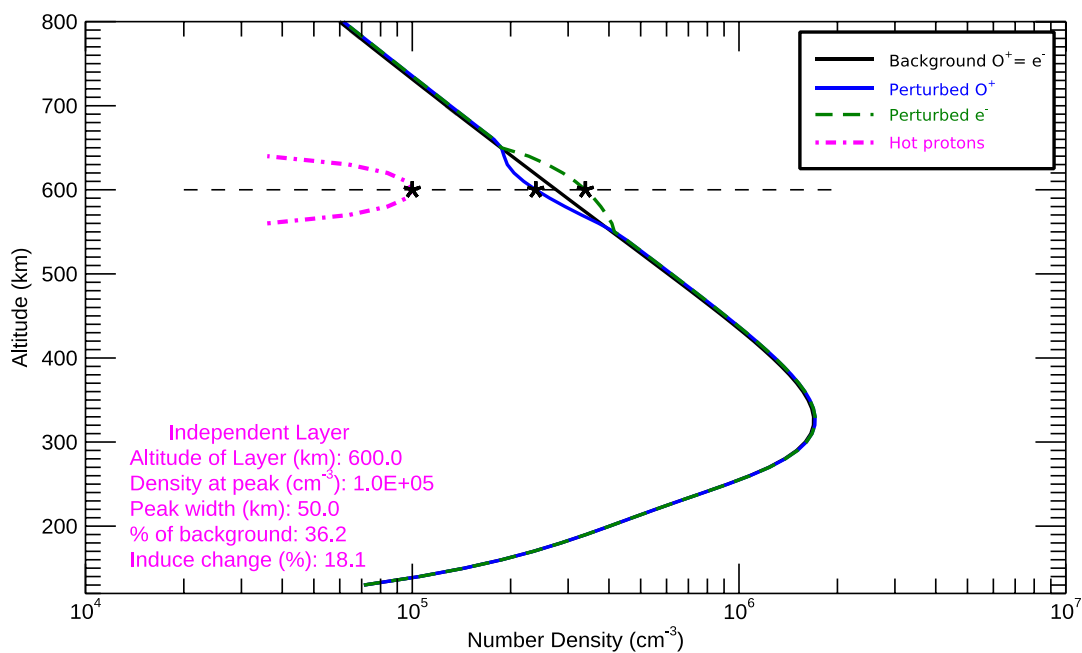

Figure E.6. Results for a proton layer peak density of $1x10^5$ cm^{-3} and center altitude of 600 km. The layer having ~36% of the background density at that altitude, decreased the ion (blue) and increased the electron (green) density each by 18%.
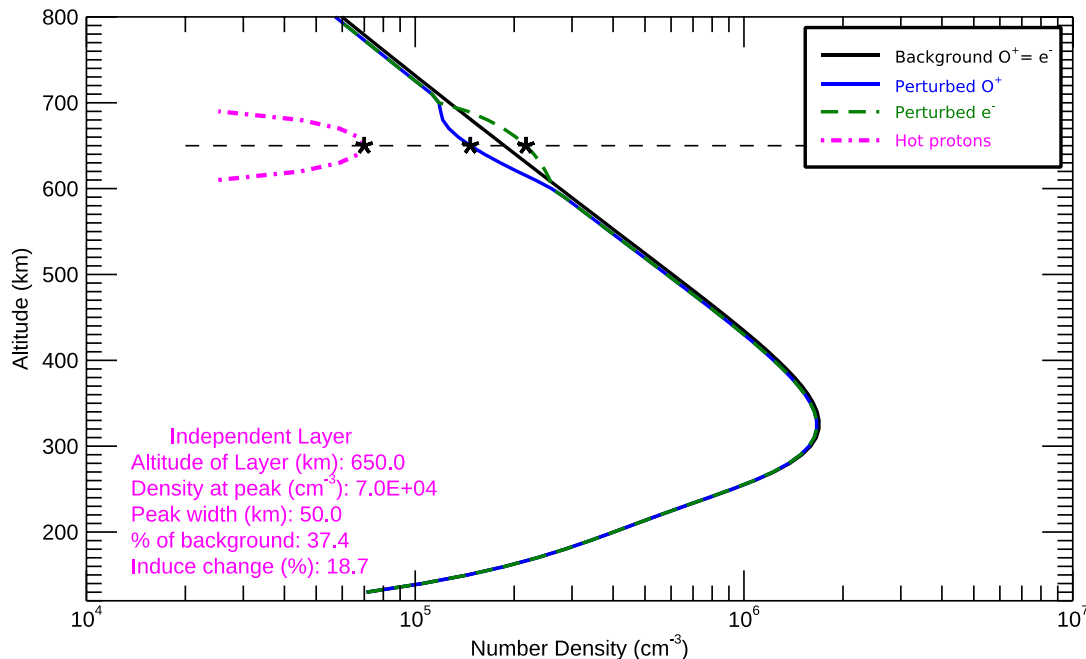
Figure E.7. Results for a proton layer with peak density of 7×10^4 cm^{-3} inserted at 650 km. The layer having ~37% of the background density at that altitude, decreased the ion (blue) and increased the electron (green) density each by ~19%.

## Summary and Implications

An independent layer of protons inserted into the topside of the F region ionosphere was modeled using a modification to the simple 1-D numerical approach provided in *Ionospheres* by Schunk and Nagy. The model was run and results obtained for proton layer altitudes varying from 450 km to 650 km and peak density from 1×10^4 cm^{-3} to 1×10^6 cm^{-3}. A comparison of the O$^+$ and electron density profiles with and without the additional layer indicated the expected perturbation. Due to the positive charge of the protons, the O$^+$ ions were repelled near the peak of the layer, producing a local decrease in the density profile. Similarly, the resultant electron density has a local increase due to the attraction to the protons. Furthermore, the results indicate that the

effect of the layer on the ionosphere is negligible, less than 5%, for proton densities an order of magnitude or less than the ambient plasma at the same altitude.

Although this 1-D model of the F-region ionosphere included many simplifying assumptions, the results demonstrate the effect of the addition of a charged particle layer on the distribution of O^+ and electrons. This simple test indicates the potential for plasma density perturbation in locations where the ionosphere and radiation belts overlap and the density of trapped energetic particles is within an order of magnitude of the local plasma density.

<div align="center">

CURRICULUM VITA
Stefan Thonnard

</div>

CAREER OBJECTIVES:

To obtain a position that leverages my experience in space science and space system development while providing me the opportunity to grow as a leader and expand my technical understanding of the Earth-space environment.

EDUCATION:

BS in Physics with Math minor, Virginia Polytechnic Institute and State University, Blacksburg, Virginia. June 1988. PhD in Physics, Utah State University, Logan, Utah. (expected December 2020). Emphasis in space science and upper atmosphere plasma dynamics.

EXPERIENCE:

<u>Department of Defense (June 1991 – present)</u>

National Reconnaissance Office (NRO), Chantilly, VA

> DEPUTY DIRECTOR, Non-traditional GEOINT Program Office
> TECHNICAL DIRECTOR, Future Capabilities Group, Advanced Technology Office
> SPACE BRANCH CHIEF, GEOINT Future Capabilities Office (Joint Duty Assignment to the National Geospatial Agency)
> CHIEF ARCHITECT, NRO Advanced System Office

Space and Naval Warfare Systems Center, San Diego, CA

> CHIEF MISSION ENGINEERING, NRO Advanced System Office
> PROGRAM TECHNICAL DIRECTOR, Joint Milli-Arcsec Pathfinder Sensor

Office of Naval Research, Arlington, VA

> PROGRAM OFFICER, Ocean Atmosphere & Space Research

Naval Research Laboratory (NRL), 4555 Overlook Ave SW, Washington, DC

    PROGRAM SUPPORT, NRO/LSPO

    RESEARCH PHYSICIST, NRL X-ray Astronomy Branch

Computational Physics Inc, Springfield, VA (August 1988-June 1991)

    RESEARCH SUPPORT, NRL Upper Atmospheric Branch

AWARDS:

    AS&T Innovation Award, Feb 2016

    Navy Meritorious Civilian Service Award, February 2011

    LSPO Innovation & Achievement Award, August 2006

    NRL Alan Berman Research Publication Award, March 1994